UC Riverside

UC Riverside Electronic Theses and Dissertations

Title

Carbon Based Nano-Materials Research, Development and Applications in Optoelectronics

Permalink

https://escholarship.org/uc/item/09g4t1pc

Author

Wang, Feihu

Publication Date

2012

Peer reviewed|Thesis/dissertation

eScholarship.org Powered by the California Digital Library
University of California

UNIVERSITY OF CALIFORNIA
RIVERSIDE

Carbon Based Nano-Materials Research, Development and Applications in Optoelectronics

A Dissertation submitted in partial satisfaction
of the requirements for the degree of

Doctor of Philosophy

in

Physics

by

Feihu Wang

December 2012

Dissertation Committee:
Dr. Robert C. Haddon, Chairperson
Dr. Jing Shi
Dr. Chun Ning (Jeanie) Lau

Copyright by
Feihu Wang
2012

The Dissertation of Feihu Wang is approved:

_____

_____

_____
Committee Chairperson

University of California, Riverside

ACKNOWLEDGEMENTS

First and foremost I would like to thank my advisor and committee chairman, Prof. Robert C. Haddon for letting me join his research group and introducing me to materials science and nanotechnology. Professor Haddon is the most brilliant scientist I have ever worked with. His advice has been inspiring and motivating. His words of encouragement have always been a strong source of support especially in moments of difficulty. Working with Prof. Haddon has made me realize what a world-class scientist is like: he is energetic, confident and a great leader. He is an experimentalist on the surface but a great theoretician at heart. Without Prof. Haddon's help, I could not have completed my research work, and the following dissertation would not have come into existence.

I would like to thank Dr. Mikhail E. Itkis for his patient instruction and for providing me with the greatest help of all. As the only physics student working in a chemical engineering lab, I have realized that most of my research would have been very difficult, if not impossible, to complete without the direction and technical support from Dr. Itkis. During my graduate years, he has offered me great assistance not only in my research but also outside the academy, and has kindly treated me as a friend.

I would like to thank all members in my research group for their friendship and for sharing their experiences and research. Particularly, Dr. Elena Bekyarova

has offered me tremendous help in conducting chemistry experiment, revising my writing and discussing results. I have been impressed by her enthusiasm for scientific research and for learning new things. I will miss other members (including former members) of my research group, they are: Arindam Sarkar, Kimberly Worsley, Sandip Niyogi, Ramesh Palanisamy, Xiaobo Sun, Neetu Jha, Huazhou Wei, Irina Kalinina, Sushanta K. Pal, Pradip Bag, Aron Pekker, Santanu Sarkar, Xiaojuan Tian, Matthew Moser.

I would like to thank my committee members, Prof. Jing Shi, and Prof. Jeanie Lau. Professor Shi admitted me into the Department of Physics and Astronomy at UCR, and introduced the Haddon research group to me after I decided to study condense matter physics other than plasma physics.

I would like to thank my family for their continuing support and care through my entire life. In particular, I want to thank my beloved wife Chenshu for her companionship in the past years. I feel lucky to have met her at UCR, making this campus a sweet place to remember for all my life.

I would like to thank the publishers for allowing me to reprint materials in my dissertation. The text and figures of this dissertation, in part, is a reprint of the material as is appears in “Enhanced Electromodulation of Infrared Transmittance in Semitransparent Films of Large Diameter Semiconducting Single-Walled Carbon Nanotubes”. Nano Lett. 10, 937-942 (2010) by Wang, F., Itkis, M. E., Haddon, R. C.; “Effect of First Row Transition Metals on the Conductivity of

Semiconducting Single-Walled Carbon Nanotube Networks". Appl. Phys. Lett. 100,(2012) by Wang, F., Itkis, M. E., Bekyarova, E., Tian, X., Sarkar, S., Pekker, A., Kalinina, I., Moser, M.; Haddon, R. C.; "Solid-State Bis-Hexahapto-Metal Complexation of Single-Walled Carbon Nanotubes". J. Phys. Org. Chem. 25 (2012) by Wang, F., Itkis, M. E., Bekyarova, E., Sarkar, S., Tian, X., Haddon, R. C.; "Enhanced Photosensitivity of Electro-Oxidized Epitaxial Graphene". Appl. Phys. Lett. 98 (2011) by Itkis, M. E., Wang, F., Ramesh, P., Bekyarova, E., Niyogi, S., Chi, X., Berger, C., de Heer, W. A., Haddon, R. C..

ABSTRACT OF THE DISSERTATION

Carbon Based Nano-Materials Research, Development
and Applications in Optoelectronics

by

Feihu Wang

Doctor of Philosophy, Graduate Program in Physics
University of California, Riverside, December 2012
Dr. Robert C. Haddon, Chairperson

Carbon-based nano-materials, including single-walled carbon nanotubes (SWNTs), graphite nanoplatelets and graphene, possess remarkable electronic, optoelectronic properties, due to their unique dimensional and geometric structure. SWNT and Graphene have recently emerged as a potential basis for new generation of electronic and optoelectronic devices.

In Chapter 1, the fundamental knowledge of graphene, SWNT and SWNT thin film are introduced, including their structure and physical properties, as well as fabrication, properties and applications. In chapter 2 and chapter 3, two examples of optoelectronic applications in SWNT thin films are discussed:
1. solid state SWNT thin film field effect transistor (FET) electro-optical modulator in which the gate potential induced electro-optical modulation is significantly enhanced by utilizing optimized transparent bottom gate device, large diameter SWNTs, and by increasing the ratio of semiconducting to metal SWNTs.
2. Ionic liquid based SWNT thin film modulator in which a very strong electro-

optical modulation can be achieved in ionic liquid coated semiconducting SWNT thin film as a result of the position dependent shift of the SWNT Fermi level. The experimental results indicate that low conductivity semiconducting SWNT film is fascinating material and have wide range of optoelectronic applications. In chapter 4, effects of metal deposition on the conductivity of SWNT networks are discussed. It is found that controlled exposure of SWNT thin films to the e-beam evaporation of Cr leads to the formation of bis-hexahapto complexes at the SWNT sidewalls, thereby bridging adjacent carbon nanotubes and reducing the inter-nanotube junction resistance. In chapter 5, an example of optoelectronic applications in graphene is discussed. Controlled electro-oxidization modifies the electronic and optoelectronic properties of multilayer epitaxial graphene, and electro-chemical oxidized graphene has potential for UV detection applications.

TABLE OF CONTENTS

List of Acronyms ……xii
List of Figures ……...xiv
Chapter 1 Introduction to Carbon Nano-Materials 1
1.1 Graphene ……2
1.1.1 Structure of graphene ……2
1.1.2 Electronic properties of graphene ……4
1.2 Introduction to carbon nanotubes ……... 10
1.2.1 Structure of SWNT …… 10
1.2.2 Electronic properties of individual SWNT……12
1.3 Thin films of SWNTs ……...19
1.3.1 Bulk SWNT materials ……19
1.3.2 Optical properties of bulk SWNT materials ……20
1.3.3 Processing of SWNTs ……21
1.3.3.1 Dispersion of SWNTs ……..21
1.3.3.2 Purification of SWNTs ……23
1.3.3.3 Optical technique for purity evaluation of SWNTs ……..24
1.3.3.4 Separation of semiconducting and metallic SWNTs ……..27
1.3.4 Fabrication of SWNTs ……28
1.3.4.1 Direct growth ……29
1.3.4.2 Solution-based deposition ……..30
1.3.5 Application of SWNT thin films ……..33
References ……39

Chapter 2 Field Effect Induced Electro-Optical Modulation of Infrared Transmittance in SWNT Thin Films 4 7
2.1 Introduction ……..47
2.2 Experimental ……54
2.2.1 Fabrication of SWNT thin film electro-absorption modulator ….54

2.2.2 Spectroscopic setup for characterization of SWNT optoelectronics ……57
2.3 Results and discussion…….. 59
2.3.1 Observation of electro-optical modulation ..……..59
2.3.2 Diameter dependence of the field effect induced electro-optical modulation of infrared transmittance ……61
2.3.3 Effect of ratio of semiconducting and metallic SWNTs on the field effect induced electro-optical modulation of infrared transmittance ……64
2.3.4 Dependence of the field effect induced electro-optical modulation of infrared transmittance on the thickness of SWNT films ……68
2.3.5 Frequency dependence of the field effect induced electro-optical modulation of infrared transmittance ……71
2.4 Summary ……..72
References ……74

Chapter 3 Ionic Liquid Based Absorption Modulation in SWNT Film 7 7
3.1 Introduction ……77
3.2 Experimental ……..82
3.3 Results and discussion ……86
3.4 Phenomenological model ……93
3.5 Potential applications of the observed electro-optical effects …….98
3.6 Summary ……103
References ……...104

Chapter 4 Effect of Metal Deposition on the Conductivity of SWNT Networks 107
4.1 Introduction ……107
4.1.1 Electronic properties of SWNT thin films ……..107
4.1.2 Chemical doping of the SWNT thin films ……...110
4.1.3 Nanotube junctions ……..112
4.2 Experimental ……..117

4.3 Results and discussion ……121
4.3.1 Typical conductance change of channels during metal deposition ...……121
4.3.2 Conductance change of SC-SWNT films during metal deposition ...……123
4.3.3 Model ……127
4.3.4 Conductance change of P2-SWNT films during metal deposition ……131
4.3.5 Conductance change of M-SWNT films during metal deposition ……132
4.3.6 Orbital interaction diagram ……133
4.3.7 Three mechanisms of enhancement conductivity in SWNT films ……135
4.4 Summary ……137
References ……138

Chapter 5 Electro-Oxidized Epitaxial Graphene and its Optoelectronics Applications 142
5.1 Introduction ……142
5.1.1 Band gap engineering of graphene ……144
5.1.2 Optoelectronic applications of graphene ……146
5.2 Experimental ……149
5.3 Result and discussion ……153
5.3.1 Effect of electro-oxidation on surface of EG ……153
5.3.2 Effect of electro-oxidation on electrical properties of EG ……156
5.3.3 Effect of electro-oxidation on FET performance of EG ……158
5.3.4 Model of effect of electro-oxidation of EG ……162
5.3.5 Enhanced photosensitivity in electro-oxidized EG ……163
5.4 Summary ……170
References ……171

List of Acronyms

0D	0 Dimensional
1D	1 Dimensional
2D	2 Dimensional
3D	3 Dimensional
DOS	Density of States
CNT	Carbon Nanotube
SWNT	Single-Walled Carbon Nanotube
MWNT	Multi-Walled Carbon Nanotube
AP-SWNT	As Prepared-SWNT
EA	Arc Discharge
HiPco	High-Pressure Carbon Monoxide
CoMoCat	Cobalt-Molybdenum Catalyst
CVD	Chemical Vapor Deposition
M-SWNT	Metallic-SWNT
SC-SWNT	Semiconducting-SWNT
SEM	Scanning Electron Microscope
TEM	Transmission Electron Microscopy
AFM	Atomic Force Microscopy
TGA	Thermogravimetric Analysis
FET	Field Effect Transistor
EO-FET	Electro-Optical Field Effect Transistor
TFT	Thin Film Transistor

LCD	Liquid Crystal Display
OLED	Organic Light-Emitting Diode
EDL	Electric Double Layer
EDLT	Electric Double Layer Transistors
MEMS	Micro-Electro-Mechanical Systems
ALD	Atomic Layer Deposition
ITO	Indium Tin Oxide
QED	Quantum Electrodynamics
Abs	Absorbance
IR	Infrared
NIR	Near-Infrared
UV	Ultraviolet
Vis	Visible
IL	Ionic Liquid
SDS	Sodium Dodecyl Sulfate
DMF	N, N- Dimethylformamide
NP	Nitrophenyl
PDMS	Poly(dimethylsiloxane)
RP	Relative Purity
PEMFC	Proton Exchange Membrane Fuel Cell
CV	Cyclic Voltammetry
TCR	Temperature Coefficient of Resistance
MCT	Mercury Cadmium Telluride
PC	Polarization Catastrophe
EG	Epitaxial Graphene

List of Figures

Figure 1.1: Carbon nanotube materials: (a) graphene; (b) fullerene; (c) nanotube; (d) graphite. ……..2

Figure 1.2: Honeycomb lattice and its Brilliouin zone. (a) Lattice structure of graphene showing three nearest-neighbor A atoms (blue circles) relative to an B atom (yellow circle) and corresponding vectors $\vec{R}_1$, $\vec{R}_2$ and $\vec{R}_3$;(b) Graphene reciprocal lattice showing high symmetry points Γ, K, and M. The Dirac points are located at the K and K' points. ……3

Figure 1.3: (a) Graphene band structure. Adapted from Wilson, 2006. (b) The band structure in the vicinity of the K and K′ points showing the Dirac cones. Adapted from Wilson, 2006. ……..8

Figure 1.4: (a) Visual presentation of wrapping of graphene sheet into seamless SWNT cylinder along the chiral vector $\overrightarrow{C_h}$; (b) armchair, zigzag and general chiral SWNTs. ……...11

Figure 1. 5: Schematic of one-dimensional band structure (dispersion relation) of carbon nanotubes and corresponding density-of-states. (a) Band structure (left) and corresponding DOS of metallic nanotube. (b) Band structure (left) and corresponding DOS of semiconducting nanotube. ……..14

Figure 1.6: Figure 1.6: Kataura plot, note that γ_o is the nearest neighbor hopping integral, for which we have used the symbol β. ……16

Figure 1.7: Idealized electronic density of states of (a) 3D system. (b) 2D system. (c) 1D system and (d) 0D system. ……..18

Figure 1.8: Absorption spectra of (a) SWNT thin film (thickness ~ 70 nm), and (b) SWNT solution (concentration at a concentration of 0.5 mg/mL). (c) DOS of SWNTs. ……...21

Figure 1.9: End-wall and side-wall functionalization of SWNTs: dissolution and dichlorocarbene reactions of SWNTs. ……23

Figure 1.10: SEM images of AP-SWNT soot collected in the electric arc chamber. SEM purity grading system shows highest purity grade 6 to lowest grade 1. Note that images b-f (grades 5-1) were obtained from samples taken from the same synthetic experiment. ……25

Figure 1.11: Schematic illustration of the electronic spectrum of EA-SWNTs. …27

Figure 1.12: (a) Photograph of laser-ablation-grown SWNTs separated in a co-surfactant solution. The top band (orange) corresponds to predominantly semiconducting SWNTs and the band just below it (green) is highly enriched in metallic SWNTs (b) absorbance spectra of isolated semiconducting SWNTs and metallic SWNTs. ……28

Figure 1.13: SEM image of self-aligned SWNTs grown by CVD method, showing that the CNTs are well-aligned, closely contacted, and clean. ……..29

Figure 1.14: (a) Photograph of semi-transparent film of AP-SWNTs formed on a wire grid during the electric arc synthesis. (b) SEM image of the loose SWNT network. ……..30

Figure 1.15: SEM image of the dense SWNT network. ……..31

Figure 1.16: Vacuum filtration steps (a) Prepare diluted suspension of purified nanotubes. (b) Vacuum-filtratation of a dilute suspension of purified nanotubes on the filtration membrane. (c) Dissolution of the membrane to leave SWNT thin film floating in solvent (water). (d) Transfer of SWNT films to substrate to form SWNT thin film based device. ……..…..32

Figure 1.17: (a) Optical image of an interdigitated electrode from the sensor array, (b) Response curves of SWNT-PABS to 100 ppm NH_3. ……..34

Figure 1.18: Carbon nanotube application in fuel cells. ……..35

Figure 1.19: Fabrication of flexible transparent electrodes for OLED. ……..36

Figure 1.20: (a) High TCR SWNT network suspended between electrical contacts as bolometer. (b) SWNT optocoupler: SWNT thin film emitter and detector are mounted face-to-face on two sapphire rings so the radiation from SWNT emitter can be sensed by the detector. ……...38

Figure 2.1: Schematic representation of the density of states (DOS) of SWNTs contributing to the near-IR and far-IR absorption. (a) Intrinsic semiconducting SWNT; S_{11} and S_{22} correspond to the first and second interband transitions in the near-IR spectral range. (b) Hole-doped semiconducting SWNT; first interband transition (S_{11} doped) is shifted to higher energy due to depletion of the conduction band. ……...49

Figure 2.2: FIR-Vis-UV spectra of films of SWNT before and after exposure to bromine vapor. ……...49

Figure 2.3: (a) Spectra of a film of as-prepared SWNTs; (b) purified L-SWNTs before (dotted line) and after (solid line) heating under vacuum at 350 °C; (c) spectra of a film as a function of the duration of the exposure to the ambient atmosphere. ……51

Figure 2.4: (a) Schematic of SWNT thin file FET structure used in ref.18, 19; (b) IR absorption spectrum of SWNT-FET. (c) Difference spectra of absorbance, before and after gate bias (VG) application. Data sets are displayed for every 25V from VG =-100 to 100 V. ……..52

Figure 2.5: Vacuum filtration steps: (a) preparation of dilute suspension of purified nanotubes; (b) vacuum-filtration of a dilute suspension of purified nanotubes on the filtration membrane; (c) dissolved membrane leaves SWNT thin film floating in solvent (water); (d) SWNT films transferred to substrate, forming SWNT thin film based device. ……..55

Figure 2.6: Optical micrograph of the experimental setup for study of the electro-optical gating effect in SWNT thin films. The square-wave modulation is applied between ITO gate electrode and semitransparent SWNT thin film while infrared transmission is monitored. ……..57

Figure 2.7: (a) Multifunctional spectroscopic setup: Vis-IR-mid-IR Horiba Yobin-Robin ihr 320 monochromator coupled to a Bruker HYPERION 1000 infrared microscope. (b) Schematic of the station. ……58

Figure 2.8: (a) spectrum of absorbance (Abs) and (b) electro-modulated transmittance $\Delta T/T$ of 35 nm thick EA-SWNT film for gate voltages of +10V and -10V. (c) Schematic representation of the density of states (DOS) change of p-doped SWNT films controlled by gate voltage contributing to the near-IR and far-IR absorption. ……60

Figure 2.9: (a) Spectra of absorbance (Abs) and (b) electro-modulated transmittance $\Delta T/T$ of 35 nm thick films of four types of SWNTs for gate voltages of -10V: SG65 SWNTs; HiPCO SWNTs; laser ablation produced L-SWNTs; electric arc produced EA-SWNTs. (c) Amplitude of electro-optical modulation, $\Delta T/T$ at the peak of the S_{11} absorption band as a function of the SWNT bandgap and average diameter. ……62

Figure 2.10: (a) Spectra of absorbance (Abs) and (b) electro-modulated transmittance $\Delta T/T$ of 35 nm thick EA-SWNTs for gate voltages. (c) Spectra of absorbance (Abs) and (d) electro-modulated transmittance $\Delta T/T$ of 35 nm thick SG65 SWNTs for gate voltages. ……63

Figure 2.11: (a)Spectra of absorbance (Abs) and (b) electro-modulated transmittance $\Delta T/T$ of 35 nm thick films of SWNT samples with different ratios of concentrations of semiconducting to metallic SWNTs (S/M). (c) Peak amplitude of the electro-optical modulation $\Delta T/T$ in SWNT films as a function of the semiconducting SWNT content. ……66

Figure 2.12: Amplitude of the electro-modulated transmittance $\Delta T/T$ as a function of semiconducting SWNT film thickness. ……..69

Figure 2.13: Amplitude of the electro-modulated absorption coefficient Δα as a function of semiconducting SWNT film thickness. 70

Figure 2.14: Frequency dependence of the electro-modulated transmittance Δ*T*/*T* normalized to the 1 kHz value. ……...71

Figure 2.15: (a) Absorption spectra of 6.5nm thick semiconducting SWNT films of under DC gate voltage. (b) Spectra of the electro-modulated transmittance Δ*T*/*T* of semiconducting SWNT film at several amplitudes of bipolar gate voltage modulation indicated next to the spectral curve. ……..73

Figure 3.1: (a) Schematic of the IL-gated SWNT thin film FET. (b) Spectral transmittance of the nanotube film FET as a function of applied counter-electrode "gate" voltage. ……79

Figure 3.2: (a) Schematic of molecular structures of the IL DEME-TFSI (top) and the cross-section of IL/ZnO EDLT (bottom). Blue, pink, green, and red spheres represent the $DEME^+$ cation, $TFSI^-$ anion, hole, and electron. (b) Comparison of the dynamical response to stepwise pulses of VG=2 V in EDLTs gated by IL, liquid $KClO_4$/PEO and solid $KClO_4$/PEO electrolytes. ……81

Figure 3.3: Schematic of a two-terminal semiconducting SWNT (SC-SWNT) channel in contact with an ionic liquid. ……..81

Figure 3.4: Schematic of the devices used in the experiment. (a) Schematic of the setup for electro-optical measurements with narrow infrared beam scanning the length of the SWNT channel. (b) Schematic of the SC-SWNT film on a pre-patterned substrate with 20 in-line electrodes coated with IL. ……..84

Figure 3.5: Schematic of device preparation. ……..85

Figure 3.6: (a) Linear I-V characteristic of intrinsic SWNT thin film and Non-linear I-V characteristic of SWNT thin film channel after coating with ionic liquid. (b) Electro-optical modulation of infrared transmittance T/T at wavelength 1.8 μm as a function of the amplitude and polarity of applied voltage. ……..87

Figure 3.7: Schematic of the setup for electro-optical measurement with the narrow infrared beam scanning the length of the SWNT channel. (a-c) Modification of the absorption spectra of the SWNT film at negative and positive electrodes (positions A and C, respectively, and the center of the channel (position B). ……88

Figure 3.8: (a) (b) Spatial dependence of the electro-optical modulation of infrared transmittance T/T on the amplitude and polarity of the applied voltage. (c) Voltage dependence of T/T at different positions along the SWNT channel..90

Figure 3.9: (a) Configuration of the SC-SWNT film on a pre-patterned substrate with 20 in-line electrodes. (b) Linear spatial distribution of the electrical potential along the SWNT channel before coating with ionic liquid. (c) Configuration of the SC-SWNT film on a pre-patterned substrate with 20 in-line electrodes coated with IL. (d) (e) Non-linear spatial distribution of the electrical potential along the SWNT channel after coating with ionic liquid as a function of the amplitude and polarity of the applied voltage. ……..……..92

Figure 3.10: The temporal evolution of the electrical potential distribution along the channel. ……93

Figure 3.11: Model of the observed non-linear electrical and electro-optical effects in SWNT thin films in ionic liquid. (a) (b) Spatial distribution of the SWNT valence and conductance bands, Fermi level and electronic density of states (DOS) in the SWNT channel without ionic liquid. (a) V = 0 V, and (b) V = 2 V. (c) (d) Spatial distribution of cations and anions in the ionic liquid, SWNT valence and conductance bands, Fermi level, DOS in SWNT channel coated by ionic liquid. (c) V = 0 V, and (d) V = 2V. S11 band under applied voltage in the vicinity of electrodes, (b) with IL (d) without IL. ……94

Figure 3.12: Electro-optical modulation of S11 absorption accompanied by modulation of mid-infrared and far-infrared absorption originating from S_{fc} excitations. ……98

Figure 3.13: **(**a) Electronic density of states (DOS) of semiconducting SWNTs of larger diameter/smaller bandgap (left); smaller diameter/larger bandgap (center); and in the case of the shift of chemical potential inside the valence band leading to the suppression of interband transitions S11 and S22 and appearance of low energy free carrier absorption S_{fc}(right). (b) Schematic of electro-optical field effect transistor (EO-FET) with semiconducting SWNTs as electro-active channel and metallic SWNTs as gate electrode separated by a layer of ionic liquid. (c) Spectra of absorption (Abs) and electro-optical modulation of transmission T/T utilizing EO-FETs with semiconducting SWNTs of four different diameters from 0.8 to 1.55nm with the spectra of electro-optical modulation extending from visible to near-infrared range (500 to 2500nm). ……..99

Figure 3.14: Electro-optical configuration and functionalities based on the SWNT thin film channel in an ionic liquid. (a) Schematic of setup in which large area of SWNT film can be switched from an opaque to the transparent state by application of voltage across two closely separated electrodes, and (c) its experimental demonstration. (b) Schematic of a set of interdigitated electrodes inserted in the SWNT channel to be used to generate periodic spatial electromodulation of infrared transmittance with the amplitude and phase controlled by the amplitude and polarity of the applied voltage, and (d) experimental demonstration. ……102

Figure 4.1 Conductivity of AP-SWNT, P2-SWNT, and P3-SWNT films as a function of film thickness. ……109

Figure 4.2 (a) IR-Vis-UV spectra of films of SWNT before and after exposure to bromine vapor.32 (b) DOS of intrinsic semiconducting SWNTs and chemically doped semiconducting SWNTs: chemical doping leads to the suppression of interband transitions S_{11} and S_{22} and appearance of low energy free carrier absorption S_{fc}(right). ……..112

Figure 4.3: (a) Tapping mode AFM image of a crossed SWNT device. Two SWNTs (green) can be seen spanning the Cr/Au electrodes (yellow). (b and c) The structures of a junction between two metallic (5,5) SWNTs. (d) *I-V* characteristics of several SWNT junctions. (e) The band structure of M-M junction. (f) The band structure of S-S junction, (g) The band structure of M-S junction. ……115

Figure 4.4: (a) Schematic of the SWNT thin film on the interdigitated electrodes together with a SEM image of the representative film. (b) Schematic of the SWNT thin film on the alumina membrane connected to the electrodes together with a SEM image of a representative film. ……118

Figure 4.5: Schematic of conductance as a function of duration of metal deposition or thickness of metal deposited on to channel. (a) Deposition of gold atoms to SWNT film or blank channel. (b) Deposition of chromium (Cr) atoms to SWNT films. ……..121

Figure 4.6: Conductivity of SC-SWNT films (t = 8nm), as a function of the duration of metal deposition of Li, Cr, and Au. ……..……123

Figure 4.7: (a) Conductivity of SWNT films as a function of the duration of metal deposition of Ti, V, Cr, Mn, and Fe. (b) Effect of metal atom deposition on the conductivity of SWNT films. ……...126

Figure 4.8: Electron transfer processes (doping): Li atoms (green) donate electrons to the conduction bands of the SWNTs. ……128

Figure 4.9: (a) Schematic of (η^6-benzene)$_2$Cr where the separation between benzene rings in (η^6-benzene)$_2$Cr is known to be 3.226 Å. (b) SWNT-SWNT junction with van der Waals gap of 3.15 Å. ……129

Figure 4.10: Cr atoms form bis-hexahapto complexes at the SWNT sidewalls thereby bridging adjacent carbon nanotubes and reducing the inter-nanotube junction resistance. ……130

Figure 4.11: Conductivity of P2-SWNT films as a function of the duration of metal deposition. ……131

Figure 4.12: Conductivity of M-SWNT films as a function of the duration of metal deposition. ……133

Figure 4.13: Orbital interaction diagram for (η^6-$C_6H_6)_2$Cr. Adapted from Ref. 59. ……134

Figure 4.14: Schematic of conductance as a function of duration of metal deposition or thickness of metal deposited on to SWNT thin film. ……..135

Figure 5.1: (a) Structure of the nitrophenyl (NP) addition products of graphene. (b) Angle-resolved photoelectron emission spectroscopy of NP-functionalized epitaxial graphene showing two diffuse bands highlighted by the dashed lines, corresponding to Dirac cones with a band edge 0.36 eV below the Fermi level, estimated from constant energy cuts.42 (c) The magnetism of EG due to NP functionalization. ……146

Figure 5.2: (a) Schematic of SiC substrate with two isolated EG channels, oxidation is conducted on one channel, leaving another channel in its pristine state. (b) Schematic illustration of electrochemical oxidation of epitaxial graphene, and cyclic voltammogram of epitaxial graphene electrode in 1 M HNO_3 (inset). ……..149

Figure 5.3: Schematic of the EG based FET. ……151

Figure 5.4: AFM images of C face of EG sample at different stages of the electro-oxidation. (a) Pristine EG. (b-e) Transformation of EG surface during the oxidation steps. ……154

Figure 5.5: (a) Raman spectra of EG-D pristine sample, after 10 min and 20 min electro-oxidation; (b) intensity of 2D-band (red) and D-band to G-band intensities ratio (blue) as a function of electro-oxidation time. ……155

Figure 5.6: Temperature dependences of resistance of graphene channels before and after oxidation. The resistance data were taken before FET fabrication without gating the channels. (a) Test channel. (b) Reference channel. ……156

Figure 5.7: Temperature dependences of resistances of pristine and electro-oxidized graphene channels presented as (a) Arrhenius and (b) semi-logarithmic plot. ……158

Figure 5.8: (a) Dependence of the channel current on gate voltage for pristine EG channel as a function of temperature. (b) Dependence of the channel current on gate voltage for electro-oxidized EG channel as a function of temperature. (c) FET mobility as a function of temperature for pristine and electro-oxidized EG channels. ……..161

Figure 5.9: Schematic of effect of electro-oxidation on electronics properties of EG. ……163

Figure 5.10: (a) Effect of fluorescent room light illumination on the resistance of electro-oxidized (blue circles) and pristine (black open circles) EG channels. (b) Spectral dependence of photoresponse of electro-oxidized channel. Inset shows schematics of the electro-oxidation EG substrate. ……164

Figure 5.11: (a) Modulation of the resistance of the electro-oxidized EG channel under square-wave pulses of blue LED illumination of different power. (b) Dependence of electro-oxidized EG channel photocurrent on the power of incident radiation. Inset shows the dependence in logarithmic scales. ……..166

Figure 5.12: (a) Modification of transfer characteristics of electro-oxidized EG channel FET under blue LED illumination at incident power of 20 μW. (Inset) Microscope image of SiC substrate with two FETs based on pristine and electro-oxidized EG channels with SWNT thin film gate electrode. Dog bone shape of the channels is indicated by dashed line. (b-d) Photoresponse of electro-oxidized EG channel at gate voltages (b) -100V, (c) 0 V and (d) +100V at incident irradiation power 0.2 μW. ……..169

Chapter 1 Introduction to Carbon Nano-Materials

In 2007, I started to pursue my Ph.D degree in materials and nano-scale physics. My research is focused on the development of carbon based nano-materials and their optoelectronic applications. The carbon-based materials I have studied include graphene, carbon nanotubes, and organic semiconductors. The building block of these materials is carbon, a chemically versatile element, readily binding with other elements and it is essential to living systems and provides the basis of organic compounds. Carbon atoms can also link with each other in various structures to form diverse carbon-based materials. It has long been found that there are many allotropes of carbon, of which the best known are graphite, diamond, and amorphous carbon. In past few decades, new types of carbon nano-materials with different dimensionalities were discovered: 0D nanometer-sized balls (fullerenes),[1] 1D carbon nanotubes [2] and 2D graphene. [3, 4] Physical properties of carbon vary widely with the allotropic form. These carbon based nano-materials show remarkable physical properties that have entranced both scientists in academia investigating the basic behavior of matter, and engineers in industry developing next generation of electronic materials and nanotechnology. In this chapter the general knowledge of graphene and single-walled carbon nanotubes (SWNTs) will be introduced, including their structure and physical properties, as well as fabrication, properties and application of SWNT thin films.

1.1 Graphene

1.1.1 Structure of graphene

Although the theoretical study of the electronic properties of the single layer graphite has been conducted for a long time, physicists first isolated individual graphene sheets by using adhesive tape in 2004.[3] Graphene is moderately stable in air, transparent and flexible.[5, 6] It is the thinnest and strongest material ever isolated. Single layer graphene is one layer of sp^2-bonded carbon atoms which are densely packed in a honeycomb crystal lattice, as shown in Figure 1.1. It can be described as a system of connected benzene rings stripped of their hydrogen atoms. 2D graphene can be seen as a building block material for other sp^2 bonded carbon materials. It can be rolled up into 1D nanotube, or stacked into 3D graphite (Figure 1.1).

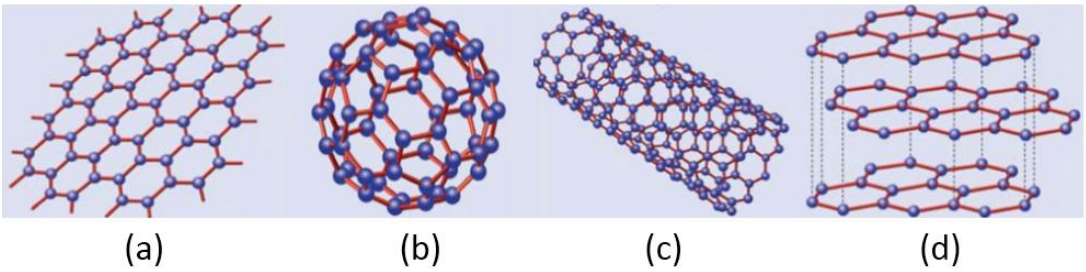

Figure 1.1: Carbon nanotube materials: (a) graphene; (b) fullerene; (c) nanotube; (d) graphite.

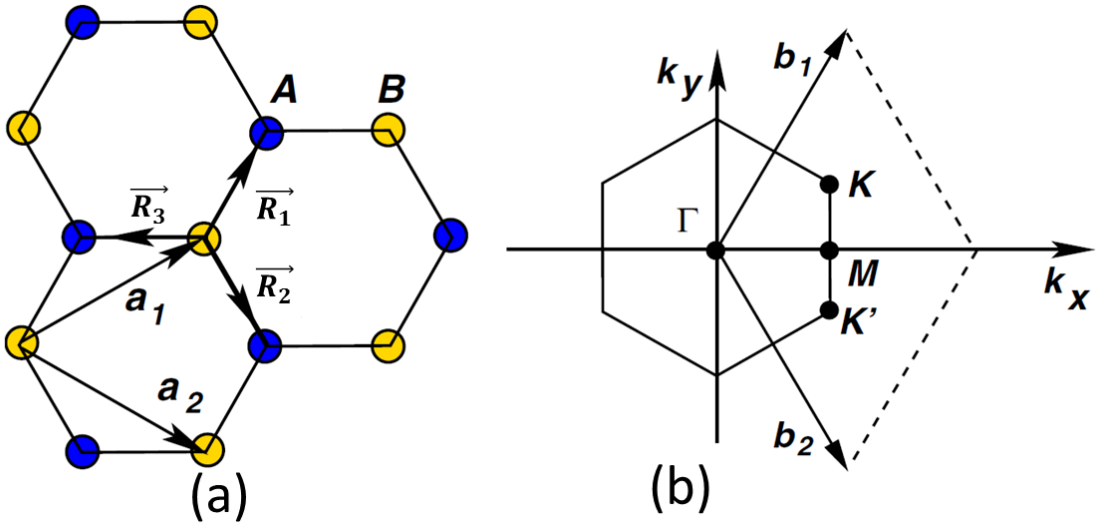

Figure 1.2: Honeycomb lattice and its Brilliouin zone. (a) Lattice structure of graphene showing three nearest-neighbor A atoms (blue circles) relative to an B atom (yellow circle) and corresponding vectors $\vec{R}_1$, $\vec{R}_2$ and $\vec{R}_3$;(b) Graphene reciprocal lattice showing high symmetry points Γ, K, and M. The Dirac points are located at the K and K' points.

The structure of graphene can be seen as a triangular lattice with a basis of two atoms in each cell. The equivalent atom sublattices A and B are indicated by yellow and blue colors in Figure 1. 2. The lattice vectors can be written as: [5]

$$\vec{a}_1 = \frac{a}{2}(3, \sqrt{3})$$

$$\vec{a}_2 = \frac{a}{2}(3, -\sqrt{3})$$

where a =1.42 Å is the length of carbon-carbon bond.

The Brillouin zone of graphene is shown in Figure 2.2 (b). The reciprocal-lattice vectors are given by:

$$\vec{b}_1 = \frac{2\pi}{3a}(1, \sqrt{3})$$

$$\vec{b}_2 = \frac{2\pi}{3a}(1, -\sqrt{3})$$

The six corners of the Brillouin zone are called the Dirac points. Due to high symmetry, only two of them, labeled as K and K′ (Figure 2.2 (b)), are unique, the remaining four are related by symmetry. The Dirac points are of great importance in the electronic structure, transport properties and chemistry of graphene.

1.1.2 Electronic properties of graphene

The electronic properties can be simply analyzed by utilizing the tight-binding approach. [7-9]

The tight binding theorem implies that

$$\Phi(\vec{x}) = c_1\Phi_1(\vec{x}) + c_2\Phi_2(\vec{x})\psi \qquad (1.1)$$

where $\Phi(\vec{x})$ is the wave function due to the unit cell, and $\Phi_1(\vec{x})$ and $\Phi_2(\vec{x})$ are the wave functions related to atoms A and B in Figure 1.2, respectively, and c_1 and c_2 are two constants. We will be using Bloch's theorem:

$$\psi(\vec{x}) = \sum_{\vec{R}} e^{i\vec{k}\cdot\vec{R}}\Phi(\vec{x} - \vec{R}) \qquad (1.2)$$

where $\psi(\vec{x})$ is the total wave function of lattice, $\vec{k}$ is the wave vector, and $\vec{R}$ are three nearest-neighbor vectors

At the simplest level of tight-binding theory, there will be a hopping integral between each A carbon atom, and its three nearest neighbor B carbon atoms (see Figure 1.2 (a)):

$$\vec{\mathrm{R}}_1 = \frac{\mathrm{a}}{2}\left(1, \sqrt{3}\right)$$

$$\vec{\mathrm{R}}_2 = \frac{\mathrm{a}}{2}\left(1, -\sqrt{3}\right)$$

$$\vec{\mathrm{R}}_3 = -\mathrm{a}(1, 0)$$

Consider the Hamiltonian for single electron in the atomic potential given by all carbon atoms:

$$H = \frac{\vec{p}^2}{2m} + \sum_{\vec{R}}\left(V\left(\vec{x} - \vec{x}_1 - \vec{R}\right) + V\left(\vec{x} - \vec{x}_2 - \vec{R}\right)\right) \tag{1.3}$$

Where $\vec{x}_{1,2}$denote the position of the two carbon atoms in the unit cell.

For simplicity, we are free to set:

$$H = U(\vec{x}) = \sum_{\vec{R}}\left(V\left(\vec{x} - \vec{x}_1 - \vec{R}\right) + V\left(\vec{x} - \vec{x}_2 - \vec{R}\right)\right) \tag{1.4}$$

Now we need to solve the Schrodinger equation:

$$H\psi(\vec{x}) = \varepsilon\psi(\vec{x}) \tag{1.5}$$

Simply project $\psi(\vec{x})$ on state $\Phi_1(\vec{x})$ and $\Phi_2(\vec{x})$, and we have:

$$\langle\Phi_1(\vec{x})|H|\psi(\vec{x})\rangle = \varepsilon\langle\Phi_1(\vec{x})|\psi(\vec{x})\rangle \tag{1.6}$$

$$\langle\Phi_2(\vec{x})|H|\psi(\vec{x})\rangle = \varepsilon\langle\Phi_2(\vec{x})|\psi(\vec{x})\rangle \tag{1.7}$$

Now we calculate $\langle\Phi_1(\vec{x})|\psi(\vec{x})\rangle$ and $\langle\Phi_1(\vec{x})|H|\psi(\vec{x})\rangle$:

$$\langle \Phi_1(\vec{x})|\psi(\vec{x})\rangle = c_1 + c_2 \int {\Phi_1}^* \Phi_2 \left(e^{i\vec{k}\cdot\vec{R}_1} + e^{i\vec{k}\cdot\vec{R}_2} + e^{i\vec{k}\cdot\vec{R}_3}\right)$$

$$= c_1 + c_2 \int e^{-i\frac{3a}{2}k_x} {\Phi_1}^* \Phi_2 \left(1 + e^{-i\vec{k}\cdot\vec{a}_1} + e^{-i\vec{k}\cdot\vec{a}_2}\right)$$

$$= c_1 + c_2 S \left(1 + e^{-i\vec{k}\cdot\vec{a}_1} + e^{-i\vec{k}\cdot\vec{a}_2}\right)$$

$$= c_1 + c_2 S\, \alpha\left(\vec{k}\right) \tag{1.8}$$

where $S = \langle \Phi_1(\vec{x})|\Phi_2(\vec{x})\rangle$, (1.9)

and $\alpha\left(\vec{k}\right) = 1 + e^{-i\vec{k}\cdot\vec{a}_1} + e^{-i\vec{k}\cdot\vec{a}_2}$, (1.10)

$$\langle \Phi_1(\vec{x})|H|\psi(\vec{x})\rangle = c_2\langle \Phi_1(\vec{x})|U|\Phi_2(\vec{x})\rangle \left(1 + e^{-i\vec{k}\cdot\vec{a}_1} + e^{-i\vec{k}\cdot\vec{a}_2}\right) = c_2\beta\, \alpha\left(\vec{k}\right) \tag{1.11}$$

Where $\beta = \langle \Phi_1(\vec{x})|U|\Phi_2(\vec{x})\rangle$ (1.12)

Putting equations (1.8) and (1.11) into (1.6):

$$c_2\beta\, \alpha = \varepsilon(c_1 + c_2 S\, \alpha) \tag{1.13}$$

From equation (1.7), we can have:

$$c_1\beta\, \alpha^* = \varepsilon(c_2 + c_1 S\, \alpha^*) \tag{1.14}$$

Thus, the eigenvalue equations derived from this tight-binding approximation are:

$$\begin{pmatrix} \varepsilon & \alpha(S\varepsilon - \beta) \\ \alpha^*(S\varepsilon - \beta) & \varepsilon \end{pmatrix} \begin{pmatrix} c_1 \\ c_2 \end{pmatrix} = \begin{pmatrix} 0 \\ 0 \end{pmatrix} \tag{1.15}$$

The dispersion relation is expressed as:

$$\varepsilon = t\sqrt{3 + \cos\left(\vec{k}\cdot\vec{a}_1\right) + \cos\left(\vec{k}\cdot\vec{a}_2\right) + \cos(\vec{k}\cdot(\vec{a}_2 - \vec{a}_1))} \tag{1.16}$$

or

$$\varepsilon = \mathrm{t}\sqrt{1 + 4\cos^2\frac{\sqrt{3}\mathrm{k_y a}}{2} + 4\cos\frac{\sqrt{3}\mathrm{k_y a}}{2}\cos\frac{3\mathrm{k_x a}}{2}} \tag{1.17}$$

Figure 1.3 (a) is the 3D plot of the energy dispersion relation of graphene. It is obvious that in graphene the conduction and valence bands touch each other at the Dirac points resulting in zero band gap. It is straightforward to check that the energy at all corners of BZ is zero. Thus intrinsic single-layer graphene is a semimetal or a zero-band-gap semiconductor.

Furthermore, we can apply Taylor's expansion in the vicinity of the Dirac points:

$$\vec{\mathrm{k}} = \vec{K} + \vec{\mathrm{q}} \tag{1.18}$$

where $\vec{K}$ is the position of Dirac points, and $\vec{\mathrm{q}}$ is small, $\mathrm{q_x a}, \mathrm{q_y a} \ll 1$.

For example, if we choose $\vec{K} = \frac{2\pi}{3\mathrm{a}}\left(1, \frac{\sqrt{3}}{3}\right)$, the energy dispersion relation can be linearized and simplified as:

$$\mathrm{E} = \frac{3\mathrm{t}}{2}\sqrt{\mathrm{q_x}^2 + \mathrm{q_y}^2} \tag{1.19}$$

as plotted in Figure 1.3 (b).

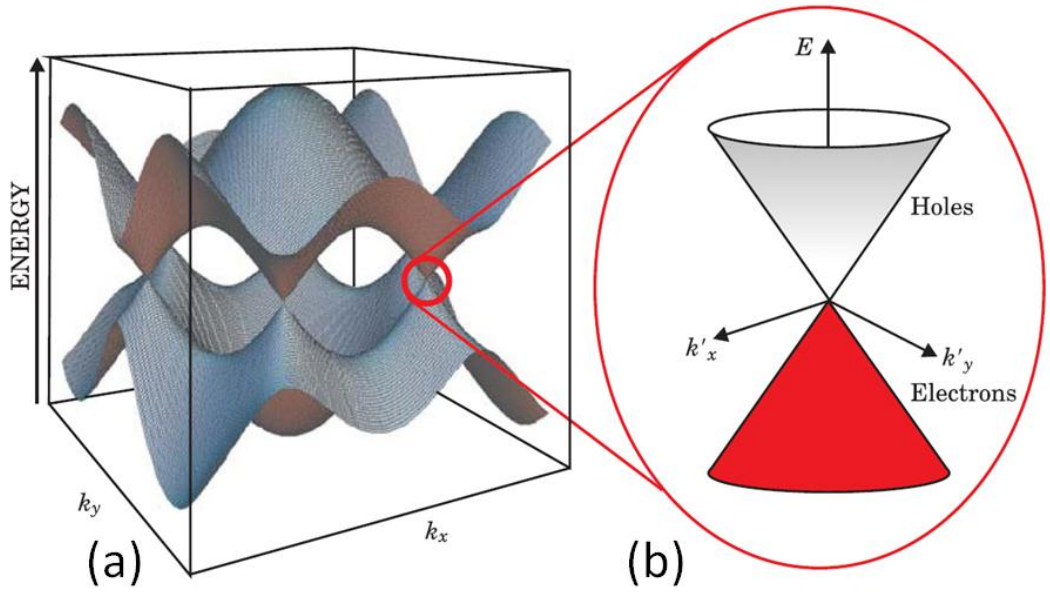

Figure 1.3: (a) Graphene band structure. Adapted from Wilson, 2006. (b) The band structure in the vicinity of the K and K′ points showing the Dirac cones. Adapted from Wilson, 2006.

Charge carriers in graphene move, unimpeded, at speeds 10–100 times faster than in today's silicon chips at normal temperatures.[10] Thus graphene is considered as a candidate for next generation devices, even though pristine graphene is not a semiconductor with a finite band gap. In addition to its remarkable electronics application promise, graphene offers a unique experimental stage for fundamental research in chemistry, [11-23] condensed matter physics and even partial physics. For example, the waves function of the electric charge behave like photons of light – that is, as if they are massless – yet retain the quantum character of electrons, carrying quantized charge and spin. Moreover, it is found that these unique electronic species are subject to the special theory of relativity– quantum electrodynamics, or QED. [24-26] Therefore,

graphene offers the prospect of testing some aspects of QED, which usually require high-energy particle accelerators, in cheaper table-top experiments.

1.2 Introduction to carbon nanotubes

1.2.1 Structure of SWNT

Carbon nanotubes are categorized as multi-walled nanotubes (MWNTs) and single-walled nanotubes (SWNTs). The MWNTs, consisting of several concentric cylindrical shells, were discovered by Iijima in conventional graphitic materials.[2] Shortly after the discovery of MWNTs, SWNTs composed of single shell, were synthesized by using the arc-discharge method with transition-metal catalysts.[27, 28]

In this thesis, I will only discuss SWNTs. The structure of SWNT can be visualized as wrapping a graphene along a chiral vector $\overrightarrow{C_h} = n\overrightarrow{a_1} + m\overrightarrow{a_2}$, into a seamless cylinder, as shown in Figure 1.4 (a). The carbon nanotube diameter and chiral angle are uniquely related to a pair of indices (n, m), by which the type of SWNT is represented. The diameter of an ideal nanotube can be calculated from its (n, m) indices as follow:

$$d = \frac{a}{\pi}\sqrt{n^2 + nm + m^2}, \qquad (1.20)$$

where a = 0.246 nm.

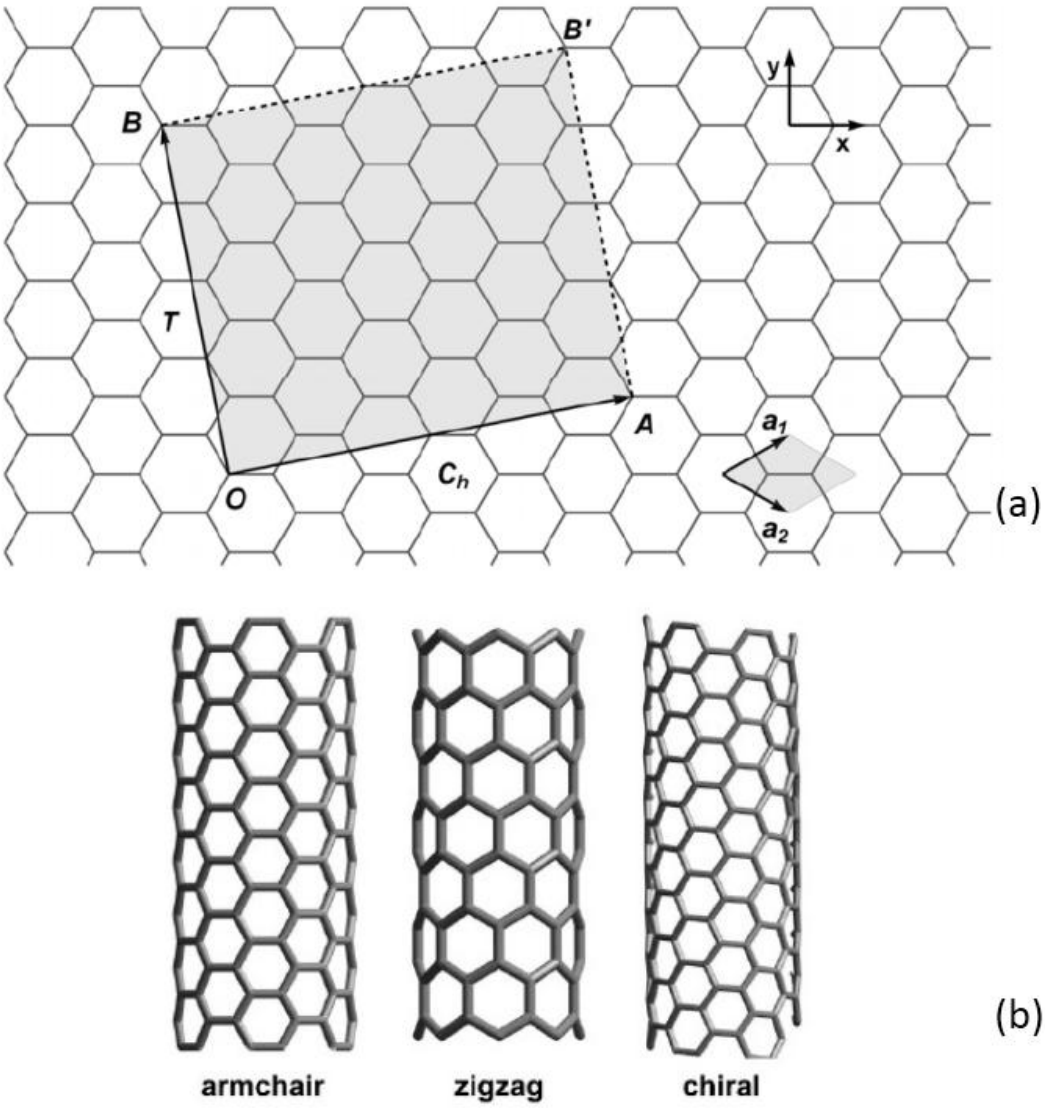

Figure 1.4: (a) Visual presentation of wrapping of graphene sheet into seamless SWNT cylinder along the chiral vector $\overrightarrow{C_h}$; (b) armchair, zigzag and general chiral SWNTs.

In the case of m=n, the carbon nanotube is called an armchair nanotube, while in the case of m=0 or n=0 the carbon nanotube is called a zigzag nanotube; all other types are called chiral nanotubes (Figure 1.4 (b)).

1.2.2 Electronic properties of individual SWNTs

Because of its one dimension structure and strong C-C covalent bonds, CNTs possesses unparalleled mechanical, thermal and electrical properties compared with other materials.

The electronic properties of single-walled carbon nanotubes can be deduced from that of graphene by mapping the band structure of 2D hexagonal lattice onto a cylinder. From the dispersion relation of graphene, we see that the Fermi energy is located at the K-points, and the low energy properties can be described by expanding the wave functions around $\vec{K}$. If we look at the eigenvalue problem again, we can apply expansion in the vicinity of the Dirac points:

$\vec{\mathrm{k}} = \vec{K} + \vec{\mathrm{q}}$, where $\vec{K}$ is the position of Dirac points, and $\vec{\mathrm{q}}$ is small, $\mathrm{q_x a}, \mathrm{q_y a} \ll 1$.

$$\varepsilon\left(\vec{\mathrm{k}}\right) = E\left(\vec{K}\right) + \varepsilon(\vec{\mathrm{q}}) = \varepsilon(\vec{\mathrm{q}}) \tag{1.21}$$

and express the function as a linear expansion at $\vec{K}$. Then the eigenvalue problem from equation (1.3) can be obtained:

$$\begin{pmatrix} \varepsilon(\vec{q}) & \frac{3\beta a(q_x + iq_y)}{2} \\ \frac{3\beta a(q_x - iq_y)}{2} & \varepsilon(\vec{q}) \end{pmatrix} \begin{pmatrix} c_1 \\ c_2 \end{pmatrix} = \begin{pmatrix} 0 \\ 0 \end{pmatrix} \tag{1.22}$$

The dispersion relation becomes:

$$\varepsilon(\vec{\mathrm{q}}) = \frac{3\beta a}{2}|\vec{\mathrm{q}}| \tag{1.23}$$

Furthermore the velocity of a wave packet is given by

$$\vec{v} = \hbar \frac{\partial \varepsilon(\vec{\mathrm{q}})}{\partial \vec{\mathrm{q}}} \tag{1.24}$$

It is independent of direction and in magnitude it is given by

$$v_F = \frac{3\beta a}{2\hbar} \tag{1.25}$$

By using the velocity we can express the dispersion relation as:

$$\epsilon(\vec{\mathrm{q}}) = \hbar v_F |\vec{\mathrm{q}}| \tag{1.26}$$

For (n,m) tube, we can decompose the wave vector $\vec{\mathrm{q}}$ into a component along the tube axis($q_{\parallel}$) and one perpendicular to it ($q_{\perp}$), in a form:

$$\vec{\mathrm{q}} = \mathrm{k}_{\parallel}\vec{\mathrm{e}_{\parallel}} + k_{\perp}\vec{e_{\perp}} \tag{1.27}$$

where $\vec{e_{\perp}} = \vec{\mathrm{C}_{\mathrm{h}}}/\left|\vec{\mathrm{C}_{\mathrm{h}}}\right|$

Because of the periodic boundary conditions around the tube circumference the transverse wave vector $k_{\perp}$will be quantized as:

$$k_{\perp,p} = 2\frac{\frac{m-n}{3}+N}{d} \tag{1.28}$$

where $\pi d = \left|\vec{\mathrm{C}_{\mathrm{h}}}\right|$, N is integer, and d is the tube diameter.

$$\varepsilon(\vec{\mathrm{q}}) = \hbar v_F |\vec{\mathrm{q}}| \tag{1.29}$$

The final result for the band structure of SWNTs can be presented as:

$$\varepsilon(\vec{\mathrm{k}}) = \varepsilon(\mathrm{k}_{\parallel}) = \frac{2\hbar v_F}{d}\sqrt{\left(\frac{\mathrm{k}_{\parallel} d}{2}\right)^2 + \left(\frac{m-n}{3} + N\right)^2} \tag{1.30}$$

It is easy to see that if $\frac{m-n}{3} \in Z$, nanotube will have zero band gap, displaying metallic or semi-metallic behavior(Figure 1.5(a)); whereas other types of tubes have finite band gaps resulting in semiconducting behavior (Figure 1.5(b)). The resulted band gap is inversely proportional to the diameter and equal to $E_g = \frac{2E_0}{3}$, where $E_0 = \frac{2\hbar v_F}{d}$.

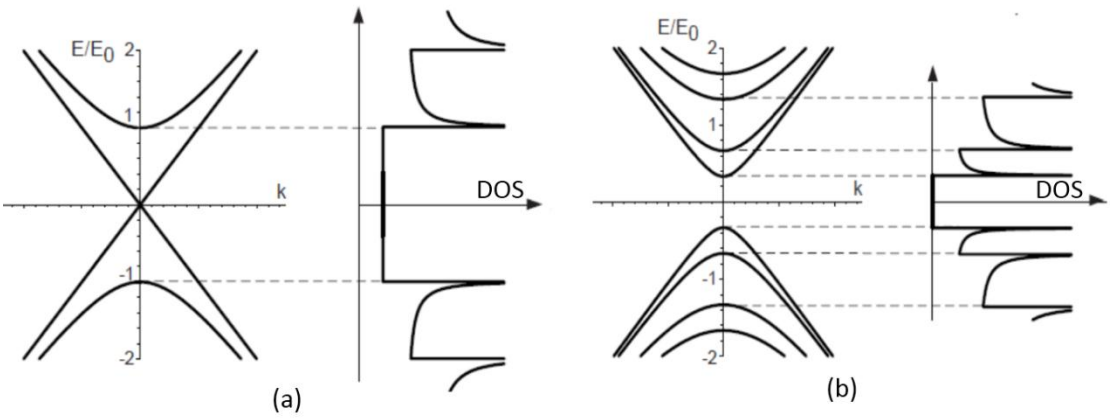

Figure 1. 5: Schematic of one-dimensional band structure (dispersion relation) of carbon nanotubes and corresponding density-of-states. (a) Band structure (left) and corresponding DOS of metallic nanotube. (b) Band structure (left) and corresponding DOS of semiconducting nanotube.

Briefly, results of electronic structure calculations can be summarized as following. The electronic properties of single-walled carbon nanotubes are determined by the chiral vector.[8, 9, 29, 30]Depending on the folding angle and the diameter, nanotubes can be metallic or semiconducting. Except for very small diameter nanotubes, tubes with structures for which n - m is divisible by 3 display metallic or semimetallic behavior leading, for example to the metallic nature of all

armchair (n = m) nanotubes. Other tubes have a band gap and show semiconducting behavior with the band gap of semiconducting SWNTs decreasing with increasing diameter as 1/d. More general theories are developed by White and Mintmire et al. [31-33]

The theory is supported by scanning tunneling spectroscopy experiments.[34] The relation between the energy gaps of SWNTs was presented in the form of the Kataura plot shown in Figure 1.6.[35, 36] Typical semiconducting SWNTs range from 2.6 to 0.7nm in diameter with corresponding band gaps varying from 0.5 to 2 eV.

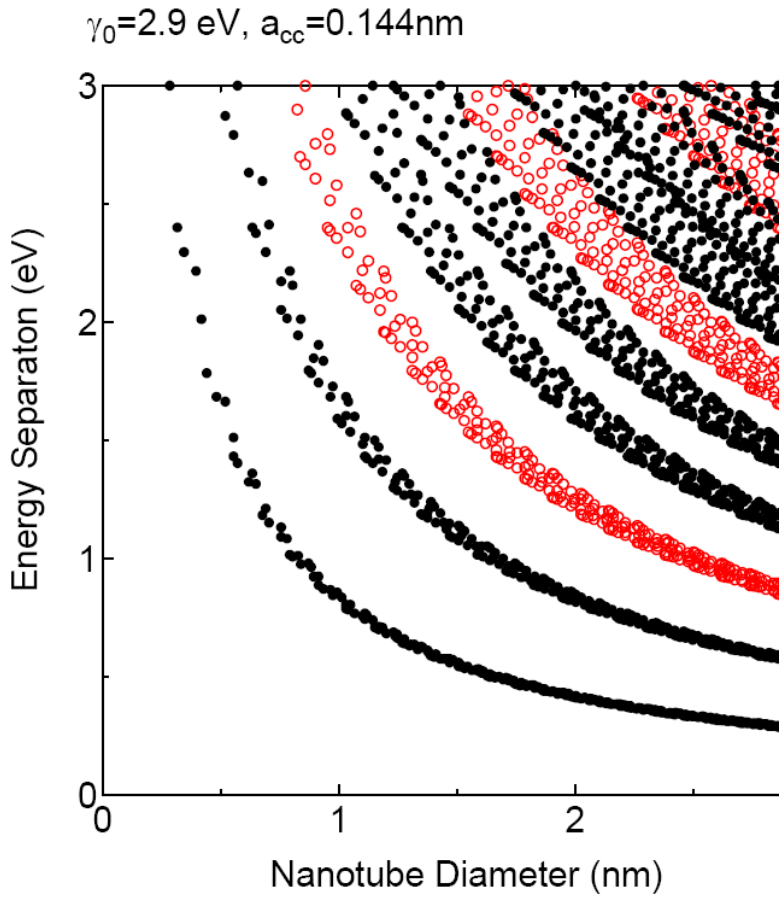

Black points are semiconductor nanotubes
Red points are metallic nanotubes

Figure 1.6: Kataura plot,[36] note that γ_o is the nearest neighbor hopping integral, for which we have used the symbol β.

A metallic SWNT has an electrical conductivity as high as 4×10^5 S/cm, and in theory, it can carry an electric current density of 4×10^9 A/cm^2, which is more than 1,000 times greater than copper. On the other hand, semiconducting SWNT shows on/off ration as high as 10^6 and mobility as high as 10^5 cm^2 /s/V.[37, 38] The electrical properties of semiconducting SWNT are sensitive to chemical

and environmental doping. This rich variety of electronic properties potentially provides all of the necessary components for electrical circuit fabrication and allows the development of SWNT based nanoelectronics.

The unique electronic properties of the carbon nanotube are the result of the quantum confinement of the electrons in one dimension and ballistic conduction has been observed in carbon nanotubes. [39] Electrons behave very differently in systems of different dimensionality as illustrated by energy dependence of the electronic density of states presented in Figure 1.7.[40] For a 3D system, the DOS is a continuous function of energy, and E_0 might correspond to an energy threshold for the onset of optical transitions, or a band gap energy E_g in a semiconductor (Figure 1.7(a)). For a 2 D system, within a given sub-band, the 2D density of states function is energy-independent, and the energy gap E_g corresponds to the band edge energy of the lowest sub-band (Figure 1.7(b)). For a 1D system, the DOS shows sharp spike-like peaks that are called van Hove singularities, and energy gap E_g would correspond to a van Hove singularity in the density of states occurring at the corresponding sub-band edge, where the magnitude of the electronic DOS becomes very large (Figure 1.7(c)). In case of 0D, the levels are completely discrete (Figure 1.7(d)).

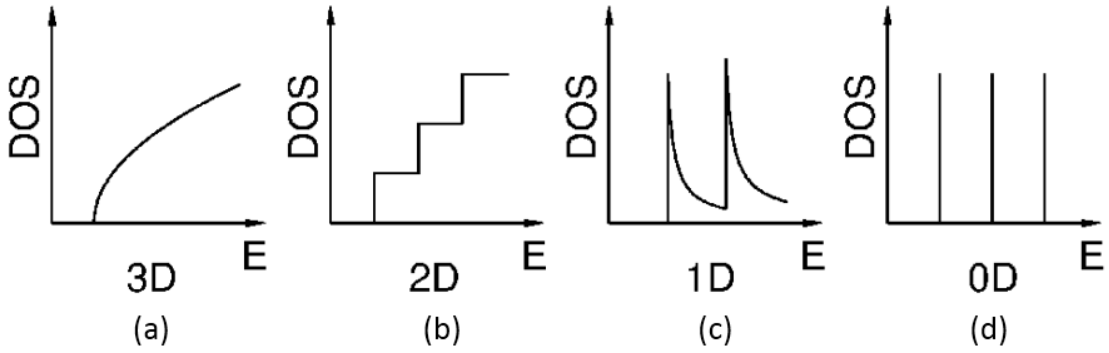

Figure 1.7: Idealized electronic density of states of (a) 3D system. (b) 2D system. (c) 1D system and (d) 0D system.

The covalent sp^2 bond formed between the carbon atoms is one of the strongest chemical bonds in an extended system known in nature, and it makes the CNT the strongest material in terms of tensile strength and elastic modulus. SWNTs were synthesized with the highest aspect (length-to-diameter) ratio of up to 132,000,000:1, [41] and the strongest fabric was fabricated by using SWNTs. [42]

Theoretical studies predicted that CNTs are very good thermal conductors along the tube, exhibiting a property known as "ballistic conduction". [43] The measured room-temperature thermal conductivity along the axis of individual SWNT is about 3500 $W \cdot m^{-1} \cdot K^{-1}$,[44] which is higher than that of natural diamond at about 2000 $W \cdot m^{-1} \cdot K^{-1}$.[45]

1.3 Thin films of SWNTs

Individual SWNTs possess remarkable physical properties, such as high mechanical strength, nanometer scale diameter, high thermal conductivity, high on/off ratio in semiconducting nanotube FET, and ultra-high electrical conductivity in metallic nanotubes. However, there are major challenges in finding a feasible technology to assemble the individual nanotubes into micro-electro-mechanical systems (MEMS) or electronic circuits; such technology is not yet in place for commercial fabrication. One possible solution is to use networks of carbon nanotubes in the form of thin films or buckypapers,[46, 47] instead of individual SWNTs.

1.3.1 Bulk SWNT materials

Bulk quantities of SWNTs can be produced by three major methods: arc discharge (EA), laser ablation, and chemical vapor deposition (CVD). Each method has its advantage and challenges. Based on the synthetic techniques, there are: EA-SWNTs, Laser-SWNTs, and CVD produced SWNTs including CVD-SWNT, HiPco-SWNTs and CoMoCat-SWNTs. The bulk nanotube material produced by most methods is in the form of soot, which contains 10-70% impurities in weight,[48-52] including amorphous carbon, graphitic nanoparticle and metal catalyst. The bulk SWNTs samples usually do not contain a single type of SWNTs, but a mixture of semiconducting and metallic SWNTs, with a distribution of diameter, length and chirality. Statistically, the metallic to semiconducting

SWNTs ratio is close to 1:2, which has been verified in experiments.[53] It is still especially challenging to produce SWNTs of controlled diameter, length and chirality to meet the specific requirements of the various applications.

1.3.2 Optical properties of bulk SWNT materials

Individual SWNTs are too small to be studied with traditional optical technologies. Spectroscopy is one of the most powerful methods for characterizing bulk carbon nanomaterials, such as purified SWNT dispersions and SWNT thin films. Figure 1.8 (a) shows the typical absorption spectrum of a nanotube film, and Figure 1.8 (b) shows the absorption spectrum of a nanotube solution. Some pronounced absorption peaks can be observed in IR spectral range and their structure can be explained by the density of states of SWNT (Figure 1.8 (c)). The S_{11} and S_{22} peak are related to the first and second interband transitions in the semiconducting nanotubes, while M_{11} peak is related to the first interband transition in the metallic nanotubes. In the typical spectrum of the bulk material,l interband transitions arising from both metallic and semiconducting tubes can be seen, because of the mixture of both types of the SWNTs. It is interesting that bulk SWNT film, which is 2D in geometry, shows the 1D DOS features corresponding to individual SWNTs.

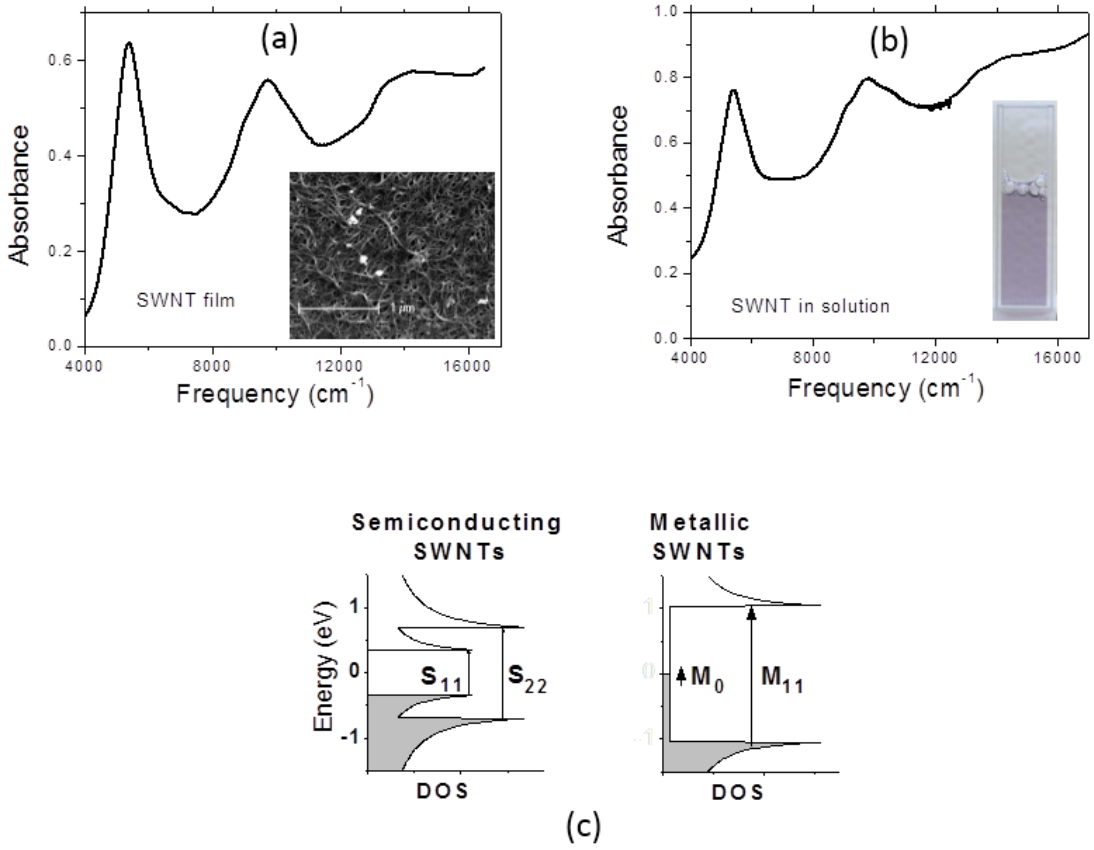

Figure 1.8: Absorption spectra of (a) SWNT thin film (thickness ~ 70 nm), and (b) SWNT solution (concentration at a concentration of 0.5 mg/mL). (c) DOS of SWNTs.

1.3.3 Processing of SWNTs

1.3.3.1 Dispersion of SWNTs

Once the SWNT materials are made, materials processing always starts with dispersion of SWNTs: it is important to keep the carbon nanotubes well-separated in solution. Because of the large van der Waals forces, SWNTs are usually bundled together. It is hard to separate nanotube bundles in solution. In Haddon research group, several techniques are used to promote the solubility of

SWNTs: 1) surfactants may be used as dispersion aids, including anionic, cationic, nonionic surfactants and various polymers;[54] 2) dispersions may be prepared in organic solvents; [55] 3) covalent functionalization may be used to enhance solubility.[56] As prepared (AP) SWNTs can be separated and dispersed by ultra-sonication by surfactant stabilization in aqueous solution. The most widely used surfactants are the anionic surfactant cetyltrimethylammonium bromide (CTAB), sodium dodecylbenzene sulfonate (NaDDBS), and cationic surfactant sodium dodecyl sulfate (SDS).[57] Carbon nanotube dispersions can also be made without surfactant, by using organic solvents which contain the amide functionality. The most widely used organic solvents are N, N-Dimethylformamide (DMF), N,N-Dimethylacetamide (DMAC) and N-Methyl-2-pyrrolidone (NMP). Covalent functionalization has also been used to improve the solubility of nanotubes,[58] but can lower their electrical conductivity. Depending on the application requirements, various functionalities can be covalently attached to the ends or side-walls of the SWNTs, resulting in soluble functionalized SWNT materials (Figure 1.9). [56, 59-61]

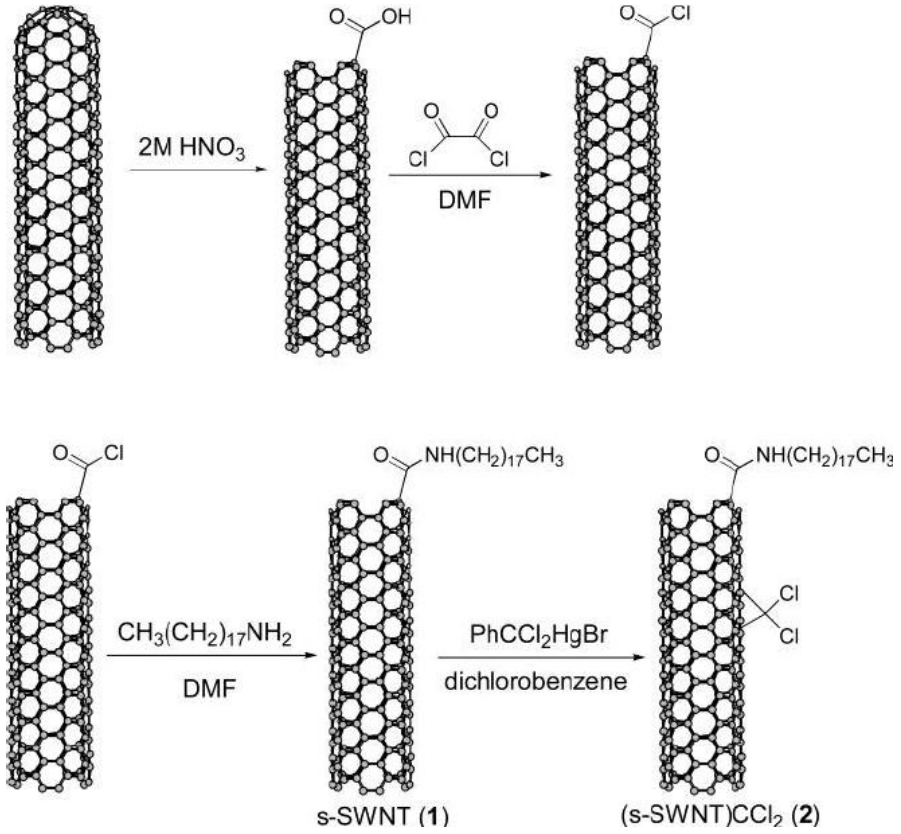

Figure 1.9: End-wall and side-wall functionalization of SWNTs: dissolution and dichlorocarbene reactions of SWNTs.[59]

1.3.3.2 Purification of SWNTs

The impurities in as-prepared SWNTs usually have to be removed in order to realize the intrinsic properties of the SWNTs. A number of purification methods have been applied to remove the impurities, such as gas phase purification, [62] and liquid phase purification.[63-73] The purification of SWNTs is difficult, because the CNTs are highly entangled and bundled, and both the SWNTs and the carbonaceous impurities are hardly soluble and nonvolatile. Haddon research group has earned a great reputation in liquid phase purification.

1.3.3.3 Optical technique for purity evaluation of SWNTs

In order to estimate the efficiency of the purification process and the quality of nanotube materials, it is very important to evaluate the purity of bulk SWNT materials. Microscopic techniques (SEM, TEM and AFM) have traditionally been the most important techniques to characterize carbon nanotubes.[74] However, the amount of material that can be seen and analyzed within one SEM frame (Figure 1. 10) is less than a pg and the material quality varies widely within the same sample, thus making it statistically impossible to obtain representative information about the bulk samples of 10g or more, that are produced by current manufacturing techniques. In additional, thermogravimetric analysis (TGA) and Raman spectroscopy have been used to characterize the purity of SWNT materials. TGA is routinely used to evaluate the amount of metal components in the SWNT materials. Raman spectroscopy is used to evaluate the carbonaceous impurity of bulk quantities of single-walled carbon nanotubes.

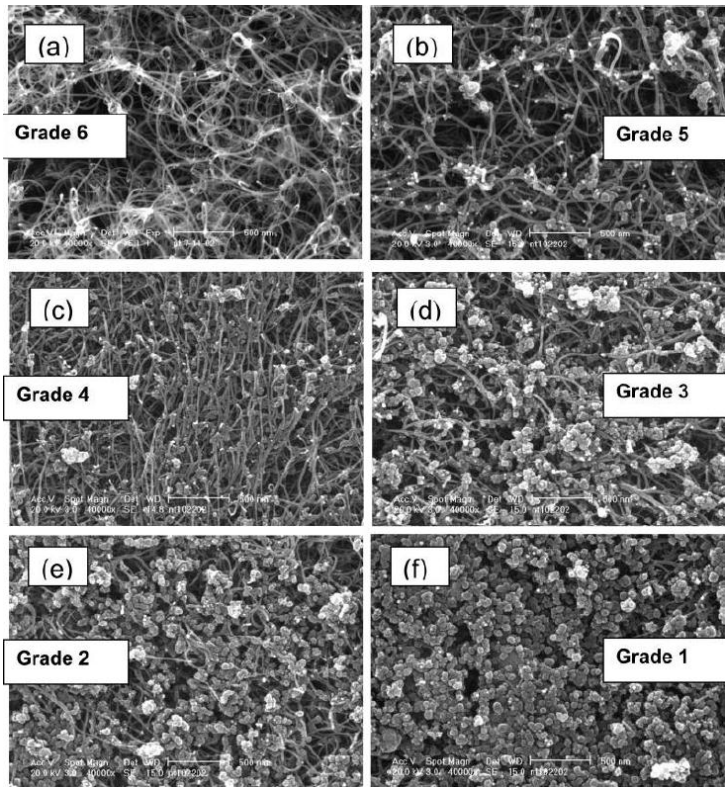

Figure 1.10: SEM images of AP-SWNT soot collected in the electric arc chamber. SEM purity grading system shows highest purity grade 6 to lowest grade 1. Note that images b-f (grades 5-1) were obtained from samples taken from the same synthetic experiment. [74]

The Haddon group first suggested and developed the use of a near-infrared (NIR) spectroscopy procedure to quantitatively evaluate the relative purity of bulk quantities of single-walled carbon nanotubes.[55, 66, 74, 75]. Instead of the absolute purity, the relative purity of the SWNT materials is defined, in which the purity is evaluated against a reference sample by using the region of the second interband transition (S_{22}) for semiconducting SWNTs.

Consider the NIR spectrum of an EA-SWNT solution (dispersion), as shown schematically in Figure 11 in the spectral range between the far-IR and

the UV (10-45000 cm^{-1}). The absorption contributions ascribed to SWNTs and carbonaceous impurities are shown in different gray scales to illustrate the spectral components. The pure absorption bands S_{11}, S_{22}, and M_{11}, originating from the interband transitions, ride on the top of the plasmon absorption. It is intuitively understandable that the strength of pure absorption bands S_{11}, S_{22}, and M_{11} in comparison to the featureless baseline provides a measure of the purity of the SWNT material. The second semiconducting transition is chosen for the purity evaluation, because the S_{22} transition is less susceptible to the doping due to material processing and exposure to the ambient atmosphere.

The relative carbonaceous purity of an arbitrary AP-SWNT sample against the reference sample is calculated by comparison of the ratio of the areal absorbance of pure S_{22} interband transition to the total areal absorbance in the S_{22} spectral region:

$$P_{sample} = \frac{AA(S_{22})_{sample}/AA(T)_{sample}}{AA(S_{22})_{reference}/AA(T)_{reference}} \times 100 \quad (1.20)$$

$$= \frac{AA(S_{22})_{sample}/AA(T)_{sample}}{0.141} \times 100 \quad (1.21)$$

where $AA(T)_{sample}$ and $AA(T)_{reference}$ are the total areas under the spectral curves given in figure, and $AA(S_{22})_{sample}$ and $AA(T)_{reference}$ are the areas under the S_{22} absorptions for the evaluated and reference samples, respectively. The ratio $AA(S_{22})_{reference}/AA(T)_{reference}$ is taken to be 0.141, which corresponds to 100% purity in the reference sample and thus leads to a practical definition of the relative purity (RP).

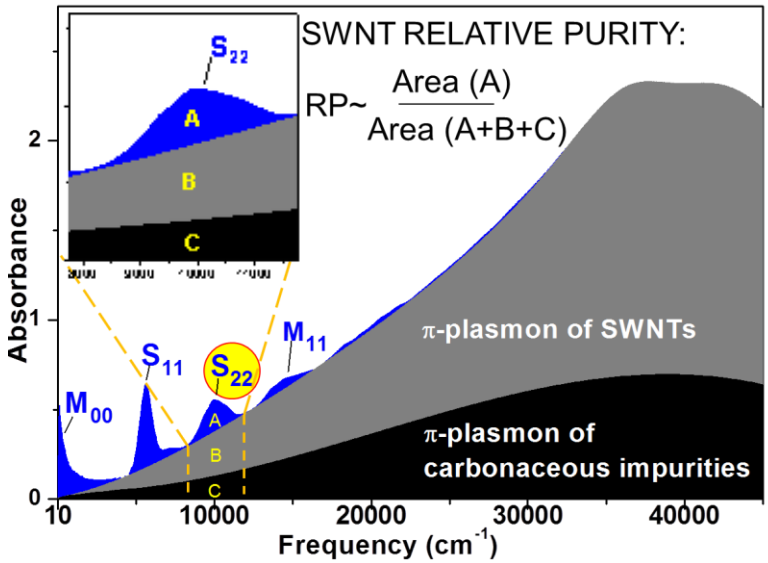

Figure 1.11: Schematic illustration of the electronic spectrum of EA-SWNTs.

1.3.3.4 Separation of semiconducting and metallic SWNTs

In some cases, SWNTs with a narrow distribution of size or chirality has to be isolated and the separation of semiconducting and metallic SWNTs is particularly important. There are several methods of separating semiconducting and metallic CNTs, including: 1) current-induced oxidation of metallic nanotubes reported by IBM; [76] 2) alternating current electrophoresis; [77] 3) density-gradient ultracentrifugation. [78-81] The density-gradient ultracentrifugation is suitable for relatively large-scale technological processes. The density-gradient ultracentrifugation separates surfactant-wrapped nanotubes by differences in their buoyant density. Narrow diameter distributions of within a 0.02-nm can be isolated and it is theoretically possible to isolate a single type of SWNT. As a

result, solutions containing either metallic SWNTs or semiconducting SWNTs can be obtained (Figure 1.12).

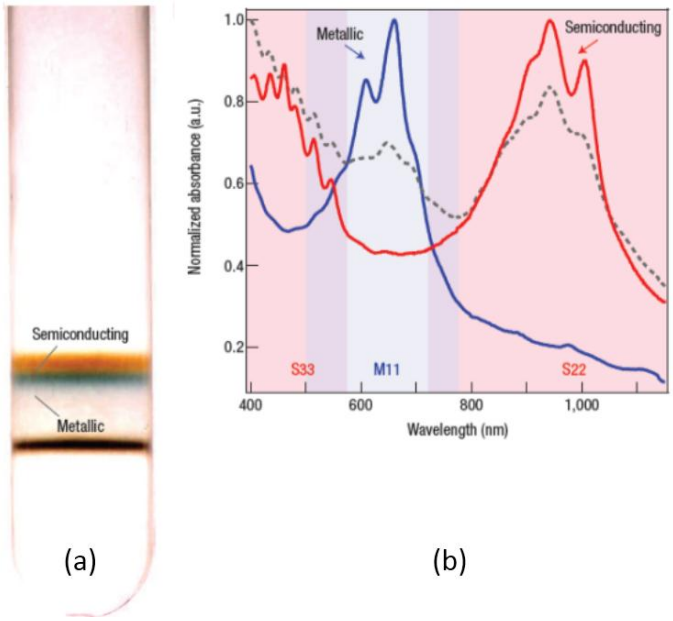

Figure 1.12: (a) Photograph of laser-ablation-grown SWNTs separated in a co-surfactant solution. The top band (orange) corresponds to predominantly semiconducting SWNTs and the band just below it (green) is highly enriched in metallic SWNTs (b) absorbance spectra of isolated semiconducting SWNTs and metallic SWNTs.[78]

1.3.4 Fabrication of SWNTs

SWNT thin film fabrication techniques can be classified into two types: 1) direct growth in which as-prepared (AP) SWNT thin films can form in the CNT synthesis process; 2) solution-based deposition, which first requires CNT purification and dispersion in a solvent.

1.3.4.1 Direct growth

CNT films can be grown directly during the synthesis process, without dispersion and purification steps. The obtained CNT film consists of pristine low defects SWNTs, which are not damaged during the nanotube purification processing.[82, 83]

CVD can grow SWNT films either randomly distributed or aligned. In the CVD method, catalyst nanoparticles on substrates are used as seeds for SWNT growth. CVD can grow SWNT films with vertically aligned SWNTs, as shown in Figure 1.13, [84] which have unique properties and applications, such as in field emission devices and supercapacitors.

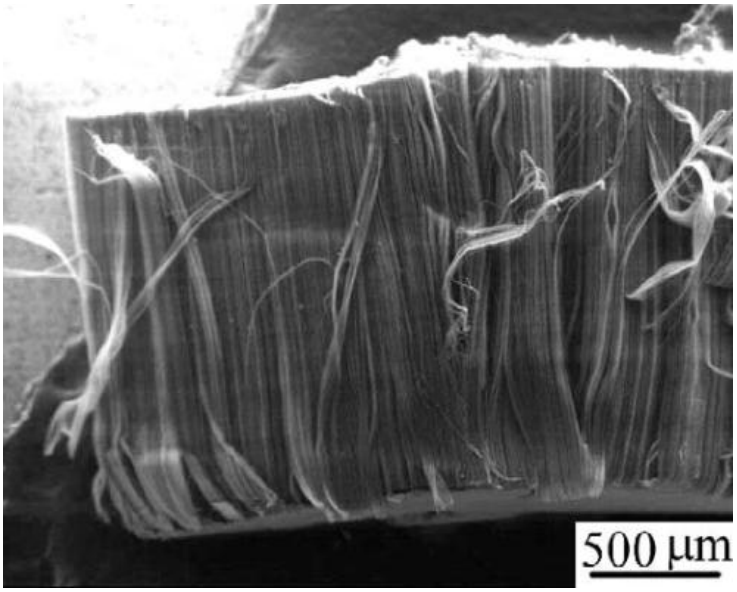

Figure 1.13: SEM image of self-aligned SWNTs grown by CVD method, showing that the CNTs are well-aligned, closely contacted, and clean. [84]

In Haddon research group, thin films of as-prepared SWNTs were assembled during electric arc discharge process.[82] A stainless steel wire grid of

cell size 2.54 × 2.54 cm was placed near the plasma zone inside the electric arc chamber. The growing SWNTs drift from the plasma core toward the water-cooled walls of the arc reactor, and the wire grid nucleates the growth of an extended SWNT network that forms a continuous semitransparent SWNT film after several minutes of operation of the electric arc (Figure 1.14). By this process, a high-purity, loose SWNT film was fabricated.

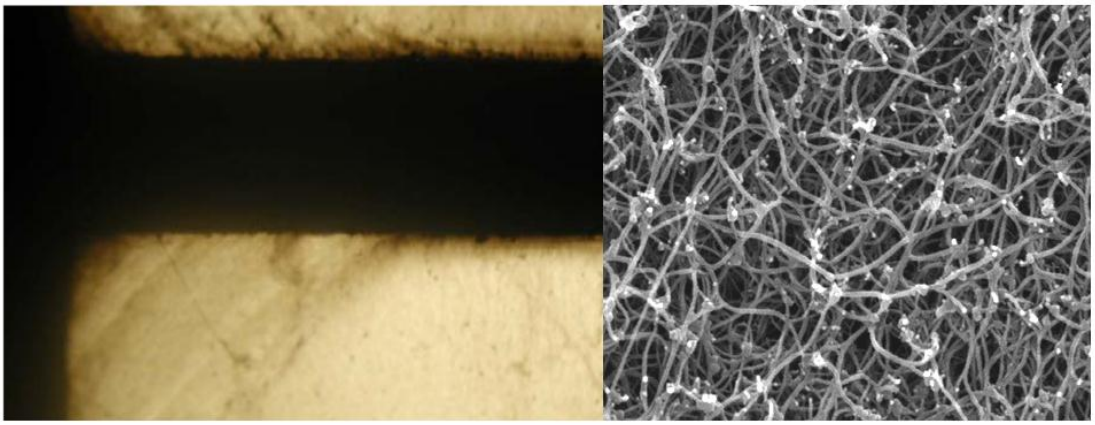

Figure 1.14: (a) Photograph of semi-transparent film of AP-SWNTs formed on a wire grid during the electric arc synthesis. (b) SEM image of the loose SWNT network.

1.3.4.2 Solution-based deposition

Solution-based film coatings have generated widespread interest in both industry and academia. Solution based depositions, which are started with CNT suspensions, include vacuum filtration, drop-drying from solvent, airbrushing, and Langmuir-Blodgett deposition. These processes usually grow dense SWNT films, as shown in Figure 1.15.[82]

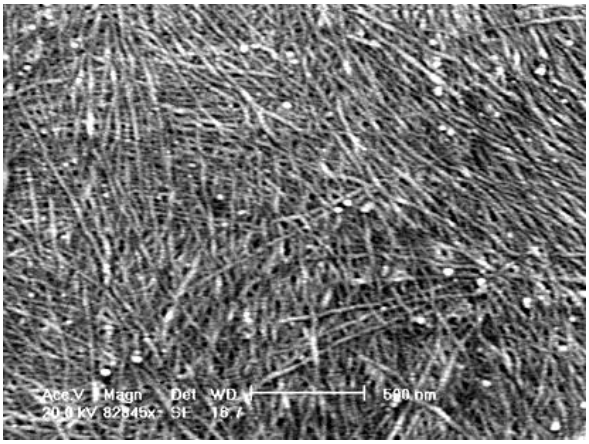

Figure 1.15: SEM image of the dense SWNT network.

In the Haddon group, most of the SWNT thin films used for device fabrication are prepared by the vacuum filtration method[82, 85, 86] by the following steps (Figure 1.16): 1) vacuum-filtration of a dilute suspension of purified nanotubes on the filtration membrane (forming the homogeneous film on the membrane); 2) washing away the surfactant with purified water and isopropanol (IIPA); 3) dissolving the filtration membrane in solvent; 4) transfer of the film to the desired substrate if necessary, followed by patterning of the nanotube thin film if needed.

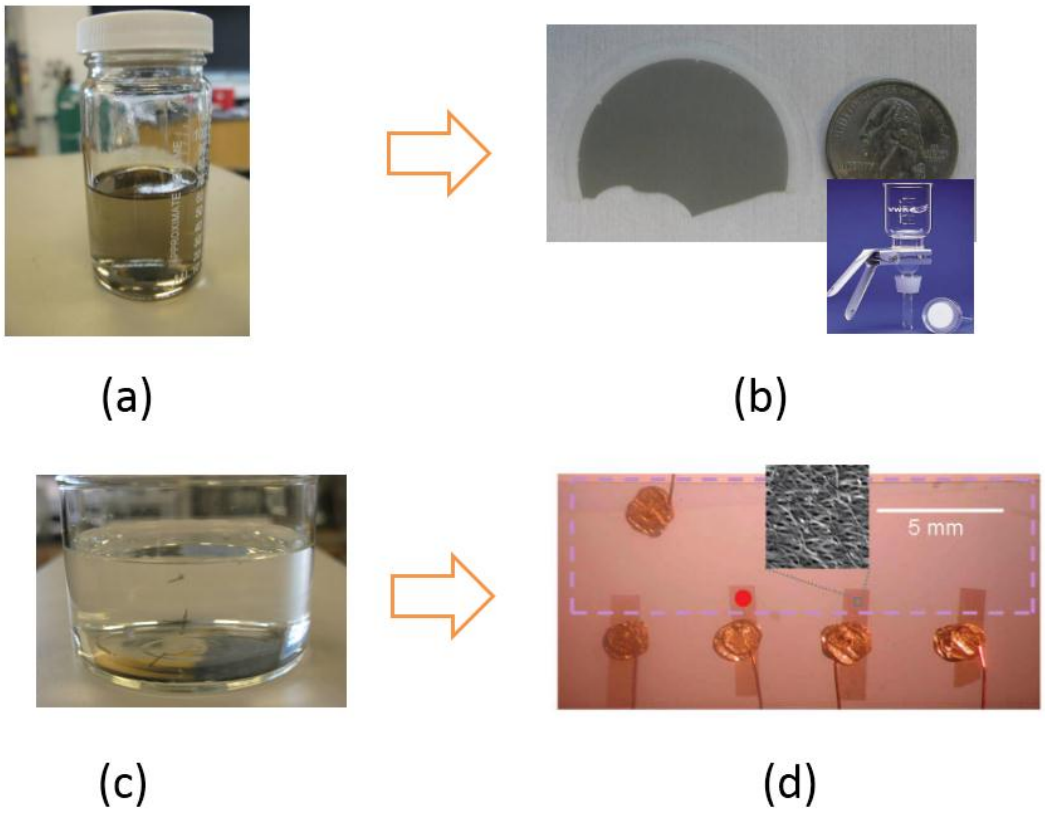

Figure 1.16: Vacuum filtration steps (a) Prepare diluted suspension of purified nanotubes. (b) Vacuum- filtration of a dilute suspension of purified nanotubes on the filtration membrane. (c) Dissolution of the membrane to leave SWNT thin film floating in solvent (water). (d) Transfer of SWNT films to substrate to form SWNT thin film based device.

The vacuum filtration method has several advantages:[46, 47] 1) it is a low temperature process, compatible with plastic substrates; 2) homogeneity of the films can be guaranteed by the process itself; 3) the film thickness can be controlled with nano-scale precision by the amount of the SWNT material utilized for the vacuum filtration. Compared with other solution-based deposition, vacuum filtration method can minimize unwanted organic solvent residue or surfactant by post cleaning steps.

1.3.5 Application of SWNT thin films

Carbon nanomaterial films are light, flexible, thermally stable and chemically inert. Carbon nanotube thin films are usually highly conductive, transparent and can be manufactured in large area. The SWNT thin films are promising materials in chemical sensor applications, transparent conducting electrodes, fuel cells, and optoelectronics.

Because of the large surface to volume ratio, nanotube random networks were used for chemical detection of gases and chemical vapors.[87-93] The SWNT network gas sensor is based on a charge transduction mechanism.[94] Single-walled carbon nanotubes networks have been demonstrated to be good sensing materials to detect a number of small gas molecules such as NO_2, NH_3 O_2 and water.[95-97] The Haddon group developed a gas sensor from functionalized SWNTs, which can detect a wide range of analytes with very low detection limit.[90, 98, 99] Those functionalized SWNT gas sensors exhibit enhanced sensitivity as compared to purified nanotubes.

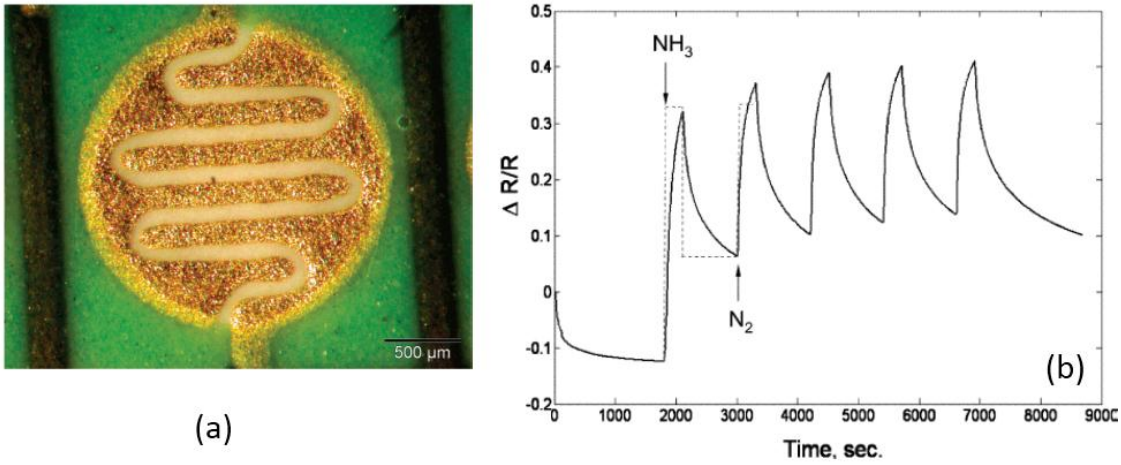

Figure 1.17: (a) Optical image of an interdigitated electrode from the sensor array, (b) Response curves of SWNT-PABS to 100 ppm NH_3.[90]

Since CNT film is thermally stable, chemically inert, and has high surface area, it has been engineered into fuel cell and supercapacitor devices.[100-103] The proton exchange membrane fuel cell (PEMFC) utilizing hydrogen as fuel has higher energy efficiency than that of the combustion engine. However, the catalysts that are currently being used such as Pt are too expensive. Haddon group is exploring the potential of SWNT thin films as a catalyst support for low Pt loading and prototypes of CNT based fuel cells with excellent performance have been demonstrated.[101, 102, 104-110]

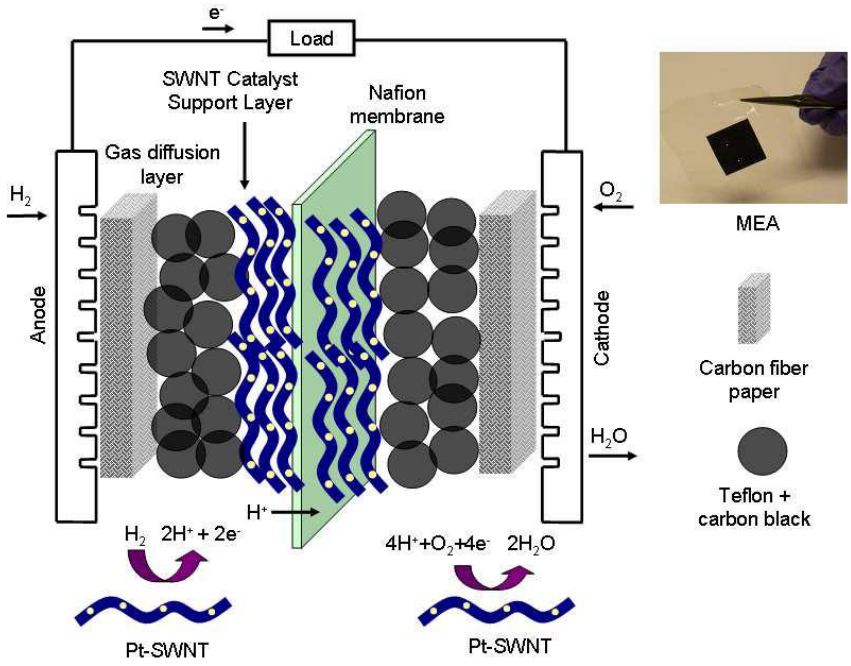

Figure 1.18: Carbon nanotube application in fuel cells.

Carbon nanotube thin films are highly conductive and transparent. SWNT films are being considered as a replacement for the brittle and expensive indium tin oxide (ITO) coated films which are now widely used as transparent conducting electrodes in LCD displays, solar cells, and solid state (OLED) lighting. [111-115] SWNT thin films are easy to cast from SWNT solution, they can be lithographically patterned, and the preparation of such films requires only very small amount of SWNT material.

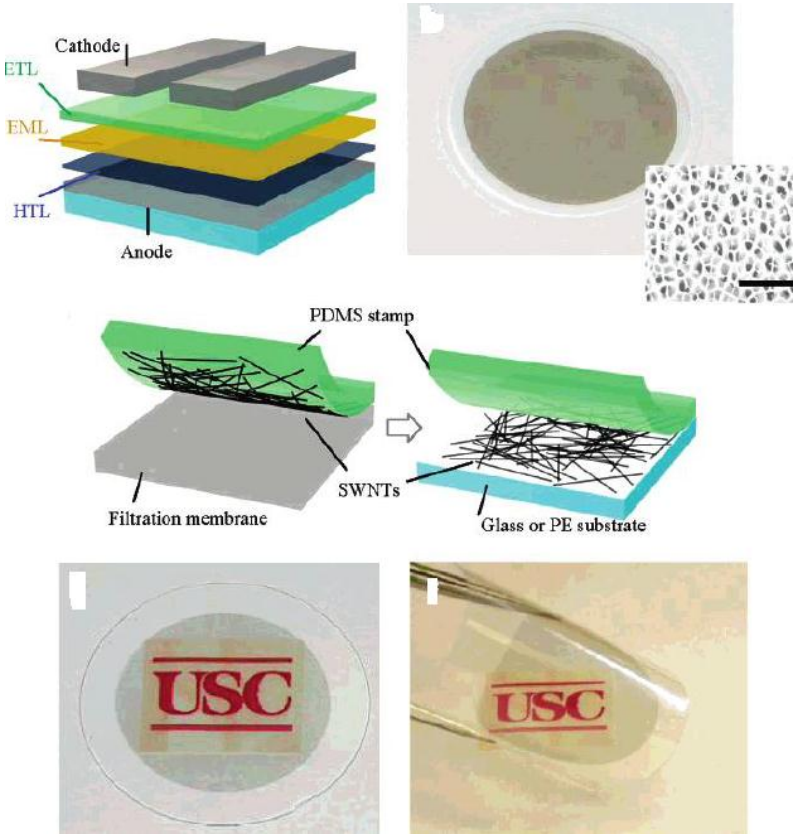

Figure 1.19: Fabrication of flexible transparent electrodes for OLED. [112]

SWNTs have recently emerged as a potential basis for new generation of optoelectronic devices.[82, 85, 86, 116-123] The Haddon research group has developed a number of carbon nanotube thin film based optoelectronic applications. Haddon group demonstrated that the SWNT photoresponse can be dramatically enhanced by suspending SWNT films in vacuum between electrical contacts to take advantage of the strong bolometric effect, as shown in Figure 1.20(a).[82] Two features of the SWNT film make it an ideal bolometric material: strong UV/Vis-NIR absorption and high negative value of the temperature coefficient of

resistance (TCR). The energy of the absorbed IR radiation is efficiently transferred to the crystal lattice through strong electron-phonon interactions that increase the temperature of the film, and the temperature increase results in a change in resistance. This development was followed by further utilization of SWNT thin film technology to assemble the first prototype of an integrated optoelectronic SWNT device, a SWNT optocoupler, in which both emitter and receiver are made of SWNT thin films, as shown in Figure 1.20(b).[85] In this device SWNT thin film emitter and SWNT thin film detector are mounted face-to-face on two sapphire rings. IR radiation from SWNT emitter (on the bottom) caused by electrical current passing through SWNT film can be sensed by the SWNT bolometric detector (on the top). SWNT emitter and detector are controlled by two isolated electronic circuits, so electrical signals can be transmitted using optical channel without electrical coupling.

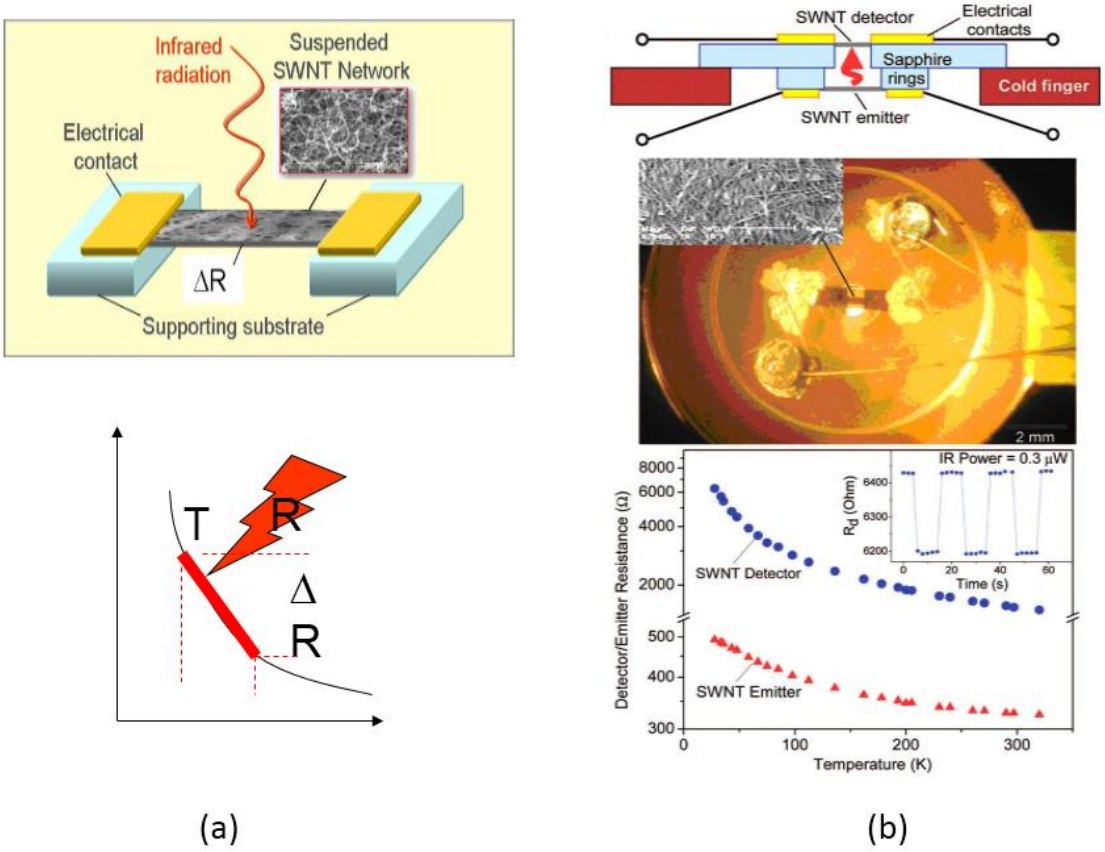

Figure 1.20: (a) High TCR SWNT network suspended between electrical contacts as bolometer.[82] (b) SWNT optocoupler: SWNT thin film emitter and detector are mounted face-to-face on two sapphire rings so the radiation from SWNT emitter can be sensed by the detector.[85]

References:

1. Kroto, H. W., Heath, J. R., O'Brien, S. C., Curl, R. F. & Smalley, R. E. C60: Buckminsterfullerene. Nature 318, 162-164 (1985).
2. Iijima, S. Helical Microtubules of Graphitic Carbon. Nature 354, 56-58 (1991).
3. Novoselov, K. S. et al. Electric Field Effect in Atomically Thin Carbon Films. Science 306, 666-669 (2004).
4. Novoselov, K. S. et al. Two-dimensional Gas of Massless Dirac Fermions in Graphene. Nature 438, 197-200 (2005).
5. Castro Neto, A. H., Guinea, F., Peres, N. M. R., Novoselov, K. S. & Geim, A. K. The Electronic Properties of Graphene. Rev. Mod. Phys. 81, 109-162 (2009).
6. Sarma, S. D., Adam, S., Hwang, E. H. & Rossi, E. Electronic Transport in Two-dimensional Graphene. Rev. Mod. Phys. 83, 407-470 (2011).
7. Wallace, P. R. The Band Theory of Graphite. Phys. Rev. 71, 622-634 (1947).
8. Saito, R., Dresselhaus, G. & Dresselhaus, M. S. Physical Properties of Carbon Nanotubes (Imperial College Press, Singapore, 1998).
9. Saito, R., Fujita, M., Dresselhaus, G. & Dresselhaus, M. S. Electronic Structure of Chiral Graphene Tubules. Appl. Phys. Lett. 60, 2204 (1992).
10. Chen, J. H., Jang, C., Xiao, S. D., Ishigami, M. & Fuhrer, M. S. Intrinsic and Extrinsic Performance Limits of Graphene Devices on SiO_2. Nature Nanotech. 3, 206-209 (2008).
11. Pisana, S. et al. Breakdown of the Adiabatic Born-Oppenheimer Approximation in Graphene. Nature Mater. 6, 198-201 (2007).
12. Schedin, F. et al. Detection of Individual Gas Molecules Adsorbed on Graphene. Nat. Mater. 6, 652-655 (2007).
13. Elias, D. C. et al. Control of Graphene's Properties by Reversible Hydrogenation: Evidence for Graphane. Science 323, 610-613 (2009).
14. Bekyarova, E. et al. Chemical Modification of Epitaxial Graphene: Spontaneous Grafting of Aryl Groups. J. Am. Chem. Soc. 131, 1336-1337 (2009).
15. Sarkar, S., Niyogi, S., Bekyarova, E. & Haddon, R. C. Organometallic Chemistry of Extended Periodic p-Electron Systems: Hexahapto-Chromium Complexes of Graphene and Single-Walled Carbon Nanotubes. Chem. Sci. 2, 1326-1333 (2011).
16. Hong, J. et al. Effect of Nitrophenyl Functionalization on the Magnetic Properties of Epitaxial Graphene. Small 7, 1175-1180 (2011).
17. Sarkar, S., Bekyarova, E., Niyogi, S. & Haddon, R. C. Diels-Alder Chemistry of Graphite and Graphene: Graphene as Diene and Dienophile. J. Am. Chem. Soc. 133, 3324-3327 (2011).

18. Niyogi, S. et al. Covalent Chemistry for Graphene Electronics. J. Phys. Chem. Lett. 2, 2487-2498 (2011).
19. Sarkar, S., Bekyarova, E. & Haddon, R. C. Chemistry at the Dirac Point: Diels-Alder Reactivity of Graphene. Acc. Chem. Res. 45, 673-682 (2012).
20. Sarkar, S., Bekyarova, E. & Haddon, R. C. Reversible Grafting of a-Naphthylmethyl Radicals to Epitaxial Graphene. Angew. Chem. Int. Ed. 51, 4901-4904 (2012).
21. Sarkar, S., Bekyarova, E. & Haddon, R. C. Covalent Chemistry in Graphene Electronics. Mater. Today 15, 276-285 (2012).
22. Sarkar, S. et al. Organometallic Hexahapto Functionalization of Single Layer Graphene as a Route to High Mobility Graphene Devices. Adv. Mater. DOI: 10.1002/adma.201203161 (2012).
23. Bekyarova, E. et al. Effect of Covalent Chemistry on the Electronic Structure and Properties of Carbon Nanotubes and Graphene. Acc. Chem. Res. accepted (2012).
24. Katsnelson, M. I., Novoselov, K. S. & Geim, A. K. Chiral Tunnelling and the Klein Paradox in Graphene. Nature Phys. 2, 620-625 (2006).
25. Geim, A. K. & Novoselov, K. S. The Rise of Graphene. Nat. Mater. 6, 183-191 (2007).
26. Martino, A. D., Dell'Anna, L. & Egger, R. Magnetic Confinement of Massless Dirac Fermions in Graphene. Phys Rev. Lett. 98, 6802-6805 (2007).
27. Bethune, D. S. et al. Cobalt-Catalized Growth of Carbon Nanotubes with Single-Atomic-Layer Walls. Nature 363, 605-607 (1993).
28. Iijima, S. & Ichihashi, T. Single-Shell Carbon Nanotubes of 1-nm Diameter. Nature 363, 603-605 (1993).
29. Dresselhaus, M. S., Dresselhaus, G. & Avouris, P. (eds.) Carbon Nanotubes: Synthesis, Structure, Properties and Applications (Springer-Verlag, Berlin, 2001).
30. Dresselhaus, M. S., Dresselhaus, G. & Jorio, A. Carbon Nanotubes: Advanced Topics in the Synthesis, Structure, Properties and Applications (Springler-Verlag New York, 2008).
31. White, C. T. & Mintmire, J. W. Nature 394, 29 (1998).
32. Mintmire, J. W. & White, C. T. Universal Density of States for Carbon Nanotubes. Phys. Rev. Lett. 81, 2506-2509 (1998).
33. Ajayan, P. M. Nanotubes from Carbon. Chem. Rev. 99, 1787-1799 (1999).
34. Martel, R., Schmidt, T., Shea, H. R., Hertel, T. & Avouris, P. Single- and Multi-Wall Carbon Nanotube Field-Effect Transistors. Appl. Phys. Lett 73, 2447-9 (1998).
35. Kataura, H. et al. Optical Properties of Single-Wall Carbon Nanotubes. Synth. Met. 103, 2555-2558 (1999).
36. Kataura, H. et al. Diameter Control of the Single-Walled Carbon Nanotubes. Carbon 38, 1691-1697 (2000).

37. Durkop, T., Getty, S. A., Cobas, E. & Fuhrer, M. S. Extraordinary Mobility in Semiconducting Carbon Nanotubes. Nano Lett. 4, 35-39 (2004).
38. Dai, H. Carbon Nanotubes: Synthesis, Integration, and Properties. Acc. Chem. Res. 35, 1035-1044 (2002).
39. Frank, S., Poncharal, P., Wang, Z. L. & de Heer, W. A. Carbon Nanotube Quantum Resistors. Science 280, 1744-1746 (1998).
40. Samsonidze, G. G. et al. The Concept of Cutting Lines in Carbon Nanotube Science. J. Nanosci. Nanotech. 3, 431-458 (2003).
41. Wang, X. et al. Fabrication of Ultralong and Electrically Uniform Single-walled Carbon Nanotubes on Clean Substrates. Nano Lett. 9, 3137-3141 (2009).
42. Dalton, A. B. et al. Super-Tough Carbon-Nanotube Fibres. Nature 423, 703 (2003).
43. Hone, J., Whitney, M., Piskoti, C. & Zettl, A. Thermal conductivity of single-walled carbon nanotubes. Physical Review B 59, R2514-R2516 (1999).
44. Kim, P., Shi, L., Majumdar, A. & McEuen, P. L. Thermal Transport Measurements of Individual Multiwalled Nanotubes. Phys. Rev. Lett. 87, 215502 (2001).
45. Yu, C., Shi, L., Yao, Z., Li, D. & Majumdar, A. Thermal Conductance and Thermopower of an Individual Single-Wall Carbon Nanotube. Nano Lett. 5, 1842-1846 (2005).
46. Wu, Z. et al. Transparent, Conductive Carbon Nanotube Films. Science 305, 1273-1276 (2004).
47. Hu, L. B., Hecht, D. S. & Gruner, G. Carbon Nanotube Thin Films: Fabrication, Properties, and Applications. Chem. Rev. 110, 5790-5844 (2010).
48. Journet, C. et al. Large Scale Production of Single-Walled Carbon Nanotubes by the Electric-Arc Technique. Nature 388, 756-758 (1997).
49. Rinzler, A. G. et al. Large-Scale Purification of Single-Wall Carbon Nanotubes: Process, Product and Characterization. Appl. Phys. A 67, 29-37 (1998).
50. Nikolaev, P. et al. Gas-Phase Catalytic Growth of Single-Walled Carbon Nanotubes from Carbon Monoxide. Chem. Phys. Lett. 313, 91-97 (1999).
51. Zhou, W. et al. Structural Characterization and Diameter-Dependent Oxidative Stability of Single Wall Carbon Nanotubes Synthesized by the Catalytic Decomposition of CO. Chem. Phys. Lett. 350, 6-14 (2001).
52. Chiang, I. W. et al. Purification and Characterization of Single-Wall Carbon Nanotubes(SWNTs) Obtained From The Gas-Phase Decomposition of CO (HiPco Process). J. Phys. Chem. B 105, 8297-8301 (2001).
53. Naumov, A. V. et al. Quantifying the Semiconducting Fraction in Single-Walled Carbon Nanotube Samples through Comparative Atomic Force and Photoluminescence Microscopies. Nano Lett. 9, 3203-3208 (2009).

54. Vaisman, L., Marom, G. & Wagner, H. D. Dispersions of surface-modified carbon nanotubes in water-soluble and water-insoluble polymers. Adv. Func, Mater. 16, 357-363 (2006).
55. Itkis, M. E. et al. Purity Evaluation of As-Prepared Single-Walled Carbon Nanotube Soot by Use of Solution Phase Near-IR Spectroscopy. Nano Lett. 3, 309-314 (2003).
56. Chen, J. et al. Solution Properties of Single-Walled Carbon Nanotubes. Science 282, 95-98 (1998).
57. Islam, M. F., Rojas, E., Bergey, D. M., Johnson, A. T. & Yodh, A. G. High Weight Fraction Surfactant Solubilization of Single-Wall Carbon Nanotubes in Water. Nano Lett. 3, 269-273 (2003).
58. Niyogi, S. et al. Chemistry of Single-Walled Carbon Nanotubes. Acc. Chem. Res. 35, 1105-1113 (2002).
59. Hu, H. et al. Sidewall Functionalization of Single-Walled Carbon Nanotubes by Addition of Dichlorocarbene. J. Am. Chem. Soc. 125, 14893-14900 (2003).
60. Kamaras, K., Itkis, M. E., Hu, H., Zhao, B. & Haddon, R. C. Covalent Bond Formation to a Carbon Nanotube Metal. Science 301, 1501 (2003).
61. Kamaras, K. et al. Effect of Physical and Chemical Doping on Optical Properties of SWNTs. AIP Conf. Proceedings 723, 197-200 (2004).
62. Ebbesen, T. W. et al. Decoration of Carbon Nanotubes. Adv. Mater. 8, 155-157 (1996).
63. Harris, P. J. F. Carbon Nanotubes and Related Structures: New Materials for the Twenty-first Century (Cambridge University Press, Cambridge, U.K., 1999).
64. Niyogi, S. et al. Chromatographic Purification of Soluble Single-Walled Carbon Nanotubes (s-SWNTs). J. Am. Chem. Soc. 123, 733-734 (2001).
65. Zhao, B. et al. Chromatographic Purification and Properties of Soluble Single Walled Carbon Nanotubes. J. Am. Chem. Soc. 123, 11673-11677 (2001).
66. Niyogi, S., Kang, C. B., Perea, D., Itkis, M. E. & Haddon, R. C. Purification of Single-Walled Carbon Nanotubes. Chem. Phys. Lett. In Press (2003).
67. Sen, R., Rickard, S. M., Itkis, M. E. & Haddon, R. C. Controlled Purification of Single-Walled Carbon Nanotube Films by Use of Selective Oxidation and Near-IR Spectroscopy. Chem. Mater. 15, 4273-4279 (2003).
68. Hu, H., Zhao, B., Itkis, M. E. & Haddon, R. C. Nitric Acid Purification of Single-Walled Carbon Nanotubes. J. Phys. Chem. B 107, 13838-13842 (2003).
69. Haddon, R. C., Sippel, J., Rinzler, A. G. & Papadimitrakopoulos, F. Purification and Separation of Carbon Nanotubes. MRS Bull. 29, 252-259 (2004).
70. Hu, H. et al. Influence of the Zeta Potential on the Dispersability and Purification of Single-Walled Carbon Nanotubes. J. Phys. Chem. B 109, 11520-11524 (2005).

71. Yu, A. et al. Application of Centrifugation to the Large-Scale Purification of Electric Arc Produced Single-Walled Carbon Nanotubes. J. Am. Chem. Soc. 128, 9902-9908 (2006).
72. Smith, J. G. et al. Preparation and Properties of Nanocomposites from Pristine and Modified SWCNTs of Comparable Average Aspect Ratios. High Performance Polymers 20, 567-587 (2008).
73. Worsley, K. A., Kalinina, I., Bekyarova, E. & Haddon, R. C. Functionalization and Dissolution of Nitric Acid Treated Single-Walled Carbon Nanotubes. J. Am. Chem. Soc. 131, 18153-18158 (2009).
74. Itkis, M. E., Perea, D., Jung, R., Niyogi, S. & Haddon, R. C. Comparison of Analytical Techniques for Purity Evaluation of Single-Walled Carbon Nanotubes. J. Am. Chem. Soc. 127, 3439-3448 (2005).
75. Sen, R., Rickard, S. M., Itkis, M. E. & Haddon, R. C. in Proceedings of the NATO Advanced Study Institute on Organic Conductors, Superconductors and Magnets: From Synthesis to Molecular Electronics (eds. Ouahab, L. & Yagubskii, E.) 143-155 (Kluwer, Corfu, Greece, 2004).
76. Collins, P. G., Arnold, M. S. & Avouris, P. Engineering Carbon Nanotubes and Nanotube Circuits Using Electrical Breakdown. Science 292, 706-709 (2001).
77. Krupke, R., Hennrich, F., v.Lohneysen, H. & Kappes, M. M. Separation of Metallic from Semiconducting Single-Walled Carbon Nanotubes. Science 301, 344-347 (2003).
78. Arnold, M. S., Green, A. A., Hulvat, J. F., Stupp, S. I. & Hersam, M. C. Sorting carbon nanotubes by electronic structure using density differentiation. Nature Nanotechnology 1, 60-65 (2006).
79. Frank, O., Kavan, L., Green, A. A., Hersam, M. C. & Dunsch, L. In-Situ Vis/NIR Spectroelectrochemistry of Single-Walled Carbon Nanotubes Enriched with (6,5) Tubes. Phys. Stat. Sol. 245, 2239-2242 (2008).
80. Green, A. A., Duch, M. C. & Hersam, M. C. Isolation of Single-Walled Carbon Nanotube Enantiomers by Density Differentiation. Nano Res 2, 69-77 (2009).
81. Hossain, M. Z., Walsh, M. & Hersam, M. C. Scanning Tunneling Microscopy, Spectroscopy, and Nanolithography of Epitaxial graphene Chemically Modified with Aryl Moieties. J. Am. Chem. Soc. 132, 15399-15403 (2010).
82. Itkis, M. E., Borondics, F., Yu, A. & Haddon, R. C. Bolometric Infrared Photoresponse of Suspended Single-Walled Carbon Nanotube Films. Science 312, 413-416 (2006).
83. Zavodchikova, M. Y. et al. Novel Carbon Nanotube Network Deposition Technique for Electronic Device Fabrication. phys. stat. sol. (b) 245, 2272-2275 (2008).
84. Zhang, X. et al. Rapid Growth of Well-aligned Carbon Nanotube Arrays. Chem. Phys. Lett. 362, 285-290 (2002).

85. Itkis, M. E., Yu, A. & Haddon, R. C. Single-Walled Carbon Nanotube Thin Film Emitter-Detector Integrated Optoelectronic Device. Nano Lett. 8, 2224-2228 (2008).
86. Wang, F., Itkis, M. E. & Haddon, R. C. Enhanced Electromodulation of Infrared Transmittance in Semitransparent Films of Large Diameter Semiconducting Single-Walled Carbon Nanotubes. Nano Lett. 10, 937-942 (2010).
87. Feigel, I. M., Vedala, H. & Star, A. Biosensors Based on One-dimensional Nanostructures. J. Mater. Chem. 21, 8940-8954 (2011).
88. Ding, M. N., Tang, Y. F., Gou, P. P., Reber, M. J. & Star, A. Chemical Sensing with Polyaniline Coated Single-Walled Carbon Nanotubes. Adv. Mater. 23, 536-540 (2011).
89. Kauffman, D. R. & Star, A. Carbon Nanotube Gas and Vapor Sensors. Angew. Chem. Int. Ed. 47, 6550-6570 (2008).
90. Bekyarova, E. et al. Chemically Functionalized Single-Walled Carbon Nanotubes for Ammonia Sensors. J. Phys. Chem. B 108, 19717-19720 (2004).
91. Ghosh, S., Sood, A. K. & Kumar, N. Carbon Nanotube Flow Sensor. Science 299, 1042-1044 (2003).
92. Varghese, O. K. et al. Gas sensing characteristics of multi-wall carbon nanotubes. Sensors and Actuators B-Chemical 81, 32-41 (2001).
93. Kong, J. et al. Nanotube Molecular Wires as Chemical Sensors. Science 287, 622-625 (2000).
94. Bekyarova, E. et al. Mechanism of Ammonia Detection by Chemically Functionalized Single-Walled Carbon Nanotubes: In Situ Electrical and Optical Study of Gas Analyte Detection J. Am. Chem. Soc. 129, 10700-10706 (2007).
95. Kong, J. et al. Nanotube Molecular Wires as Chemical Sensors. Science 287, 622-625 (2000).
96. Collins, P. G., Bradley, K., Ishigami, M. & Zettl, A. Extreme Oxygen Sensitivity of Electronic Properties of Carbon Nanotubes. Science 287, 1801-1804 (2000).
97. Li, J. et al. Carbon Nanotube Sensor for Gas and Organic Vapor Detection. Nano Lett. 3, 929-933 (2003).
98. Joshi, K. A. et al. A Disposable Biosensor for Organophosphorus Nerve Agents Based on Carbon Nanotubes Modified Thick Film Electrode. Electroanalysis 17, 54-58 (2005).
99. Zhang, T. et al. Poly(m-Aminobenzene Sulfonic Acid) Functionalized Single-Walled Carbon Nanotubes Based Gas Sensor. Nanotechnol. 18, 165504 -6 (2007).
100. Shen, J. F., Hua, Y. Z., Li, C., Qin, C. & Ye, M. X. Pt-Co Supported on Single-Walled Carbon Nanotubes as an Anode Catalyst for Direct Methanol Fuel Cells. Electrochim. Acta 53, 7276-7280 (2008).

101. Ramesh, P., Itkis, M. E., Tang, J. M. & Haddon, R. C. SWNT-MWNT hybrid architecture for proton exchange membrane fuel cell cathodes. J. Phys. Chem. C 112, 9089-9094 (2008).
102. Tang, J. et al. in MRS Spring Meeting 2007 EE03-01 (MRS, San Francisco, 2007).
103. Liu, Z. et al. Preparation and Characterization of Platinum-Based Electrocatalysts on Multiwalled Carbon Nanotubes for Proton Exchange Membrane Fuel Cells. Langmuir 18, 4054-4060 (2002).
104. Tang, J. M. et al. Carbon Nanotube Free-Standing Membrane as Gas Diffusion Layer in Hydrogen Fuel Cells. Micro & Nano Letters 1, 62-65 (2006).
105. Tang, J. et al. Carbon Nanotube Free Standing Membrane of Pt/SWNTs as Catalysts Layer in Hydrogen Fuel Cells. Aus. J. Chem. 60, 528-532 (2007).
106. Tang, J. M. et al. High Performance Hydrogen Fuel Cells with Ultralow Pt Loading Carbon Nanotube Thin Film Catalysts. J. Phys. Chem. C 111, 17901-17904 (2007).
107. Jha, N., Palanisamy, R., Itkis, M. E. & Haddon, R. C. Construction of a Carbon-Nanotube-Based Fuel Cell Which Exceeds 2015 DOE Targets. ACS Nano submitted (2011).
108. Xie, X. et al. Graphene-Sponges as High-Performance Low-Cost Anodes for Microbial Fuel Cells. Energy & Environ. Sci. 5, 6862-6866 (2012).
109. Xie, X. et al. Nano-Structured Textiles as High-Performance Aqueous Cathodes for Microbial Fuel Cells. Energy & Environ. Sci. 4, 1293-1297 (2011).
110. Xie, X. et al. Three-Dimensional Carbon Nanotube-Textile Anode for High-Performance Microbial Fuel Cells. Nano Lett. 11, 291-296 (2011).
111. Cao, Q. et al. Highly Bendable, Transparent Thin-Film Transistors that use Carbon-Nanotube-Based Conductors and Semiconductors with Elastomeric Dielectrics. Advanced Materials 18, 304-+ (2006).
112. Zhang, D. et al. Transparent, Conductive, and Flexible Carbon Nanotube Films and Their Applications in Organic Light-Emitting Diodes. Nano Lett. 6, 1880-1886 (2006).
113. Gruner, G. Carbon Nanotube Films for Transparent and Plastic Electronics. J. Mater. Chem. 16, 3533-3539 (2006).
114. Hu, L. B., Yuan, W., Brochu, P., Gruner, G. & Pei, Q. B. Highly Stretchable, Conductive, and Transparent Nanotube Thin Films. Appl. Phys. Lett. 94 (2009).
115. Lu, F. S. et al. Metallic Single-Walled Carbon Nanotubes for Transparent Conductive Films. Chem. Phys. Lett. 497, 57-61 (2010).
116. Avouris, P., Freitag, M. & Perebeinos, V. Carbon-Nanotube Photonics and Optoelectronics. Nature Photonics 2, 341-350 (2008).

117. Freitag, M., Martin, Y., Misewich, J. A., Martel, R. & Avouris, P. Photoconductivity of Single Carbon Nanotubes. Nano Lett. 3, 1067-1071 (2003).
118. Levitsky, I. A. & Euler, W. B. Photoconductivity of Single-Wall Carbon Nanotubes Under Continuous-Wave Near-Infrared Illumination. Appl. Phys. Lett. 83, 1857-1859 (2003).
119. Freitag, M. et al. Hot Carrier Electroluminescence from a Single Carbon Nanotube. Nano Lett. 4, 1063-1066 (2004).
120. Tarasov, M., Svensson, J., Weis, J., Kuzmin, L. & Campbell, E. Carbon Nanotube Based Bolometer. JETP Lett. 84, 267-270 (2006).
121. Lee, J. U., Codella, P. J. & Pietrzykowski, M. Direct Probe of Excitonic and Continuum Transitions in the Photocurrent Spectroscopy of Individual Carbon Nanotube p-n Diodes. Appl. Phys. Lett. 90, 053103 (2007).
122. Mann, D. et al. Electrically DrivenThermal Light Emission from Individual Single-Walled Carbon Nanotubes. Nat. Nanotechnol. 2, 33-38 (2007).
123. St-Antoine, B. C., Menard, D. & Martel, R. Single-Walled Carbon Nanotube Thermopile For Broadband Light Detection. Nano Lett. 11, 609–613 (2011).

Chapter 2 Field Effect Induced Electro-Optical Modulation of Infrared Transmittance in SWNT Thin Films

2.1 Introduction

SWNT thin films possess unique optoelectronic properties due to the one dimensional structure of individual carbon nanotubes.[1, 2] They have already shown great promise in optoelectronic applications in the IR-Vis spectral range, as IR detectors,[3-9] LEDs [10-16] and opto-couplers.[17] Electro-optical phenomena are one of the fascinating, but least explored fields of CNT based photonics. Here I present a fundamental study of electro-optical effects in thin SWNT films that resulted in enhancement of the amplitude of electro-optical modulation by an order of magnitude which is much superior to previous reports.[18, 19]

An electro-optical modulator is an optoelectronic device which can be used to modulate the intensity of the optical beam via the application of an electric voltage. One specific type of electro-optical modulator is the electro-absorption modulator, in which the principle of operation is often based on the Stark and Franz–Keldysh effects: that is, changes in the shape of the spectra in the vicinity of the band edge under an applied electric field which includes excitonic features. Recently, it has been predicted theoretically that Stark and Franz–Keldysh effect are extremely strong in the case of 1D SWNT placed in external static electric field along the tube axis, especially when excitonic effects are taken into account.[20] However, the Franz-Keldysh effect in SWNTs has not yet been observed experimentally. Instead, it was found that the light transmitted

through SWNT thin film based FET can be electrically modulated by the gate voltage.[18, 19] Compared with the conventional types of electro-optical modulators, SWNT based electro-absorption modulator has the potential to operate with much lower voltages and at very high speed. The SWNT random networks are flexible at thicknesses between a monolayer and a hundred nanometers, which could make these devices extremely useful for 3D integrated optoelectronics.[21]

In the absorption spectrum of pristine carbon nanotube film, the observed S_{11}, S_{22} and M_{11} peaks are due to interband transitions between related van Hove singularities.[22] Because of the spike like DOS, slight modification of Fermi level in the DOS of the SWNTs significantly modifies the intensity of the intrinsic interband transitions in the semiconducting SWNTs (Figure 2.1). The most common method used to control Fermi level position is chemical doping,[23-27] either substitutional or interstitial. Exposure of the nanotubes to vapors of Br_2 or I_2,[28-32] which injects holes into the valence band of the carbon nanotubes, shifts their Fermi levels, resulting in a change in the Vis-IR spectrum (Figure 2.2).[31]

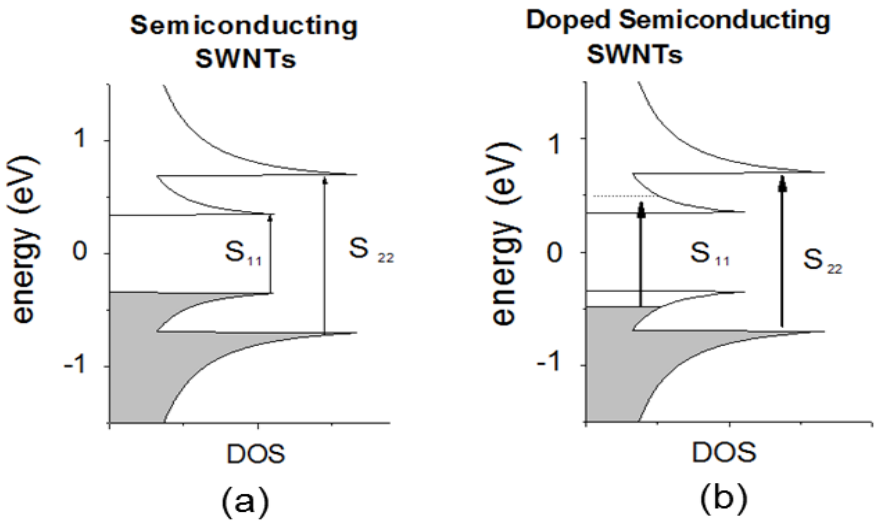

Figure 2.1: Schematic representation of the density of states (DOS) of SWNTs contributing to the near-IR and far-IR absorption. (a) Intrinsic semiconducting SWNT; S_{11} and S_{22} correspond to the first and second interband transitions in the near-IR spectral range. (b) Hole-doped semiconducting SWNT; first interband transition (S_{11} doped) is shifted to higher energy due to depletion of the conduction band.

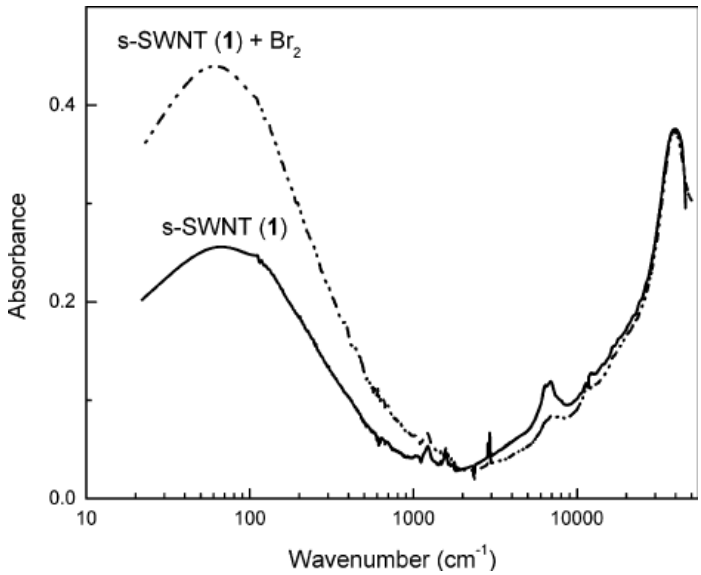

Figure 2.2: FIR-Vis-UV spectra of films of SWNT before and after exposure to bromine vapor.[33]

Chemical doping also occurs naturally during the purification process and exposure to the ambient atmosphere (Figure 2.3 (a)). The standard purification process methods that are used to remove impurities from the as-prepared SWNT material lead to p-doped purified SWNTs, and heating of the purified SWNTs in high vacuum can lead to partially desorption of the dopant and SWNTs de-doping. [22] [34, 35] Depletion of the first singularity in the DOS (Figure 2.1 (b)) results in the loss of the corresponding interband electronic transition (dashed arrow) and loss of the associated S_{11} absorption intensity, while refilling of the first singularity results in the gain of the corresponding interband transition strength and enhancement of the associated S_{11} absorption intensity. Thus, annealing of SWNT films yields the spectra in which the absorption intensities are maximized. The exposure to the ambient atmosphere can also introduce p-type dopants in SWNTs, suppressing the intensity of S_{11} absorption peaks, which can be easily observed in semiconducting SWNT films (Figure 2.3 (b)). Despite the strong effect of chemical doping, it cannot be utilized for optical modulation applications because of the slow reaction time.

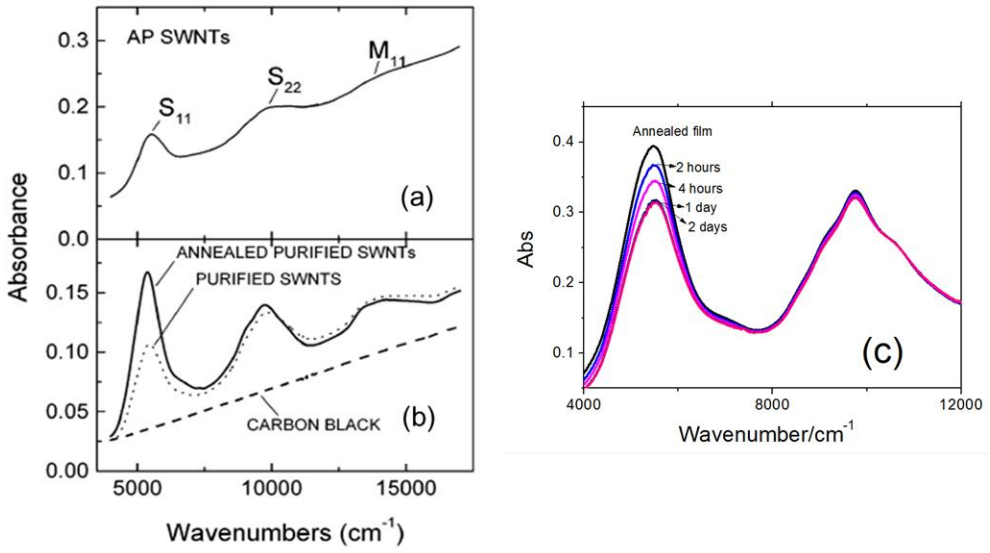

Figure 2.3: (a) Spectra of a film of as-prepared SWNTs; (b) purified L-SWNTs before (dotted line) and after (solid line) heating under vacuum at 350 °C; (c) spectra of a film as a function of the duration of the exposure to the ambient atmosphere.

As an alternative to the chemical doping, electrolyte based electro-chemical doping can be conducted by utilizing electrolyte gating in a FET[36] or electrochemical cell configuration.[37, 38] Giant electro-optical modulation of the infrared transmission in the range of the first interband transition of semiconducting SWNTs (S_{11}) was achieved (up to 50%), but the slow response time in the range of minutes limits the practical application of such electrolyte based devices.[36]

Electrical control of the SWNT absorbance was also demonstrated in solid state FET configuration.[18, 19] In these reports SWNT thin film was connected to source and drain terminals while the electrical potential between the SWNT thin

film and an isolated gate electrode was modified resulting in shifting the Fermi level of the semiconducting SWNTs and modulating the intensity of interband transitions (Figure 2.4 (a)); such devices show much faster electro-optical response but the amplitude of electro-optical modulation was very low (0.2-0.5%) (Figure 2.4 (b)).[18, 19]

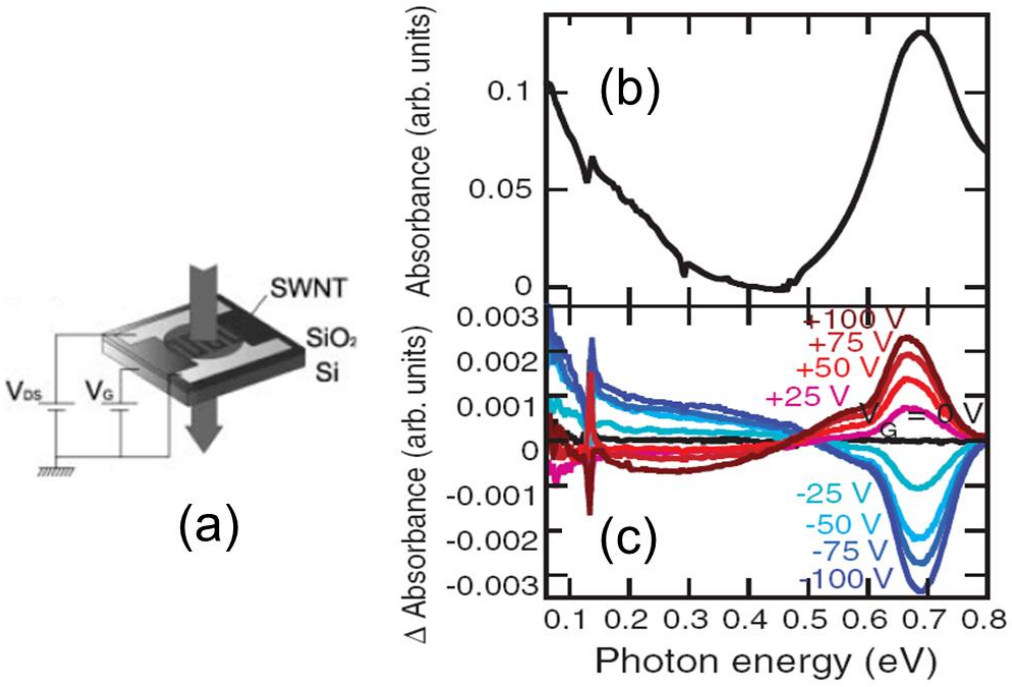

Figure 2.4: (a) Schematic of SWNT thin file FET structure used in ref.[18, 19]; (b) IR absorption spectrum of SWNT-FET. (c) Difference spectra of absorbance, before and after gate bias (V_G) application. Data sets are displayed for every 25V from V_G =-100 to 100 V.

In our study, we set out to enhance the solid state electro-optical effect by conducting a comprehensive fundamental study of the major factors influencing the amplitude of the electro-optical modulation in SWNTs. As a result, we

demonstrated that the utilization of separated semiconducting SWNTs of large diameter leads to an order of magnitude enhancement of the electro-optical modulation (ΔT) of infrared transmittance T, with a frequency bandwidth exceeding 100 kHz.

2.2 Experimental

2.2.1 Fabrication of SWNT thin film electro-absorption modulator

All SWNT films in this work were prepared from dispersions in water or dimethylformamide (DMF) by vacuum filtration using an alumina membrane disk (47 mm dia, 0.02 μm pore size, and 34 mm working dia.). To determine the film thickness of the SWNT thin film, we prepared a thicker film (>100 nm) and measured it by using a Dektak profilometer. The thickness of the SWNT thin films was controlled by the amount of the SWNT material utilized for the vacuum filtration taking into account the working area of the filtration membrane. SWNT film were patterned with the desired shape and size (narrow ribbon of width 0.5mm and length 3-4mm in this experiment) on the membrane by using a precision knife with a titanium alloy blade. The alumina membrane is dissolved in a 0.05N NaOH aqueous solution, leaving fragments of nanotube film with the desired shape floating in solution. The NaOH residue is cleaned by transferring the nanotube films to DI water several times with glass pipette followed by transferring the film to the substrate with pre-patterned electrodes to fabricate the electro-optical device.(Figure 2.5)

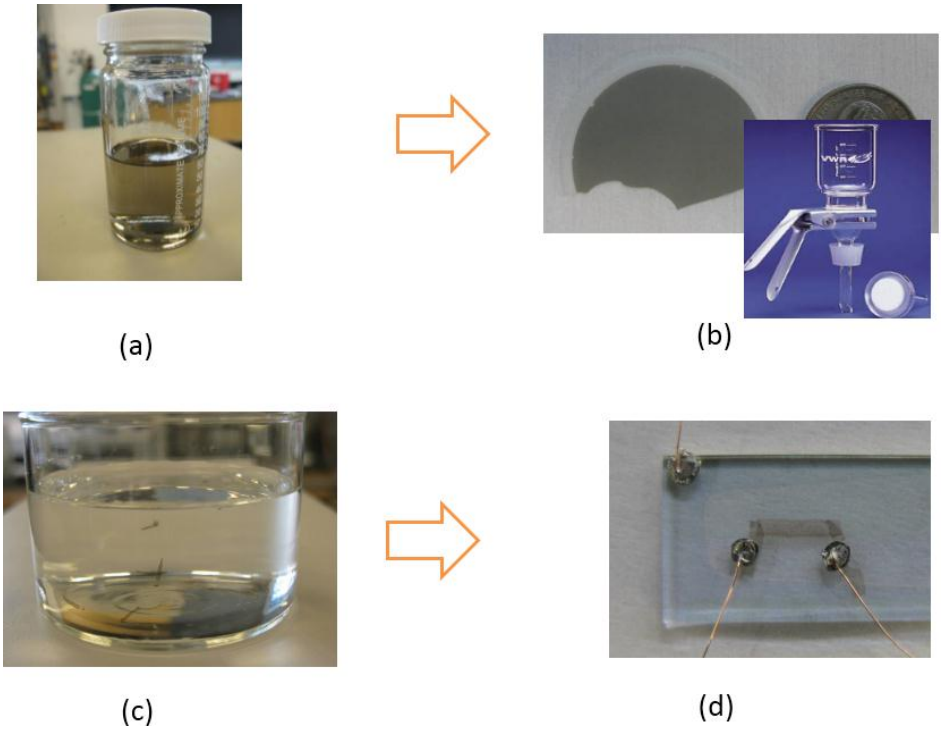

Figure 2.5: Vacuum filtration steps: (a) preparation of dilute suspension of purified nanotubes; (b) vacuum-filtration of a dilute suspension of purified nanotubes on the filtration membrane; (c) dissolved membrane leaves SWNT thin film floating in solvent (water); (d) SWNT films transferred to substrate, forming SWNT thin film based device.

High quality ITO coated glass substrates are chosen as the bottom gate electrode. In order to optimize the device yield and performance, we tested several gate dielectric materials at a variety of thicknesses, including parylene (optimum thickness ~800 nm), silicon dioxide, and silicon nitride (optimum thickness~120 nm), but we found that hafnium oxide (optimum thickness ~80-90 nm) provided the best performance. HfO_2 is high-k gate dielectric and HfO_2 deposited by atomic layer deposition (ALD) is stable against breakdown for gate voltages up to 20-30 V under ambient conditions.

In this study, many kinds of SWNT materials were tested; the majority of films used in this study were prepared from a dispersion of 0.040 mg of SWNT material in 100 mL of solvent with a resulting thickness *t*= 35 nm corresponding to a density of 1.2 g/cm^3 for all types of SWNT films. The SWNT film in the form of a narrow ribbon of width 0.5mm and length 3-4mm was transferred onto the hafnium oxide layer. The active area of the individual devices corresponds to the region of overlap between the ITO, HfO_2 and SWNT layers which was typically 0.5 × 0.5 mm^2.

Each substrate consisted of 4-5 devices which were prepared to allow the comparison of different types of SWNTs; 5-10 devices were measured for each type of SWNTs. Indium pads were used to connect the SWNT devices to the external circuit. (Figure 2.6)

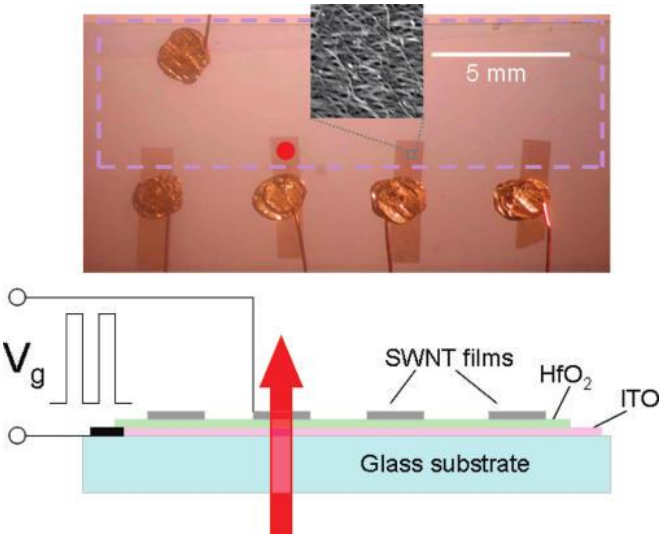

Figure 2.6: Optical micrograph of the experimental setup for study of the electro-optical gating effect in SWNT thin films. The square-wave modulation is applied between ITO gate electrode and semitransparent SWNT thin film while infrared transmission is monitored.

2.2.2 Spectroscopic setup for characterization of SWNT optoelectronics

In order to characterize the optoelectronic properties of SWNT thin films, we developed a multifunctional spectroscopic setup in which high resolution Vis-IR-mid-IR Horiba Yobin-Robin ihr 320 monochromator was coupled to the input of a Bruker HYPERION 1000 infrared microscope (Figure 2.7 (a)). Infrared or visible monochromatic radiation from the spectrophotometer enters the IR microscope and is focused so that the IR beam gives rise to an aperture-controlled rectangular spot of characteristic size ~100 -10 μm at the SWNT film surface. The microscope is operated in transmission mode and the intensity of the light transmitted through the SWNT thin film electro-optical modulator is measured by Si and mercury cadmium telluride (MCT) photodetectors with the

output detector signal processed by a lock-in amplifier as a function of wavelength of radiation (absorption spectrum) and electric field applied to the SWNT film (Figure 2.7 (b)). For IR transmission spectroscopy, the monochromatic radiation was chopped at 105 Hz; spectra of the electro-modulated transmitted light were taken without chopping the light, but with the gate voltage modulated at frequency of 230 Hz. The measurements were conducted under ambient environment.

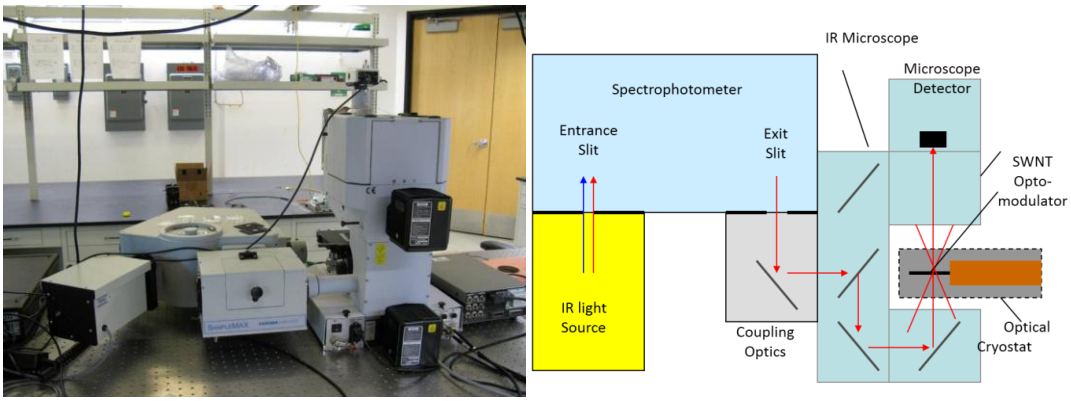

(a) (b)

Figure 2.7: (a) Multifunctional spectroscopic setup: Vis-IR-mid-IR Horiba Yobin-Robin ihr 320 monochromator coupled to a Bruker HYPERION 1000 infrared microscope. (b) Schematic of the station.

2.3 Results and discussion:

2.3.1 Observation of electro-optical modulation

Figure 2.8 (a), 2.8 (b) present spectra of absorbance (Abs) and electro-modulated transmittance $\Delta T/T$ of 35 nm thick EA-SWNT film for gate voltages of negative (blue curve) and positive (red curve) polarity. The spectrum of the SWNT film was essentially identical to that which I discussed in Chapter 1.[22] The EA-SWNT films consist of a mixture of semiconducting and metallic nanotubes of different diameters. The peaks at approximately 0.67 eV and 1.22 eV correspond to the first and second interband transitions (S_{11} and S_{22}) in semiconducting nanotubes, and the peak at 1.71 eV corresponds to the first interband transition (M_{11}) in metallic nanotubes. The electro-optical modulation signal $\Delta T/T$ is concentrated in the vicinity of the S_{11} transition; the electro-optical modulation signal in the vicinity of the S_{22} transition is visible but much weaker compared to the effect at S_{11}. There is no observable electro-optical modulation signal in the vicinity of the M_{11} transition. At positive gate potential the sign of electro-optical modulation $\Delta T/T$ is negative (transmission decreases), while at negative gate potential the sign of electro-optical modulation $\Delta T/T$ is positive (transmission increases). The observed effect is in accord with the electrical control of the Fermi level by the gate potential; the applied negative (positive) gate potential induces depletion (refilling) of the first semiconducting van Hove singularity in the valence band thus decreasing (increasing) the number of the effective states participating in the S_{11} optical transition(Figure 2.8 (c)). The observed changes

correspond to a p-type doped SWNT film; in the case of n-doping the sign of the effect is expected to be reversed; and in the case of exact intrinsic state, the transmittance is expected to increase for both polarities of the gate voltage.

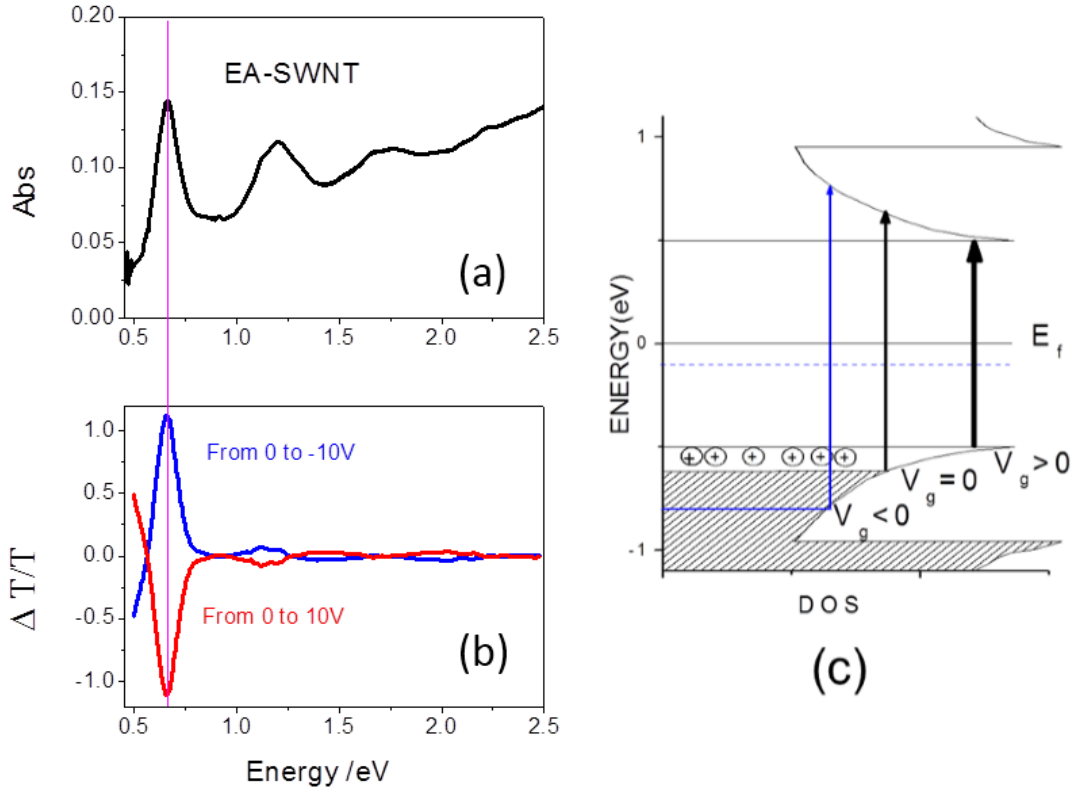

Figure 2.8: (a) spectrum of absorbance (Abs) and (b) electro- modulated transmittance Δ*T*/*T* of 35 nm thick EA-SWNT film for gate voltages of +10V and -10V. (c) Schematic representation of the density of states (DOS) change of p-doped SWNT films controlled by gate voltage contributing to the near-IR and far-IR absorption.

2.3.2 Diameter dependence of the field effect induced electro-optical modulation of infrared transmittance

First, we studied the effect of SWNT diameter on the electro-optical phenomena in SWNT thin films. Four types of SWNT with different diameters were utilized: CoMoCAT SG65 SWNTs, purchased from SouthWest Nanotechnologies, Inc. of average diameter, D_{av} = 0.8 $\pm$0.1 nm; HiPCO SWNTs, purchased from Carbon Nanotechnologies, Inc. (CNI), D_{av} = 1.0 $\pm$ 0.1 nm; SWNTs produced by laser ablation, purchased from CNI, L-SWNTs, D_{av}=1.3 $\pm$0.1 nm, and electric arc produced (purified) SWNTs synthesized in our group, EA-SWNTs, D_{av} =1.55 $\pm$ 0.1 nm. All films are prepared from a dispersion of 0.040 mg of SWNT material in 100 mL of solvent with a resulting thickness t = 35 nm.

Figure 2.9 (a) and 2.9 (b) presents spectral measurement of absorbance (Abs) and electro-modulated transmittance $\Delta T/T$ of four types of SWNTs for negative gate voltage V=-10V. From the spectra, we can see that S_{11} bands for SG65-SWNTs, HiPCO-SWNTs, L-SWNTs, and EA-SWNTs are centered at 1.21, 0.95, 0.78, and 0.66 eV, respectively, in accordance with the increasing SWNT diameter from 0.8 to 1.55nm, which again verifies the relationship that the band gap of semiconducting SWNTs decreases with increasing diameter as 1/d [39, 40].

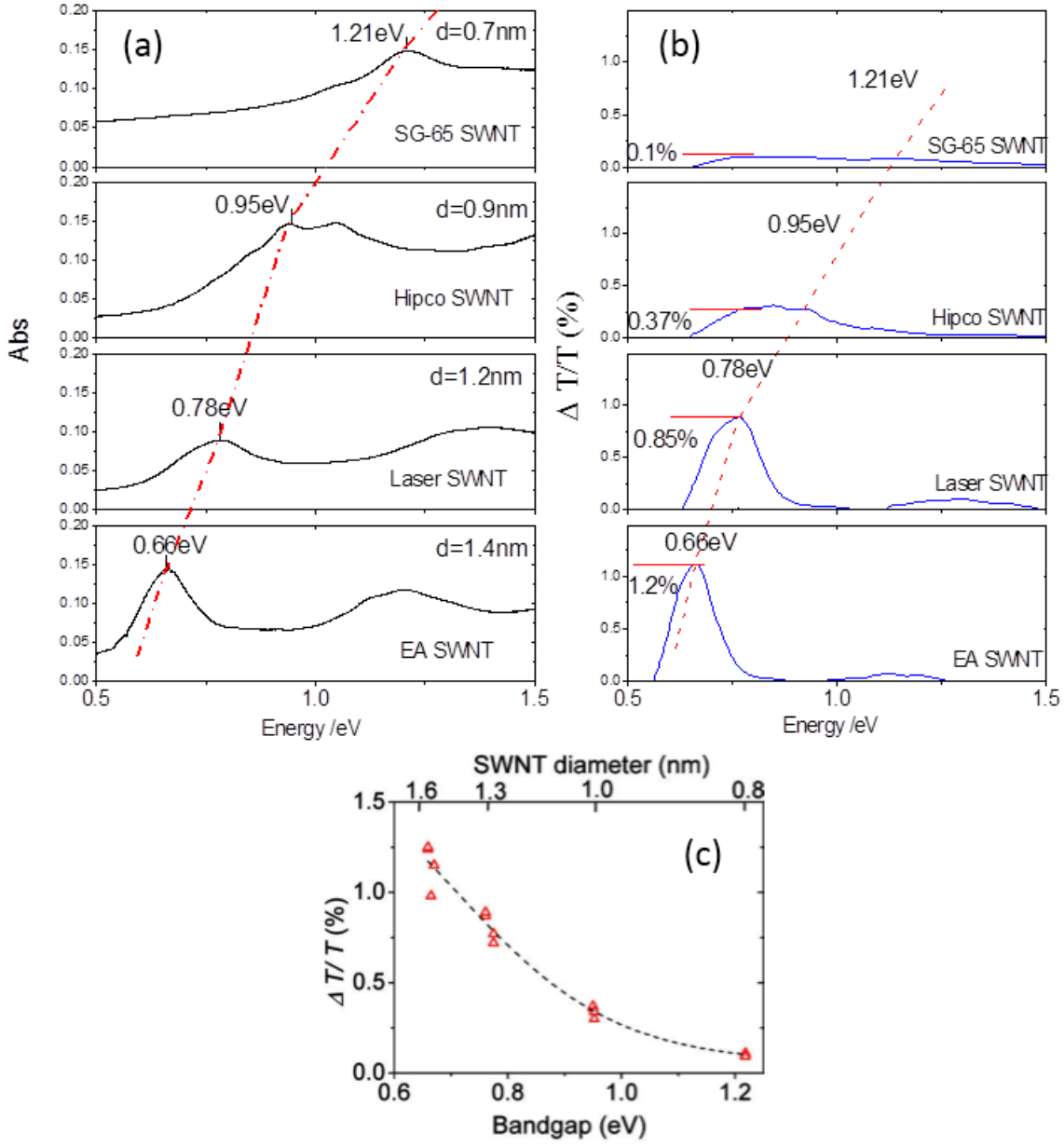

Figure 2.9: (a) Spectra of absorbance (Abs) and (b) electro-modulated transmittance Δ*T*/*T* of 35 nm thick films of four types of SWNTs for gate voltages of -10V: SG65 SWNTs; HiPCO SWNTs; laser ablation produced L-SWNTs; electric arc produced EA-SWNTs. (c) Amplitude of electro-optical modulation, Δ*T*/*T* at the peak of the S_{11} absorption band as a function of the SWNT bandgap and average diameter.

As can be seen in Figure 2.9 (b), the electro-modulated response increases with increasing SWNT diameter and decreasing band gap, as summarized in Figure 2.9 (c). This dependence is naturally related to the energy separation between the chemical potential E_f (Fermi level), and the energy of the valence band E_V; in the larger diameter SWNTs the energy separation is the smallest and the band filling is more sensitive to the shift of the chemical potential induced by the gate voltage.

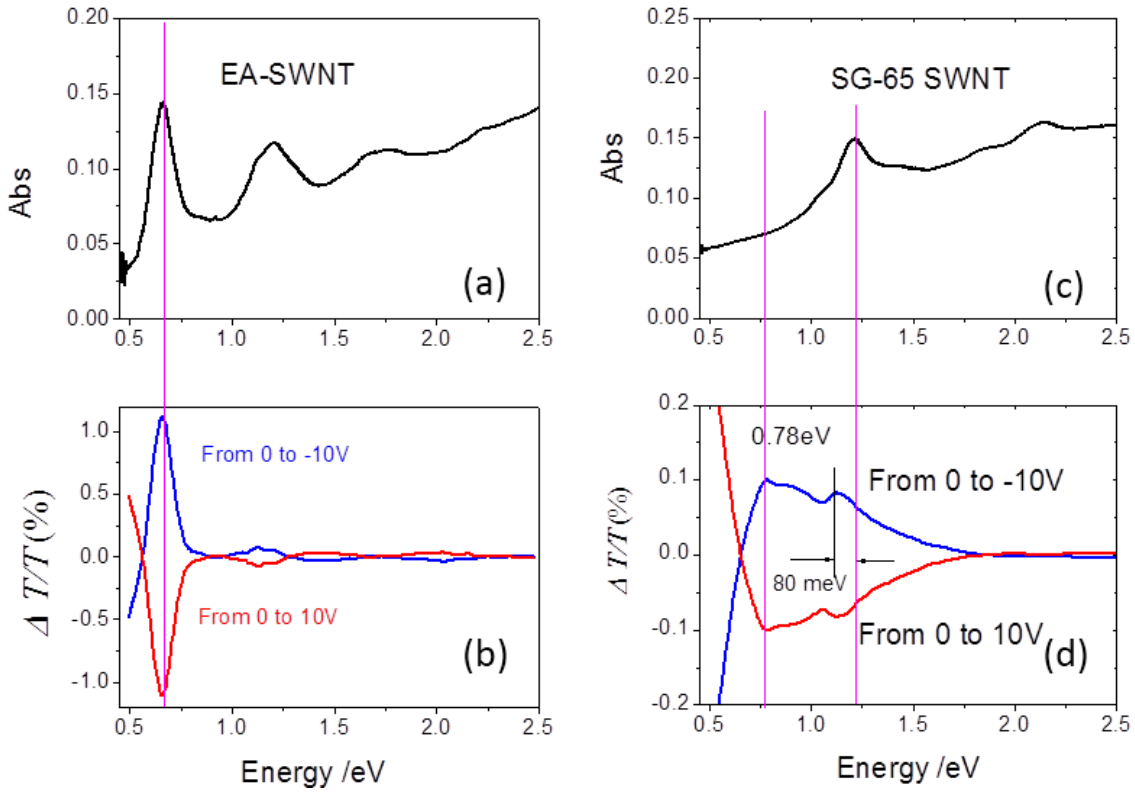

Figure 2.10: (a) Spectra of absorbance (Abs) and (b) electro-modulated transmittance Δ*T*/*T* of 35 nm thick EA-SWNTs for gate voltages. (c) Spectra of absorbance (Abs) and (d) electro-modulated transmittance Δ*T*/*T* of 35 nm thick SG65 SWNTs for gate voltages.

For large diameter SWNTs, the position of absorption and electro-optical modulation spectra are practically coincident. In contrast, for small diameters SG65-SWNTs (Figure 2.10) we observed notable red shift of the spectral maximum of the electro-optical modulation $\Delta T/T$ with respect to the maximum of the absorbance spectra. Moreover, an extended tail in the electro-optical modulation $\Delta T/T$ with maximum at 0.78 eV is observed. This red shift can be explained on the basis of Figure 2.9 (c) which indicates that the contribution to the electro-optical modulation of the low energy (larger diameter) tail of the SWNT diameter distribution within each type of SWNTs is enhanced. It is likely that a small fraction of large diameter SWNTs ($d \approx 1.3$ nm, E_g=0.78eV) with absorption features hidden in the low energy tail of the spectrum produces a contribution to the electro-optical spectrum comparable to the contribution of the dominant population fraction of SG65-SWNTs suppressed due to strong diameter dependence of the electro-optical effect.

2.3.3 Effect of ratio of semiconducting and metallic SWNTs on the field effect induced electro-optical modulation of infrared transmittance

Bulk SWNTs materials consist of a mixture of semiconducting and metallic SWNTs, most frequently at the 2:1 statistical ratio. Only the semiconducting SWNTs are expected to contribute to the electro-optical signal induced by the gate potential, so the enrichment of the sample with semiconducting SWNTs should further enhance the amplitude of the electro-optical signal. To investigate

the effect of semiconducting SWNT content on the amplitude of the electro-optical modulation, we utilized four different samples of EA-SWNTs purchased from NanoIntegris Inc.[41] with varying ratios of semiconducting to metal metallic (S/M) SWNTs: IsoNanotubes-M(70%), S/M (%) ~30:70; PureTubes, S/M ~67:33; IsoNanotubes-S (95%), S/M ~95:5 and IsoNanotubes-S (99%), S/M ~99:1. All films were of the same thickness t = 35 nm.

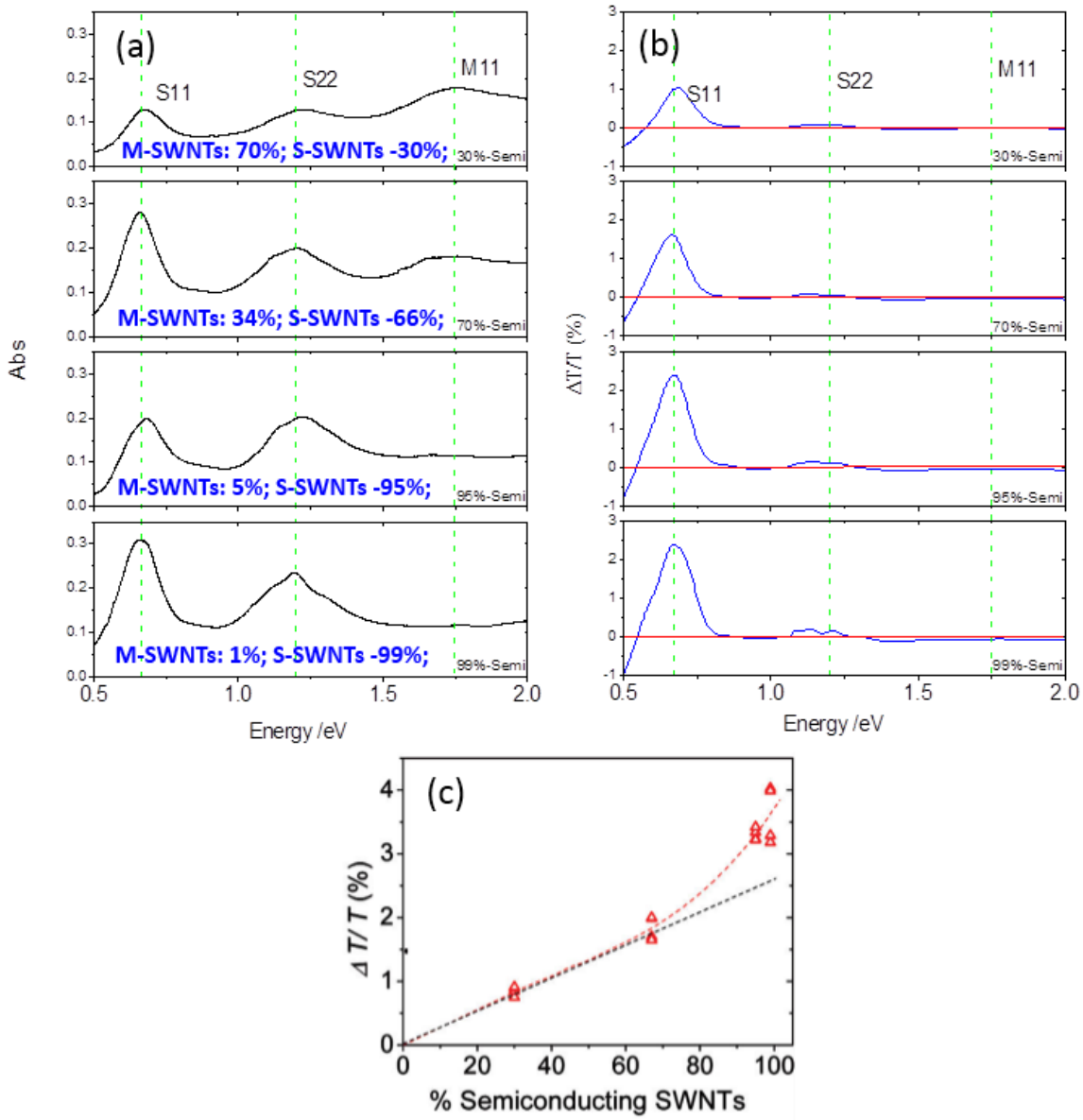

Figure 2.11: (a)Spectra of absorbance (Abs) and (b) electro-modulated transmittance Δ*T*/*T* of 35 nm thick films of SWNT samples with different ratios of concentrations of semiconducting to metallic SWNTs (S/M). (c) Peak amplitude of the electro-optical modulation Δ*T*/*T* in SWNT films as a function of the semiconducting SWNT content.

Figure 2.11 (a) and 2.11(b) present spectral measurements of absorbance and electro-optical modulated transmittance $\Delta T/T$ of SWNT films prepared from SWNT fractions containing different S:M ratios. Absorption spectra for S/M = 30:70 SWNTs shows a prominent M_{11} absorption band in accordance with the enrichment in metallic SWNTs. With decreasing metallic and increasing semiconducting fraction, the S_{11} and S_{22} optical features are enhanced at the expense of the M_{11} feature. In the absorption spectrum of S/M=99:1 SWNTs, there is no observable M_{11} absorption peak. It is obvious that the electro-optical modulation signal grows as the S:M ratio increases from 30:70 to 99:1 (Figure 2.11 (b)). The dependence of the electro-optical modulation on the ratio of semiconducting to metallic SWNTs is summarized in Figure 2.11(c). It can be noticed, that with increasing content of semiconducting SWNTs above 70% the amplitude of electro-optical modulation increases super-linearly. The linear component of increase of the electro-optical modulated signal can be explained by the increasing concentration of s-SWNTs contributing to the effect; the non-linear component of increase can be attributed to the additional effect of the removal of metallic SWNTs which are sources of free carriers that screen the gate potential thus suppressing the FET performance.

SWNT films are always heavily p-doped as a result of SWNT processing, film preparation, and exposure to the ambient atmosphere. We attempted to restore the intrinsic nature of semiconducting SWNT films by removing the dopants utilizing annealing of SWNT films in vacuum at 350 °C for duration of 2

to 5 hours. The annealing substantially enhanced the S_{11} band, but the amplitude of electro-optical modulation did not notably change in any of the samples. We also notice that sign of the response is unchanged which means that the SWNT films remain in a partially p-doped state even after annealing. If the semiconducting SWNTs film is in exact intrinsic state, the transmittance is expected to increase for both polarities of the gate voltage.

2.3.4 Dependence of the field effect induced electro-optical modulation of infrared transmittance on the thickness of SWNT films

An annealed SWNT film composed of 99% separated semiconducting SWNTs still possesses significant conductance associated with free carriers. As a result, the gate voltage affects efficiently only thin layer of the film adjacent to the gate dielectric, while the rest of layers are screened from the effect of the gate voltage. It is intuitively understandable that the gate voltage should be more efficient for thinner films. But from the application standpoint, if the film is too thin, there will not be enough optical depth to modulate strongly the transmitted signal. In order to enhance the electro-optical modulation, we have to find the thickness of SWNT film at which the electro-optical modulated signal reaches a maximum. In this study, we utilized SWNT materials IsoNanotubes-S (99%), and nanotube films with different thickness from 120 to 6 nm were fabricated.

The amplitudes of electro-modulated signals $\Delta T/T$ are presented in Figure 2.12, respectively. The electro-optical modulated signal reaches a maximum around a thickness of 15 nm (~10 SWNT layers) with a slight decrease in the thinnest films (6 nm) and a decrease by a factor of two for thicker films (t ~100 nm).

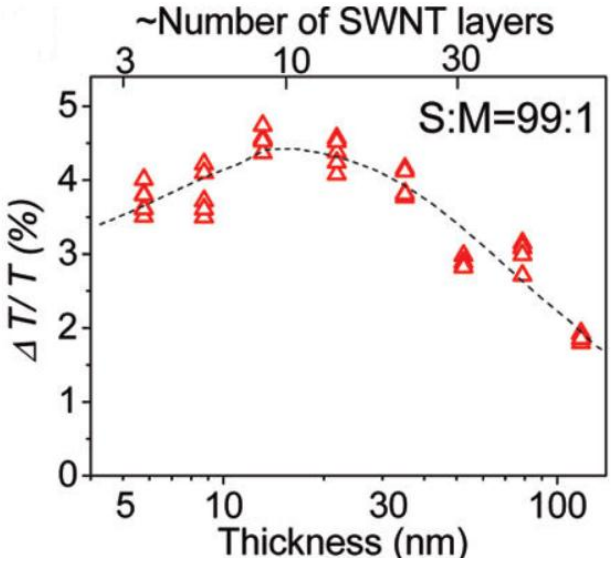

Figure 2.12: Amplitude of the electro-modulated transmittance $\Delta T/T$ as a function of semiconducting SWNT film thickness.

Because of the relationship between the transmittance (T) and the absorption coefficient (α), $T=\exp(-\alpha t)$, where t is the film thickness, the change in transmittance (ΔT) is related to the change of the absorption coefficient, $\Delta \alpha$. Neglecting reflection, we can represent the transmittance of a SWNT film modulated with an electric field E as, $T + \Delta T(E) \approx \exp[-(\alpha + \Delta \alpha (E))t]$. In the regime where $\Delta \alpha t \ll 1$, this leads to the relationship $\Delta T/T \approx -\Delta \alpha t$, in which $\Delta \alpha t$

is directly proportional to the total charge accumulated at a given gate voltage. The spatial distribution of the accumulated charge across the thickness of the SWNT film can be evaluated by studying the modification of absorption coefficient $\Delta\alpha$ as a function of SWNT film thickness. A strong dependence on the film thickness is observed for $\Delta\alpha$ normalized to the film thickness as shown in Figure 2.13, with $\Delta\alpha$ increasing by 40 times as the film thickness decreases from 120 to 6 nm. This indicates that most of the charge is accumulated in the layers (1-5) adjacent to the gate dielectric interface; the presence of the additional layers results in a decrease of the response due to the screening of the gate potential by the carriers supplied by the outer layers.

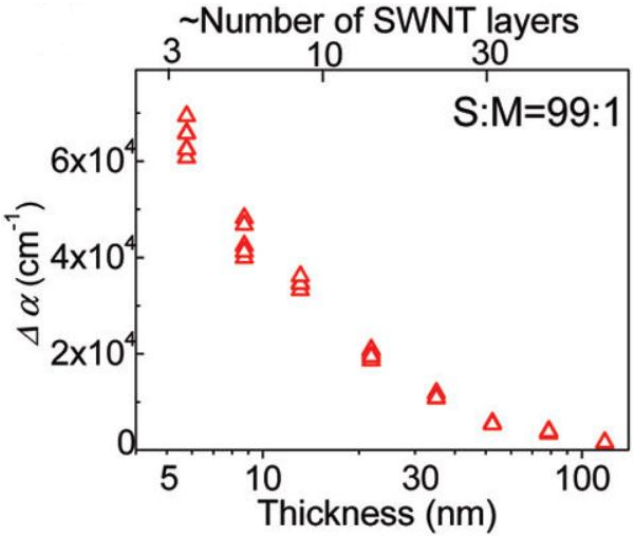

Figure 2.13: Amplitude of the electro-modulated absorption coefficient $\Delta\alpha$ as a function of semiconducting SWNT film thickness.

2.3.5 Frequency dependence of the field effect induced electro-modulation of infrared transmittance

We measured the electro-modulated transmittance as a function of frequency of the gate voltage modulation in the range 1 Hz to 100 kHz. We found that that the bandwidth of the response exceeds 100 kHz (Figure 2.14), which is the upper limit of the lock in amplifier in our current experimental setup. The observed ~8% drop of the signal at 100 kHz is not intrinsic to the SWNT device but originates from the external circuit. Recently 80 GHz FETs were reported utilizing S:M = 99:1 SWNT thin films, [42] and we believe the operational bandwidth of the gate induced electro-optical modulation can be extended to GHz range.

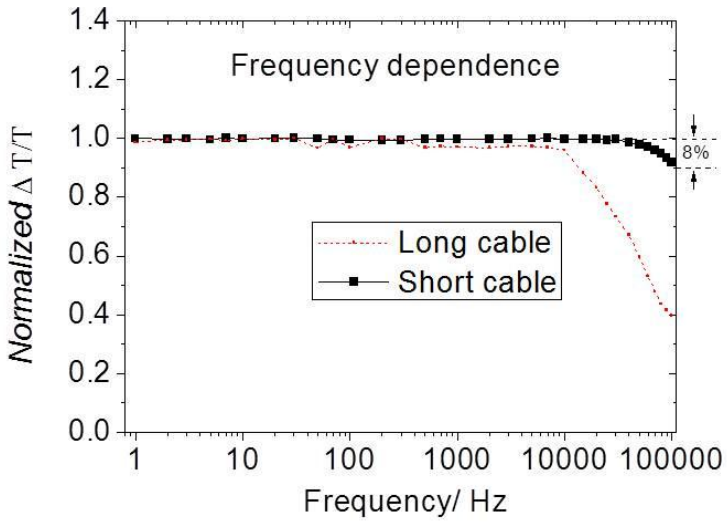

Figure 2.14: Frequency dependence of the electro-modulated transmittance Δ*T*/*T* normalized to the 1 kHz value.

2.4 Summary

In summary, we present a comprehensive study of the electro-optical effect in solid state SWNT thin film devices as a function of SWNT diameter, the ratio of semiconducting to metallic SWNTs, and SWNT thin film thickness. By using optimized transparent bottom gate electrodes, large diameter SWNTs, increasing the ratio of semiconducting to metal SWNTs, and by decreasing the SWNT film thickness, the electro-optical modulation (ΔT) of infrared transmittance T can be significantly enhanced. In very thin films $t \cong 6.5$ nm the relative change of absorption coefficient $\Delta\alpha/\alpha$ at the S_{11} interband transition reaches 70%(Figure 2.15 (a)), and electro-optical modulation (ΔT) of infrared transmittance T can be enhanced to the level of $\Delta T/T \sim 7\%$ (Figure 2.15 (b)) in 35nm thick SWNT films, which is more than an order of magnitude larger than in previous SWNT thin film solid state devices.

The bandwidth of the SWNT thin film electro-optical modulator exceeds 100 kHz with potential bandwidth of the signal extending to GHz range. The resulting solid state SWNT thin film electro-optical modulator possesses a number of attractive features such as infrared range of operation, high transparency, fast response time, low operating voltage, and nanometer scale thickness and is potentially useful in the development of 3D-integrated arrays with optoelectronic mode of interlayer communication.

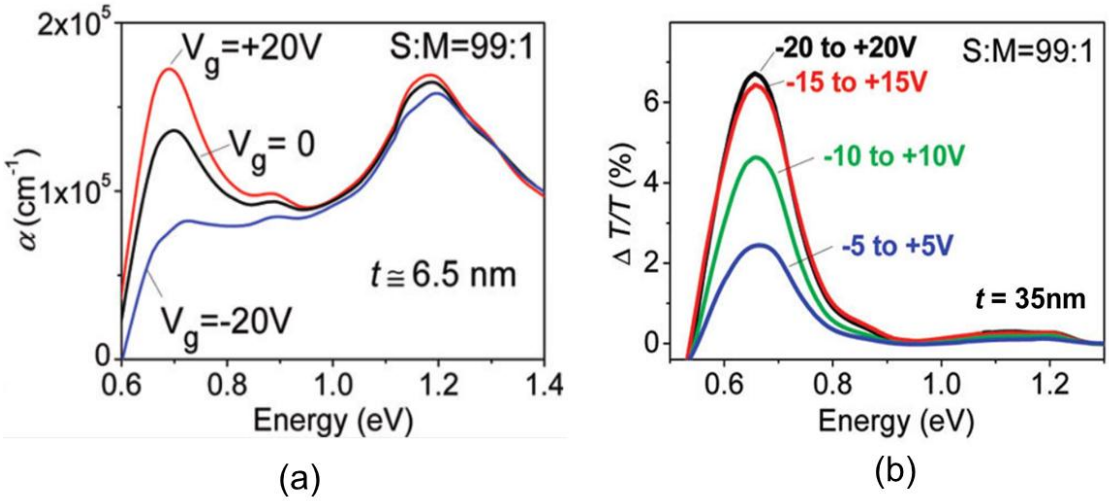

Figure 2.15: (a) Absorption spectra of 6.5nm thick semiconducting SWNT films of under DC gate voltage. (b) Spectra of the electro-modulated transmittance Δ*T*/*T* of semiconducting SWNT film at several amplitudes of bipolar gate voltage modulation indicated next to the spectral curve.

References:

1. Dresselhaus, M. S., Dresselhaus, G. & Jorio, A. Carbon Nanotubes: Advanced Topics in the Synthesis, Structure, Properties and Applications (Springler-Verlag New York, 2008).
2. Avouris, P., Freitag, M. & Perebeinos, V. Carbon-Nanotube Photonics and Optoelectronics. Nature Photonics 2, 341-350 (2008).
3. Freitag, M., Martin, Y., Misewich, J. A., Martel, R. & Avouris, P. Photoconductivity of Single Carbon Nanotubes. Nano Lett. 3, 1067-1071 (2003).
4. Qiu, X., Freitag, M., Perebeinos, V. & Avouris, P. Photoconductivity Spectra of Single-Carbon Nanotubes: Implications on the Nature of Their Excited States. Nano Lett. 5, 749-752 (2005).
5. Itkis, M. E., Borondics, F., Yu, A. & Haddon, R. C. Bolometric Infrared Photoresponse of Suspended Single-Walled Carbon Nanotube Films. Science 312, 413-416 (2006).
6. Tarasov, M., Svensson, J., Weis, J., Kuzmin, L. & Campbell, E. Carbon Nanotube Based Bolometer. JETP Lett. 84, 267-270 (2006).
7. Lee, J. U., Codella, P. J. & Pietrzykowski, M. Direct Probe of Excitonic and Continuum Transitions in the Photocurrent Spectroscopy of Individual Carbon Nanotube p-n Diodes. Appl. Phys. Lett. 90, 053103 (2007).
8. Pradhan, B., Setyowati, K., Liu, H., Waldeck, D. & Chen, J. Carbon Nanotube-Polymer Nanocomposite Infrared Sensor. Nano Lett. 8, 1142-1146 (2008).
9. Arnold, M. S. et al. Broad Spectral Response Using Carbon Nanotube/Organic Semiconductor/C60 Photodetectors. Nano Lett. 9, 3354-3358 (2009).
10. Li, P. et al. Polarized Incandescent Light Emission from Carbon Nanotubes. Appl. Phys. Lett. 82, 1763-1765 (2003).
11. Wei, J., Zhu, H. & Wu, D. Carbon Nanotube Filaments in Houshold Light Bulbs. Appl. Phys. Lett. 84, 4869-4871 (2004).
12. Freitag, M. et al. Hot Carrier Electroluminescence from a Single Carbon Nanotube. Nano Lett. 4, 1063-1066 (2004).
13. Chen, J. et al. Bright Infrared Emission from Electrically Induced Excitons in Carbon Nanotubes. Science 310, 1171-1174 (2005).
14. Mann, D. et al. Electrically DrivenThermal Light Emission from Individual Single-Walled Carbon Nanotubes. Nat. Nanotechnol. 2, 33-38 (2007).
15. Adam, E. et al. Electroluminescence from Single-Wall Carbon Nanotube Network Transistors. Nano Lett. 8, 2351-2355 (2008).
16. Engel, M. et al. Thin Film Nanotube Transistors Based on Self-Assembled, Aligned, Semiconducting Carbon Nanotube Arrays Acs Nano 2, 2445-2452 (2008).

17. Itkis, M. E., Yu, A. & Haddon, R. C. Single-Walled Carbon Nanotube Thin Film Emitter-Detector Integrated Optoelectronic Device. Nano Lett. 8, 2224-2228 (2008).
18. Takenobu, T., Murayama, Y., Shiraishi, M. & Iwasa, Y. Optical Observation of Carrier Accumulation in Single-Walled Carbon Nanotube Transistors. Jpn. J. Appl. Phys. 45, L1190-L1192 (2006).
19. Takenobu, T., Murayama, Y. & Iwasa, Y. Optical Evidence of Stark Effect in Single-Walled Carbon Nanotube Transistors. Appl. Phys. Lett. 89, 263510 (2006).
20. Perebeinos, V. & Avouris, P. Exciton Ionization, Frank-Keldysh, and Stark Effects in Carbon Nanotubes. Nano Lett. 7, 609-613 (2007).
21. Wang, F., Itkis, M. E. & Haddon, R. C. Enhanced Electromodulation of Infrared Transmittance in Semitransparent Films of Large Diameter Semiconducting Single-Walled Carbon Nanotubes. Nano Lett. 10, 937-942 (2010).
22. Itkis, M. E. et al. Spectroscopic Study of the Fermi Level Electronic Structure of Single Walled Carbon Nanotubes. Nano Lett. 2, 155-159 (2002).
23. Zhou, D., Kong, J., Yenilmez, E. & Dai, H. Modulated Chemical Doping of Individual Carbon Nanotubes. Science 290, 1552-1555 (2000).
24. Bockrath, M. et al. Chemical Doping of Individual Semiconducting Carbon Nanotube Ropes. Phys. Rev. B 61, R10 606-R10 608 (2000).
25. Hasiotis, C. et al. Development and characterization of acid-doped polybenzimidazole/sulfonated polysulfone blend polymer electrolytes for fuel cells. Journal of the Electrochemical Society 148, A513-a519 (2001).
26. Kazaoui, S., Minani, N., Kataura, H. & Achiba, Y. Absorption Spectroscopy of Single-Wall carbon nanotubes: effects of chemical and electrochemical doping. Synth. Met 121, 1201-1202 (2001).
27. Fischer, J. E. Chemical Doping of Single Wall Carbon Nanotubes. Acc. Chem. Res. ASAP (2002).
28. Lee, R. S., Kim, H. J., Fischer, J. E., Thess, A. & Smalley, R. E. Conductivity Enhancement in Single-Walled Carbon Nanotube Bundles Doped with K and Br. Nature 388, 255-257 (1997).
29. Rao, A. M., Eklund, P. C., Bandow, S., Thess, A. & Smalley, R. E. Evidence for Charge Transfer in Doped Carbon Nanotube Bundles from Raman Scattering. Nature 388, 257-259 (1997).
30. Chen, Y. et al. Chemical Attachment of Organic Functional Groups to Single-Walled Carbon Nanotube Material. J. Mater. Res. 13, 2423-2431 (1998).
31. Chen, J. et al. Solution Properties of Single-Walled Carbon Nanotubes. Science 282, 95-98 (1998).
32. Niyogi, S. et al. Chemistry of Single-Walled Carbon Nanotubes. Acc. Chem. Res. 35, 1105-1113 (2002).

33. Hu, H. et al. Sidewall Functionalization of Single-Walled Carbon Nanotubes by Addition of Dichlorocarbene. J. Am. Chem. Soc. 125, 14893-14900 (2003).
34. Niyogi, S., Kang, C. B., Perea, D., Itkis, M. E. & Haddon, R. C. Purification of Single-Walled Carbon Nanotubes. Chem. Phys. Lett. In Press (2003).
35. Itkis, M. E. et al. Purity Evaluation of As-Prepared Single-Walled Carbon Nanotube Soot by Use of Solution Phase Near-IR Spectroscopy. Nano Lett. 3, 309-314 (2003).
36. Wu, Z. et al. Transparent, Conductive Carbon Nanotube Films. Science 305, 1273-1276 (2004).
37. Kavan, L. et al. Electrochemical Tuning of Electronic Structure of Single-Walled Carbon Nanotubes: In-Situ Raman and vis-NIR Studies. J. Phys. Chem. B 105, 10764-10771 (2001).
38. Zukalova, M., Tarabek, J., Kalbac, M., Kavan, L. & Dunsch, L. In Situ Optical Spectroelectrochemistry of Single-Walled Carbon Nanotube Thin Films. J Solid State Electrochem. 12, 1279-1284 (2008).
39. Saito, R., Fujita, M., Dresselhaus, G. & Dresselhaus, M. S. Electronic Structure of Graphene Tubules based on C60. Phys. Rev. B 46, 1804-1811 (1992).
40. Kataura, H. et al. Optical Properties of Single-Wall Carbon Nanotubes. Synth. Met. 103, 2555-2558 (1999).
41. Arnold, M. S., Green, A. A., Hulvat, J. F., Stupp, S. I. & Hersam, M. C. Sorting carbon nanotubes by electronic structure using density differentiation. Nature Nanotechnology 1, 60-65 (2006).
42. Nougaret, L. et al. 80 GHz Field-Effect Transistors Produced Using High Purity Semiconducting Single-Walled Carbon Nanotubes. Appl. Phys. Lett. 94, 243505 (2009).

Chapter 3 Ionic Liquid Based Absorption Modulation in SWNT Film

3.1 Introduction

Single-walled carbon nanotubes (SWNTs) possess unique optoelectronic properties due to their one-dimensional electronic structure.[1-3] A number of photonic applications have been proposed based on the observation of photodetection and light emission from SWNTs; [3-12] in addition, SWNT thin films have been explored as transparent conducting coatings in large area solar cells and displays.[13-17] Electro-optical phenomena provide another fascinating but less explored field of SWNT photonics in which most reports relate to the modulation of the interband and excitonic transitions in SWNT thin film field-effect transistors (FET) which utilize electrolytic cells and solid state gates,[13, 18-20], while the search for the theoretically predicted enhancement of Frank-Keldysh and Stark effects[3, 21] is still in progress.

In chapter 2, I introduced a study of the electro-optical modulation based on solid state SWNT thin film FET.[20] By using optimized transparent bottom gate electrode and semiconducting SWNTs of larger diameter, the electromodulation (ΔT) of infrared transmittance T was significantly enhanced with a bandwidth exceeding 100 kHz. The 7% transmittance modulation which was achieved is still below the requirements for practical applications. The limitation of the electro-optical response is due to the low dielectric constants and the breakdown voltage limitation of the gate dielectric layer which limits the accumulated carrier density in all solid FET devices. Further optimizations in the device structure are

suggested by utilizing a multilayer geometry and substituting ITO layer with a semitransparent film of metallic SWNTs.

Here we propose to introduce an ionic liquid (IL) into the SWNT thin film electro-optical FET. Ionic liquids are highly polar low-melting-temperature binary salts typically comprising nitrogen-containing organic cations and inorganic anions. Since there is no solvent, ILs are distinctly different from aqueous, organic, gel, or polymer electrolytes. Ionic liquids advantageously have high thermal stability, they are nonvolatile, they are compatible with most materials systems, they can be exposed to moderate potential differences without undergoing redox reactions, and they are fluid over a wide temperature range. Due to the formation of an electric double layer (EDL) in which IL functions as a very thin gate insulator,[22-24] typical IL-gated FETs can accumulate carriers with a very high density. ILs can be especially efficient in the case of porous SWNT films with high surface to volume ratio which are easily intercalated by ILs thus providing efficient gating to all layers of the SWNT film in contrast to all-solid state SWNT FET.

Application of a potential between the nanotube film and the remote gate electrode establishes an electric double layer consisting of the excess charge drawn into each layer of individual nanotubes and the cloud of oppositely charged electrolyte ions. Thus, the advantage of using IL dielectrics in SWNT thin film device compared to solid state dielectrics is in the significantly enhanced charge modulation at very low gate voltage.

The Rinzler group reported an electro-optical SWNT FET configuration in which a giant electro-optical modulation of the infrared transmission in the range of the first interband transition of semiconducting SWNTs (S_{11}) was achieved (Figure 3.1).[13]

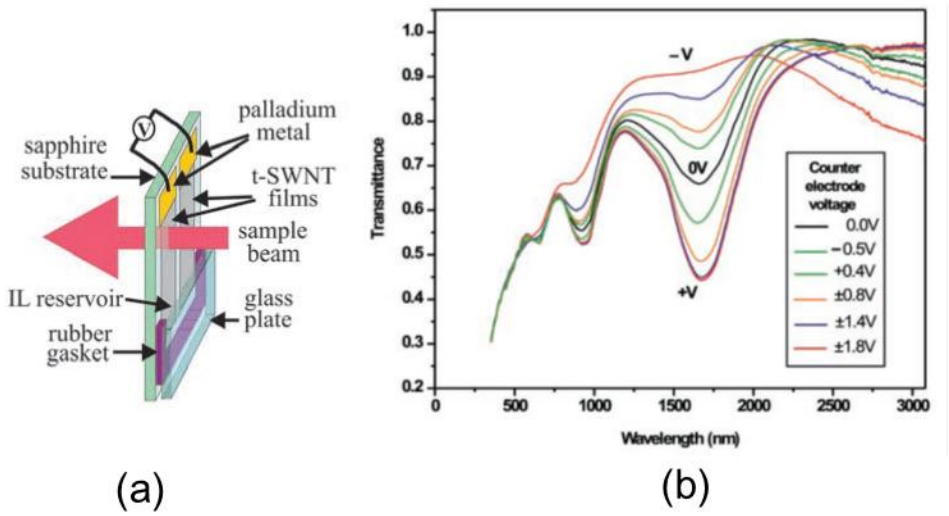

Figure 3.1: (a) Schematic of the IL-gated SWNT thin film FET. (b) Spectral transmittance of the nanotube film FET as a function of applied counter-electrode "gate" voltage. [13]

However, the switching speed of IL based devices is determined by the polarization response time of the IL cation and anion, not by the carrier mobility in the semiconductor channel.[24] This response time is usually very slow, in the range of minutes. The slow response limits the transistor switching speed at room temperature, which is a major disadvantage for the applications of IL based devices.

Very recently, a new type of IL (DEME-TFSI) was developed and used in the Iwasa group as a gate dielectric for electric double layer transistors (EDLTs) (Figure 3.2(b)). [25-28] The molecular structure of DEME-TFSI, which is a highly polar binary salt composed of nitrogen-containing cations and imide anions, is schematically presented in Figure 3.2(a). The electrochemical potential window of this compound is -3V to +2.7 V, and this IL can be used under ambient conditions. It has a higher ionic conductivity and dielectric constant than electrolyte dielectrics. Also, it is solvent-free and compatible with most materials, especially oxide systems, in which it can be exposed to moderate voltages without undergoing redox reactions. Furthermore, the switching of DEME-TFSI EDLTs is much faster than that of other electrolyte/IL-gated EDLTs (Figure 3.3(c,d)). It is the reversible and rapid polarization relaxation of the mobile ions in highly conductive ILs that leads to the fast response and robust properties of DEME-TFSI EDLTs.[22, 25]

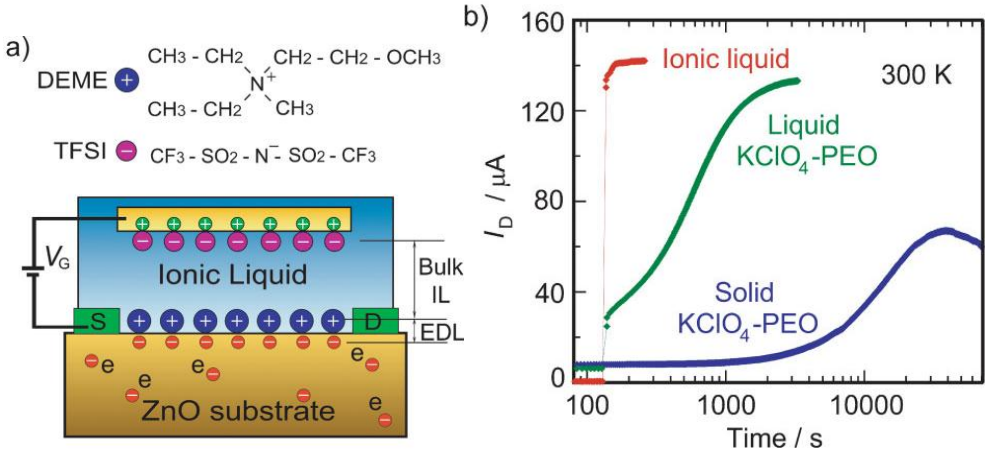

Figure 3.2: (a) Schematic of molecular structures of the IL DEME-TFSI (top) and the cross-section of IL/ZnO EDLT (bottom). Blue, pink, green, and red spheres represent the $DEME^+$ cation, $TFSI^-$ anion, hole, and electron. (b) Comparison of the dynamical response to stepwise pulses of V_G=2 V in EDLTs gated by IL, liquid KClO4/PEO and solid KClO4/PEO electrolytes.[25]

We initially planned to study electro-optical modulation in DEMT-TFSI/SWNT thin film FETs, but we discover that even without gate electrode, a simple two-terminal semiconducting single-walled carbon nanotube (SC-SWNT) channel in contact with an ionic liquid, shown in figure 3.3, induces a very strong electro-optical modulation in a wide spectral range as a result of the position dependent shift of the SWNT Fermi level.

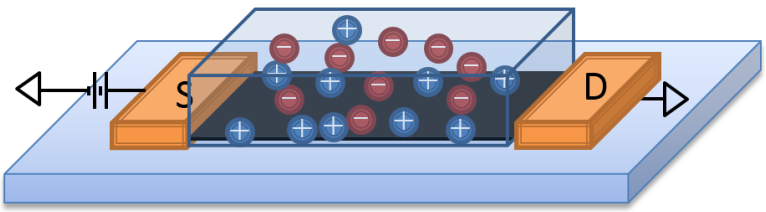

Figure 3.3: Schematic of a two-terminal semiconducting SWNT (SC-SWNT) channel in contact with an ionic liquid.

3.2 Experimental

In this study we use a two-terminal device with gold contacts fabricated on optical substrates, in which active channel consists of the film of SC-SWNTs coated with an ionic liquid (Figure 3.3).

Separated 99% semiconducting SWNTs of average diameter D_{av} = 1.55±0.1nm, purchased from Nanointegris Inc were mostly utilized in this study. Other kinds of SWNTs of different diameters were also utilized: mixed semiconducting and metallic Laser-SWNTs (D_{av} = 1.3±0.1nm) and the HiPCO SWNTs (D_{av} = 1.0±0.2nm) are obtained from Carbon Nanotechnologies, Inc; predominantly semiconducting CoMoCAT SG65 SWNTs (D_{av} = 0.8±0.1nm) were obtained from SouthWest Nanotechnologies, Inc. Separated 99% metallic SWNTs of average diameter D_{av} = 1.55±0.1nm were utilized as the transparent conducting gate electrode in the FET devices. The ionic liquid (DEME-TFSI) was obtained from Kanto Corporation.

60nm thick SWNT thin films were prepared by vacuum filtration and transferred to optical substrates with two pre-patterned Cr/Au (10nm/100nm) electrodes to form rectangular channels of length 1000-2000 μm and width 200-400 μm(shown in Figure 3.4(a)). In this study, another type of optical substrate with 20 pre-patterned in-line electrodes (shown in Figure 3.4(b)) were fabricated to study the spatial distribution of the electrical potential U along the SWNT channel. The electrode patterns were made by a photolithography process followed by e-beam metal deposition. The electrodes were 3 μm wide and more

densely populated in the vicinity of the current contacts. 20 in-line electrodes are numbered from #1 to # 20 in order from left to right. The current was applied between contacts #2 and #19, so contacts #1 and #20 were used to measure the potential under the current electrodes excluding the contact contribution. The measurements were conducted utilizing a Keithley 2700 multichannel data acquisition system.

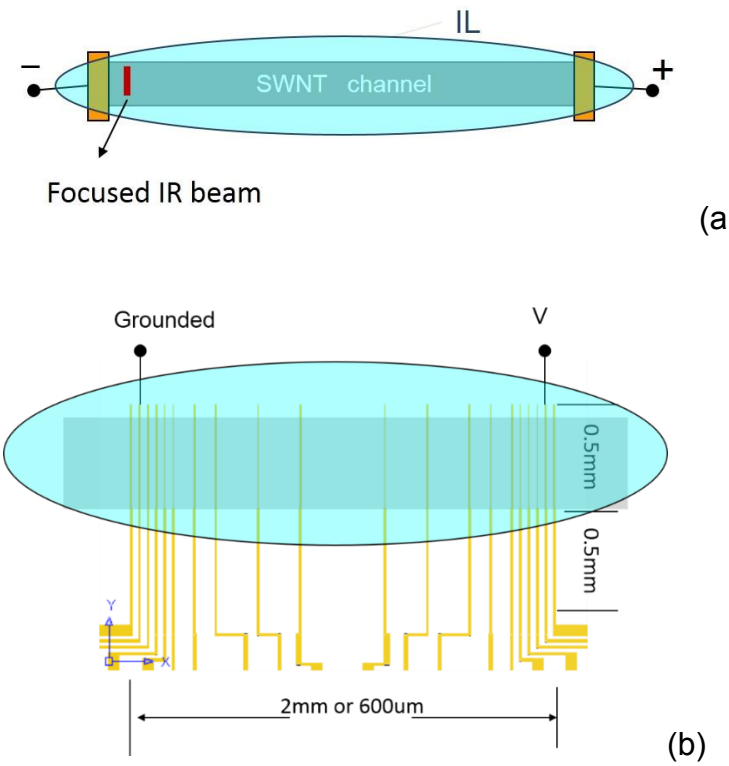

Figure 3.4: Schematic of the devices used in the experiment. (a) Schematic of the setup for electro-optical measurements with narrow infrared beam scanning the length of the SWNT channel. (b) Schematic of the SC-SWNT film on a pre-patterned substrate with 20 in-line electrodes coated with IL.

For the device preparation, SWNT films were transferred onto optical substrate with pre-patterned electrodes and annealed in vacuum to reduce the effect of environmental doping.[29] A thin frame of poly(dimethylsiloxane) (PDMS, thickness ~200 μm), was placed around the SWNT channel to contain a thin uniform layer of ionic liquid; after filling the frame the ionic liquid was covered with a sapphire window (Figure 3.5).

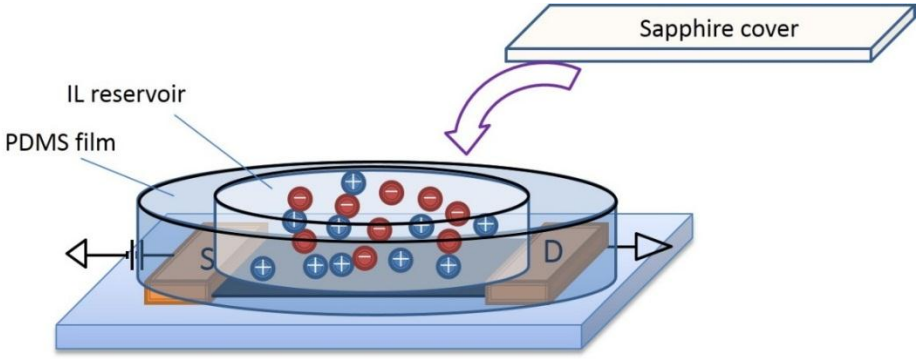

Figure 3.5: Schematic of device preparation.

For the device characterization, we utilized the multi-functional spectroscopic setup described in chapter 2, but infrared beam from the monochromator (Horiba Yobin-Robin ihr 320) was focused into a narrow 10 μm wide strip (Figure 3.4(a)) by utilizing an aperture in infrared microscope (Bruker Hyperion 1000). The experiment setup can provide two measurement modes: 1) Measurements of local absorption spectra in the spectral range 4000-16000 cm^{-1} (wavelength 2500-625nm) at any position along the SWNT channel as a function of applied voltage; 2) Measurements of the electro-optical response at fixed wavelength while scanning the channel length. The sample was mounted on a motorized micrometer stage so that the electro-optical response could be acquired along the length of the SWNT channel. The sign and amplitude of the electro-optical response were measured utilizing the two frequency modulation technique with two lock-in amplifiers (SRS 830): the IR radiation was chopped at frequency (230-400Hz) and the voltage across the channel was modulated in the form of square-wave pulses of low frequency (0.5-10 Hz).

3.3 Results and discussion

Before the application of DEME-TFSI ionic liquid to the SWNT channel, the annealed SWNT channel shows a linear current-voltage (I-V) relationship (Figure 3.6(a)) and no change in the optical transparency of the films was observed under an applied voltage. However, after SWNT channel is coated with a thin layer of DEME-TFSI ionic liquid, the I-V characteristics became strongly non-linear with the resistance decreasing by an order of magnitude at the highest applied voltage (Figure 3.6(a)). In addition, we observed a strong modulation of the infrared transmission in the vicinity of electrodes (Figure 3.6(b)); the strongest electro-optical modulation was observed at a wavelength of 1.8 μm which corresponds to the first interband transition of the semiconducting SWNTs (S_{11}); the time needed for the development of the change is shorter than 1 second. The amplitude and sign of the electro-optical effect changed with the position of the IR beam along the channel and with the amplitude and polarity of the applied voltage.

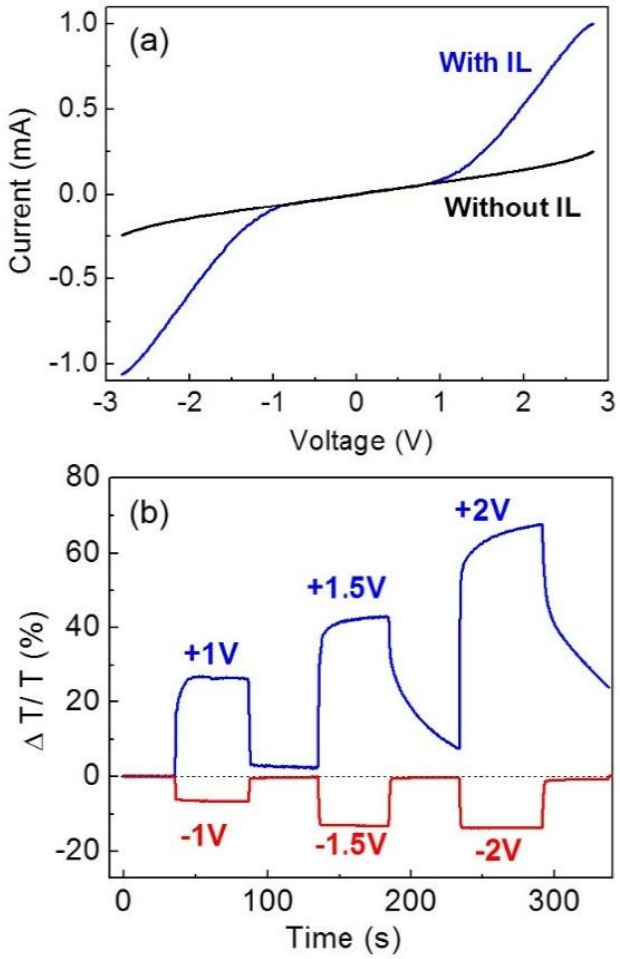

Figure 3.6: (a) Linear I-V characteristic of intrinsic SWNT thin film and Non-linear I-V characteristic of SWNT thin film channel after coating with ionic liquid. (b) Electro-optical modulation of infrared transmittance ΔT/T at wavelength 1.8 μm as a function of the amplitude and polarity of applied voltage.

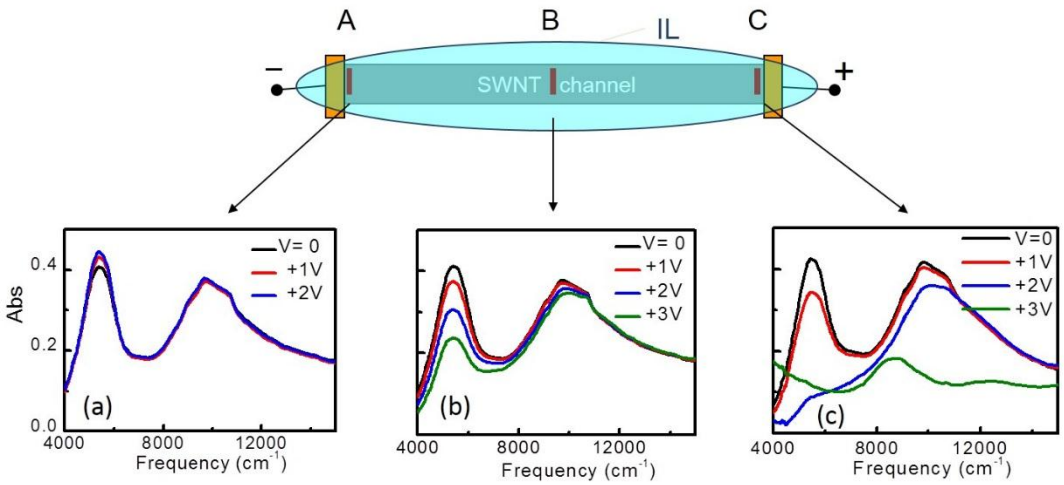

Figure 3.7: Schematic of the setup for electro-optical measurement with the narrow infrared beam scanning the length of the SWNT channel. (a-c) Modification of the absorption spectra of the SWNT film at negative and positive electrodes (positions A and C, respectively, and the center of the channel (position B).

Figure 3.7(a)-(c) show the absorption spectra in the segments of the SWNT film adjacent to the negative and positive electrodes (Positions A and C, respectively) and at the central Position B as a function of applied voltage. In the absence of an applied voltage (V=0), the absorption spectrum shows a position independent S_{11} peak which is partially suppressed due to residual environmental doping. In the vicinity of the negative current contact position A, the application of a voltage leads to a slight enhancement of the S_{11} peak as the film approaches its intrinsic state as shown in Figure 3.7(a). In the vicinity of the positive current contact at the position C there is a strong suppression of the S_{11} peak and the S_{11} feature completely disappears at V=2V; a further increase of the voltage leads to

the complete suppression of the S_{22} peak and the appearance of a new peak located between the initial S_{11} and S_{22} transitions shown in Figure 3.7(c), which was first observed in 1998 under extreme iodine doping of soluble SWNTs,[30] and recently rediscovered and ascribed to a 3-particle excited state. [31] The central part of the sample shows the same behavior that is observed at the positive electrode but with smaller amplitude (Figure 3.7(b)).

The electro-optical modulation of the infrared transmission has very strong spatial dependence. To study this dependence, we mounted the device on a motorized micrometer stage so that the electro-optical response at fixed wavelength could be acquired along the length of the SWNT channel. The spatially resolved distribution of the electro-optical modulation of the infrared transmission [$\Delta T(V,x)/T_{V=0}(\%)$], at a fixed wavelength of 1800 nm is presented in Figure 3.8(a), 8(b) as a function of amplitude and the polarity of applied voltage. With the application of a voltage a region of slightly decreasing IR transmittance develops near the negative electrode, while the transmittance in the vicinity of the positive electrode strongly increases and the region of increasing transmittance asymmetrically expands to occupy most of the of the channel length, while the region of negative electro-transmittance localizes within 50 μm of the negative electrode (Figure 3.8(a)). Interchange of the contact polarities lead to an inversion of the sign of the electro-optical modulation at the electrodes while the transmittance in the central region of the SWNT channel remains positive and independent of the polarity of the applied voltage. Figure 3.8(c) presents the

voltage dependence of ΔT/T at different positions A, B and C along the SWNT channel.

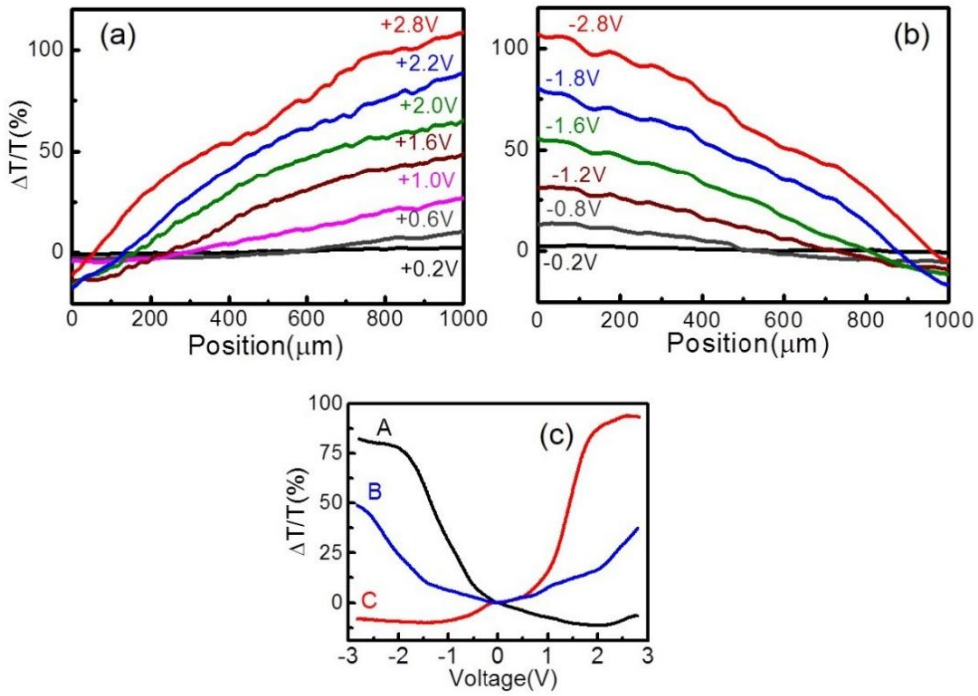

Figure 3.8: (a) (b) Spatial dependence of the electro-optical modulation of infrared transmittance ΔT/T on the amplitude and polarity of the applied voltage. (c) Voltage dependence of ΔT/T at different positions along the SWNT channel.

To further characterize the device, we utilized the optical substrate with 20 in-line electrodes to study the spatial distribution of the electrical potential U along the SWNT channel as a function of the applied voltage. The length of the SWNT thin film channel is 2000 μm and width is 200 μm (shown in Figure 3.9(a)). The current was applied between contacts #2 and #19, the other contacts are used to measure the potential distribution utilizing a Keithley 2700 multichannel data acquisition system. The experimental setup was tested on a semiconducting

SWNT sample before application of the ionic liquid and showed a linear distribution of electrical potential U(x) along the SWNT channel (Figure 3.9(b)) and no indication of detectable electro-optical effects.

After application of the IL to SWNT thin film channel (Figure 3.9(c)), the U(x) distribution shows strongly nonlinear features (Figure 3.9(d), 3.9(e)). With increasing voltage we observed an upward bending of the U(x) curve with formation of the high electric field region in the vicinity of the negative electrode. At the highest applied voltage, V=2V, the high electric field region compresses to a segment <30 μm (Figure 3.9(d)). The strength of electric field at the negative current contact reached 500 V/cm, exceeding the strength of the field at the positive contact by more than two orders of magnitude. On reversing the device polarity the high field region shifted to the opposite contact (Figure 3.9(e)).

A time of ~100 ms is needed for the formation of the strongly non-linear potential profile, shown in Figure 3.10. This implies that the response time of the electro-optical modulation in DEME-TFSI / SWNT film channel device is in the range of 100ms.

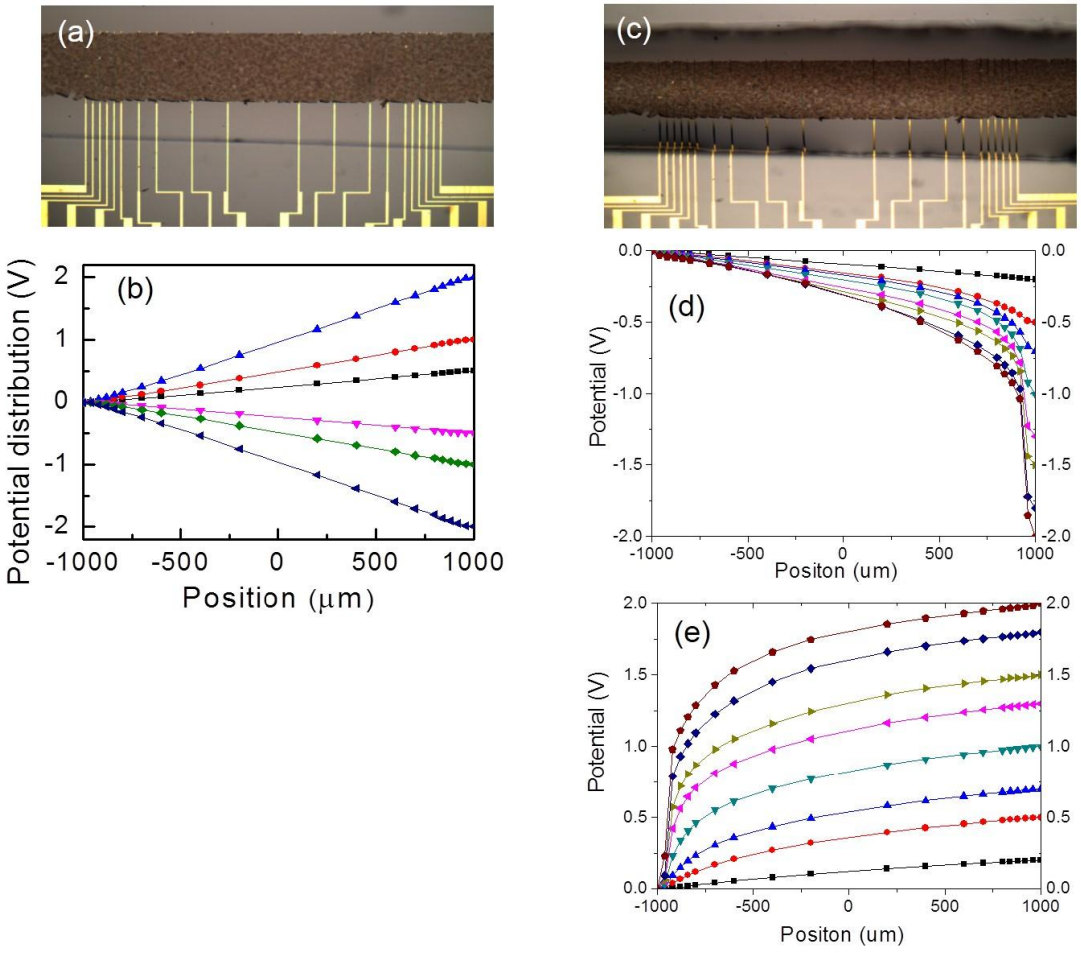

Figure 3.9: (a) Configuration of the SC-SWNT film on a pre-patterned substrate with 20 in-line electrodes. (b) Linear spatial distribution of the electrical potential along the SWNT channel before coating with ionic liquid. (c) Configuration of the SC-SWNT film on a pre-patterned substrate with 20 in-line electrodes coated with IL. (d) (e) Non-linear spatial distribution of the electrical potential along the SWNT channel after coating with ionic liquid as a function of the amplitude and polarity of the applied voltage.

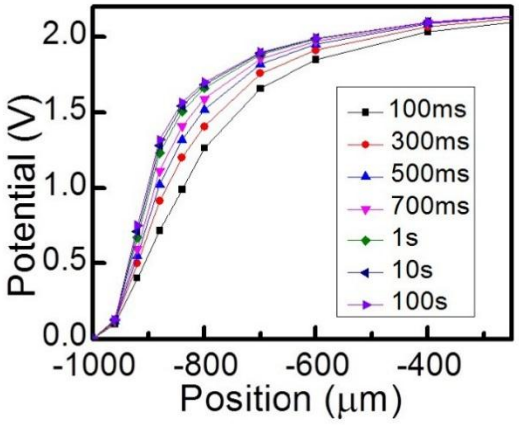

Figure 3.10: The temporal evolution of the electrical potential distribution along the channel.

3.4 Phenomenological model

The SWNT network is treated as a semiconducting medium and the schematic relationship of the band structure to the charge distribution in the ionic liquid is presented in Figure 3.11.

In the absence of the ionic liquid (at V=0, Fig. 3a), absorption spectrum shows a position independent S_{11} peak, the SWNT film can be described by a position independent Fermi level E_F and the relationship of the Fermi level to the positions of the valence (V) and conduction (C) bands does not change under an applied voltage; thus all the bands and the local chemical potential line acquire the slope dV/dx (Figure 3.11(b)) as confirmed by the linear potential distribution presented in Figure 3.9(b) ($V \neq 0$). In the presence of the ionic liquid at zero voltage the $DEME^+$ cations and $TFSI^-$ anions are distributed uniformly along the

surface of SWNT film (Figure 3.11(c)) with the local value of E_F independent of position along the channel, as confirmed by the position independent absorption spectra.

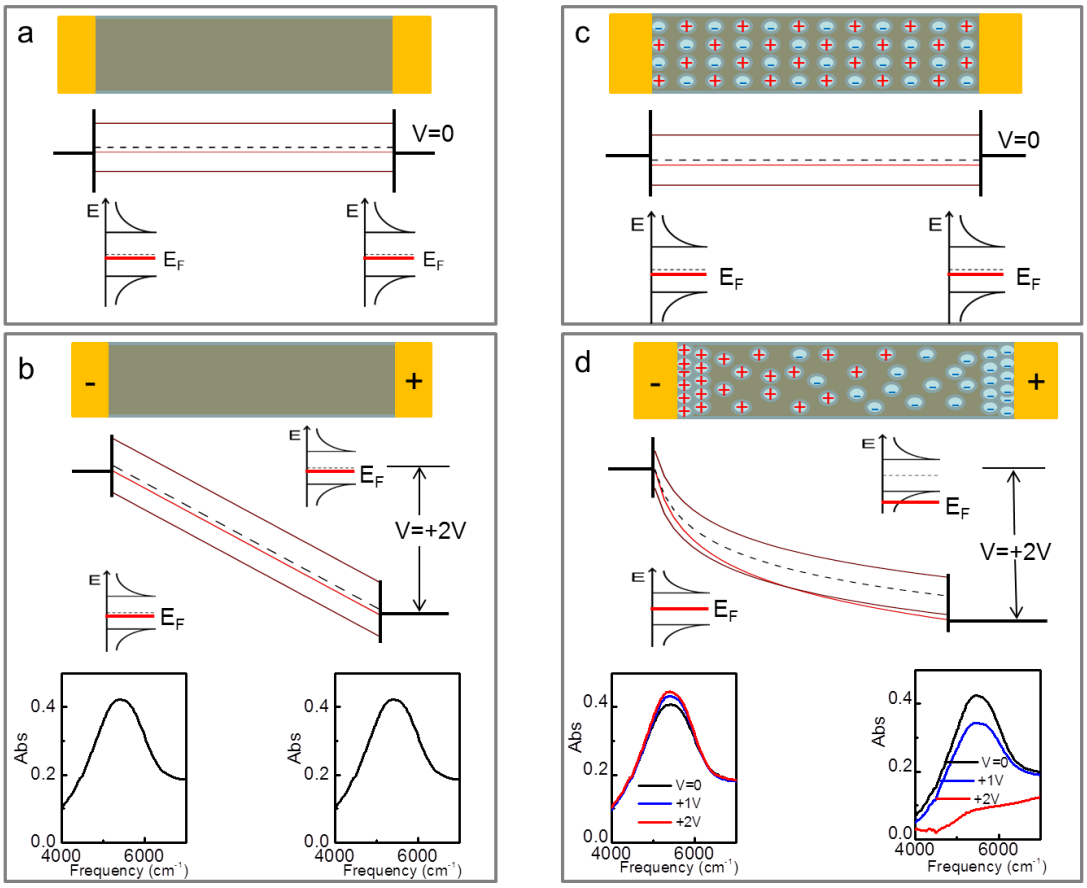

Figure 3.11: Model of the observed non-linear electrical and electro-optical effects in SWNT thin films in ionic liquid. (a) (b) Spatial distribution of the SWNT valence and conductance bands, Fermi level and electronic density of states (DOS) in the SWNT channel without ionic liquid. (a) V = 0 V, and (b) V = 2 V. (c) (d) Spatial distribution of cations and anions in the ionic liquid, SWNT valence and conductance bands, Fermi level, DOS in SWNT channel coated by ionic liquid. (c) V = 0 V, and (d) V = 2V. S_{11} band under applied voltage in the vicinity of electrodes, (b) with IL (d) without IL.

It is well known that the issue of Schottky barrier formation at individual carbon nanotube—metal junctions is of crucial importance for nanotube-based electronic devices.[32-36] But in the case of our SWNT thin film system with or without IL coating layer, the band bending due to the Schottky barrier is undetectable by the optical method because the length of the depletion region is in the sub-micron range which is much shorter than the resolution of microscope system (~10 μm) as well as the characteristic length (~30μm) of the observed electro-optical modulation. Thus, it is unlikely that the Schottky barrier is involved in this electro-optical modulation effect, in the following discussion I will neglect the Shottky barrier structure at nanotube film-metal junction.

Upon application of a voltage the distribution of the anions and cations becomes polarized, thereby generating a high concentration of cations in the vicinity of positive electrode and anions at the negative electrode and forming a lateral electric double layer capacitor (Figure 3.11(d)).[25-28, 37, 38] This spatial redistribution of ions shifts the local Fermi level in the carbon nanotube network in different directions at the two electrodes: down in energy towards the highly p-doped state at the positive electrode (as confirmed by the strong suppression of the S_{11} absorption band), and up in energy at the negative electrode towards the intrinsic state as indicated by the slightly increasing S_{11} absorption. The final distribution of the electrical potential along the SWNT channel is established through the equilibration of the ionic and SWNT charge distribution as determined by the position dependent shift of the Fermi level. This distribution is

presented schematically in Figure 3.11(d): the highly resistive region of the channel in the vicinity of the negative electrode which constitutes the intrinsic state experiences most of the potential drop resulting in the high electric field.

Given the p-type nature of the device it can be envisioned as two rectifying metal-semiconductor junction biased in opposite directions and connected in series: one operating under forward bias at the hole injecting positive contact and the other operating under reverse bias at the negative contact. We suggest that the ions in the ionic liquid are able to function in the same manner as the donor and acceptor sites in the channel of a heavily doped semiconductor, but due to the nature of the device the ionic liquid is much more efficient in compensating the injected charge. This is because the ionic liquid can dynamically adjust to the electrostatic charge on the carbon nanotubes; the nature of the SWNTs themselves allow for a very effective geometry in which the anions can diffuse inside the carbon nanotubes and within the galleries between the SWNTs. At small operating voltages ($V < 1V$), the I-V characteristics of the device remain linear (Figure 3.6(a)) and the absorption spectrum shows a rigid band shift of the Fermi level with removal of electron density from the S_1 level and a reduction in the intensity of the S_{11} transition (Figure 3.7(c)). Beyond this point ($V > 1V$), however, the I-V characteristics diverge and we identify this region of the doping profile with the approach to the polarization catastrophe;[39-41] this is also reflected in the absorption spectrum in the region of the interband electronic transitions, which undergoes a drastic modification at these voltages.

The onset of the polarization catastrophe (PC) has been studied in a number of heavily doped semiconductors and it is expected to occur at donor concentrations of $N \approx 10^{19}$ cm^{-3}, at which point the dielectric constant (ε) of the medium becomes very large and as $\varepsilon \rightarrow \infty$, the dielectric becomes a metal. The ionic liquid DEME-TSFI has an intrinsic ionic concentration, $N > 10^{21}$ cm^{-3} and will represent a large fraction of the volume of the active channel in our measurements and thus we expect that it is possible to approach the PC and the metal-insulator transition of the SC-SWNT films studied in our experiments; ionic concentrations of $N \approx 10^{20}$ cm^{-3}, have been achieved in previous experiments using this ionic liquid which was sufficient to induce superconductivity in such insulators as $SrTiO_3$ and ZrNCl, and to efficiently gate ZnO, Bi_2Te_3 and graphene FET channels. [25-28, 37, 38]

3.5 Potential applications of the observed electro-optical effects

The results and discussion above are focused on the narrow spectrum range in the vicinity of the interband transition. In addition, the shifting of the Fermi level below the top of the valence band not only suppresses the S_{11} and S_{22} interband transitions but also produces free carrier excitations (transitions S_{fc}, Figure 3.13(a)) in the mid- and far-infrared spectral ranges. Figure 3.12 shows the transfer of the spectral weight from the near-IR S_{11} absorption to the mid-IR and far-IR range which includes the 3-5 and ~10 μm atmospheric transparency bands. The pristine SWNT film has weak mid-IR absorption; the observed strong electromodulation in mid/far-IR spectral range suggests that SWNT thin film is a remarkable material for IR electro-optical applications.

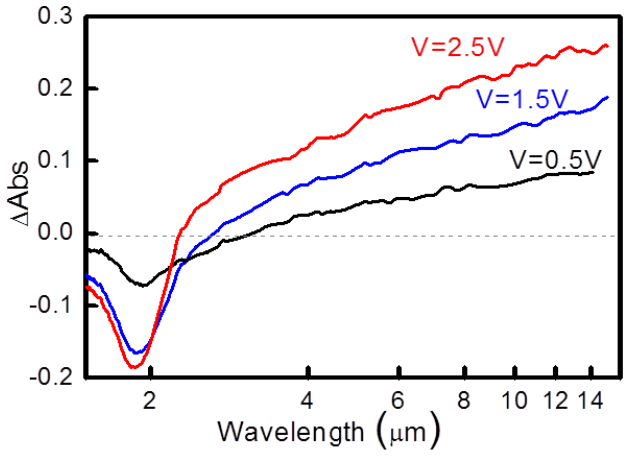

Figure 3.12: Electro-optical modulation of S11 absorption accompanied by modulation of mid-infrared and far-infrared absorption originating from S_{fc} excitations.

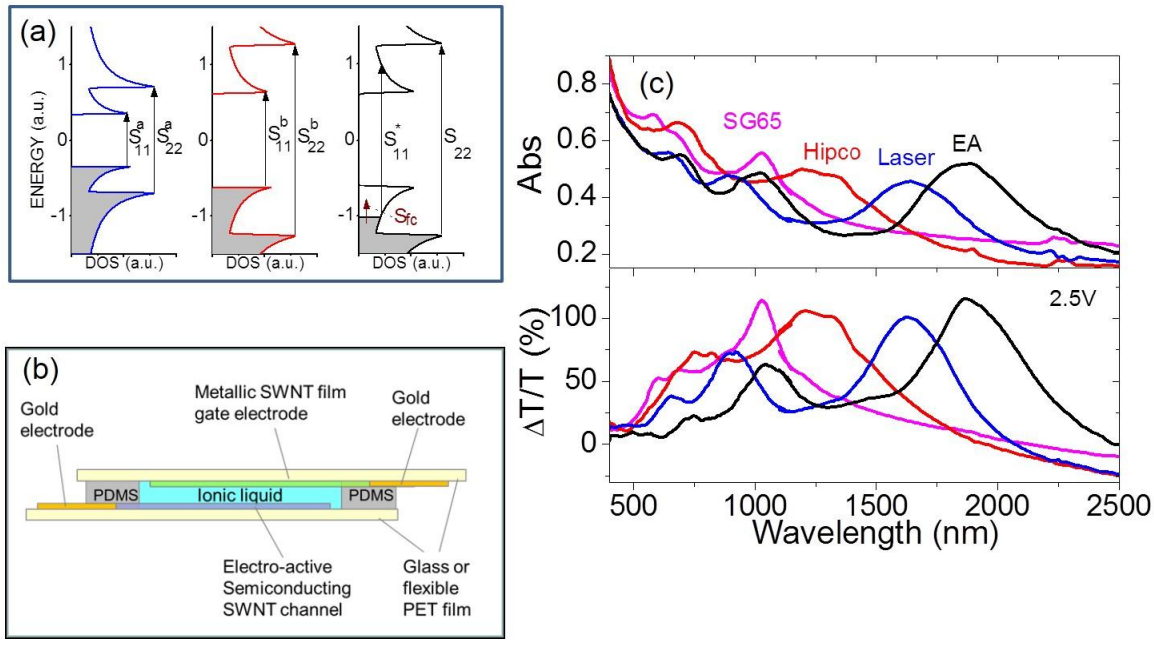

Figure 3.13: **(**a) Electronic density of states (DOS) of semiconducting SWNTs of larger diameter/smaller bandgap (left); smaller diameter/larger bandgap (center); and in the case of the shift of chemical potential inside the valence band leading to the suppression of interband transitions S_{11} and S_{22} and appearance of low energy free carrier absorption Sfc(right). (b) Schematic of electro-optical field effect transistor (EO-FET) with semiconducting SWNTs as electro-active channel and metallic SWNTs as gate electrode separated by a layer of ionic liquid. (c) Spectra of absorption (Abs) and electro-optical modulation of transmission $\Delta T/T$ utilizing EO-FETs with semiconducting SWNTs of four different diameters from 0.8 to 1.55nm with the spectra of electro-optical modulation extending from visible to near-infrared range (500 to 2500nm).

In addition to the IR range, the spectral range of the electro-optical modulation can be further extended into the visible range. The bandgap in SC-SWNTs is inversely proportional to the SWNT diameter and for smaller diameter SWNTs, the S_{11} absorption band is shifted to higher energy range (Figure 3.13(a)). In order to explore the visible part of the spectral range of the electro-optical modulation, we fabricated a set of gated electro-optical devices in which

the channels were comprised of SWNTs of four different diameter distributions: D_{av} = 1.55±0.1nm, 1.3±0.1nm, 1.0±0.2nm, and 0.8±0.1nm. The transparent gate electrodes were made out of a thin film of 99% metallic SWNTs with a thin layer of ionic liquid separating the electro-active semiconducting SWNT channel from the transparent gate electrode as shown schematically in Figure 3.13(b). The thickness of the working film is 90nm and the thickness of the transparent electrodes (99% metallic SWNT thin film) is 10nm. Figure 3.13(c) presents spectra of absorbance (Abs) and electro-modulated transmittance $\Delta T/T$ for all the devices. Since the IR-Vis beam transmits through both the working SWNT thin film and the metallic film electrodes, a weak M_{11} peak at 700 nm can be observed in all spectra. Electro-modulated spectra which involve S_{11}, S_{22} and even M_{11} bands extend from the near-infrared to the visible (2500 to 500 nm).

Recently electrochromic materials (material which can change their optical properties under an applied voltage), have emerged as a promising technology for engineering smart windows which are capable of reducing the heating and cooling loads and increasing the lighting efficiency in buildings,[42-44] and improving thermal control and reducing fuel consumption in vehicles.[45] Carbon nanotubes have been considered in electrochromic smart window design as the transparent conducting electrode for replacement of indium tin oxide.[13-17, 43] The current study together with earlier developments[13, 18-20] suggests that SWNTs could contribute to this technology as an active electrochromic layer in smart window applications.

Figure 3.14 provides some alternative configurations for our SWNT thin film based electro-optical devices. Figure 3.14(a) presents a schematic of a SWNT electro-optical modulator in which the voltage is applied between two closely situated electrodes and allowed to uniformly switch the optical transparency of the large area of the device external to the contacts; Figure 3.14(c) illustrates the experimental realization of this configuration and shows the transmission data for such a device as a function of the applied voltage and position. Figure 3.14(b) presents a schematic of another SWNT thin film based electro-optical functionality in which a set of interdigitated electrodes is inserted along the channel; under application of a voltage a periodic spatial modulation of transmittance can be produced with the amplitude and phase controlled by the amplitude and polarity of the applied voltage as experimentally demonstrated in Figure 3.14(d). The period of modulation can also be changed by addressing different groups of electrodes; such a system can be utilized as an electrically configurable diffraction grating for an infrared spectrophotometer in which the wavelength can be scanned without moving parts.

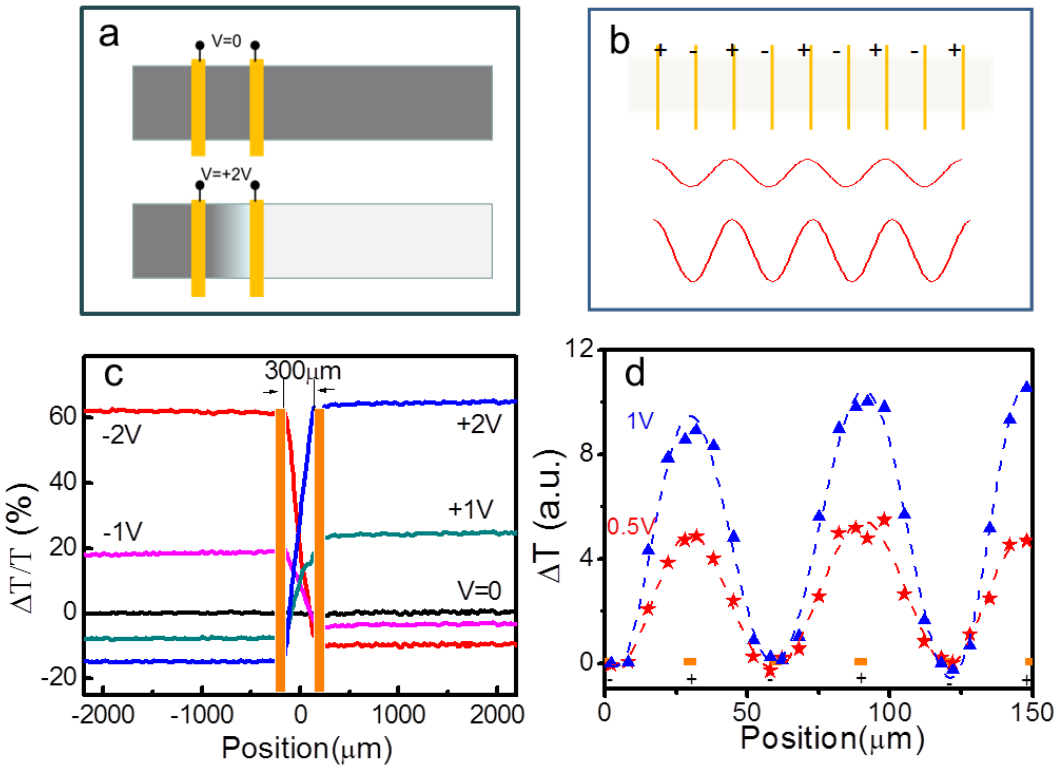

Figure 3.14: Electro-optical configuration and functionalities based on the SWNT thin film channel in an ionic liquid. (a) Schematic of setup in which large area of SWNT film can be switched from an opaque to the transparent state by application of voltage across two closely separated electrodes, and (c) its experimental demonstration. (b) Schematic of a set of interdigitated electrodes inserted in the SWNT channel to be used to generate periodic spatial electro-optical modulation of infrared transmittance with the amplitude and phase controlled by the amplitude and polarity of the applied voltage, and (d) experimental demonstration.

3.6 Summary

We found that the application of an electrical potential to a SC-SWNT film in the presence of an ionic liquid leads to a position dependent modulation of the optical transmission which is associated with the injection of holes into the SC-SWNT valence band, dynamically compensated by the polarized medium of the ionic liquid. We suggest that the nonlinear I-V curves and the modified band electronic structure signal the onset of the polarization catastrophe previously observed in heavily doped semiconductors. The electrical control of the local optical transmission suggests the applications of SC-SWNT thin films as electrically configurable optical media. The broad spectral range of electro-optical modulation, which extends from the far-infrared to the visible, suggests that the SWNT thin films are candidate materials for utilization as the active layer in electrochromic smart windows.

References:

1. Dresselhaus, M. S., Dresselhaus, G. & Avouris, P. (eds.) Carbon Nanotubes: Synthesis, Structure, Properties and Applications (Springer-Verlag, Berlin, 2001).
2. Dresselhaus, M. S., Dresselhaus, G. & Jorio, A. Carbon Nanotubes: Advanced Topics in the Synthesis, Structure, Properties and Applications (Springler-Verlag New York, 2008).
3. Avouris, P., Freitag, M. & Perebeinos, V. Carbon-Nanotube Photonics and Optoelectronics. Nature Photonics 2, 341-350 (2008).
4. Freitag, M., Martin, Y., Misewich, J. A., Martel, R. & Avouris, P. Photoconductivity of Single Carbon Nanotubes. Nano Lett. 3, 1067-1071 (2003).
5. Levitsky, I. A. & Euler, W. B. Photoconductivity of Single-Wall Carbon Nanotubes Under Continuous-Wave Near-Infrared Illumination. Appl. Phys. Lett. 83, 1857-1859 (2003).
6. Freitag, M. et al. Hot Carrier Electroluminescence from a Single Carbon Nanotube. Nano Lett. 4, 1063-1066 (2004).
7. Itkis, M. E., Borondics, F., Yu, A. & Haddon, R. C. Bolometric Infrared Photoresponse of Suspended Single-Walled Carbon Nanotube Films. Science 312, 413-416 (2006).
8. Tarasov, M., Svensson, J., Weis, J., Kuzmin, L. & Campbell, E. Carbon Nanotube Based Bolometer. JETP Lett. 84, 267-270 (2006).
9. Lee, J. U., Codella, P. J. & Pietrzykowski, M. Direct Probe of Excitonic and Continuum Transitions in the Photocurrent Spectroscopy of Individual Carbon Nanotube p-n Diodes. Appl. Phys. Lett. 90, 053103 (2007).
10. Mann, D. et al. Electrically DrivenThermal Light Emission from Individual Single-Walled Carbon Nanotubes. Nat. Nanotechnol. 2, 33-38 (2007).
11. Itkis, M. E., Yu, A. & Haddon, R. C. Single-Walled Carbon Nanotube Thin Film Emitter-Detector Integrated Optoelectronic Device. Nano Lett. 8, 2224-2228 (2008).
12. St-Antoine, B. C., Menard, D. & Martel, R. Single-Walled Carbon Nanotube Thermopile For Broadband Light Detection. Nano Lett. 11, 609–613 (2011).
13. Wu, Z. et al. Transparent, Conductive Carbon Nanotube Films. Science 305, 1273-1276 (2004).
14. Gruner, G. Carbon Nanotube Films for Transparent and Plastic Electronics. J. Mater. Chem. 16, 3533-3539 (2006).
15. Zhang, D. et al. Transparent, Conductive, and Flexible Carbon Nanotube Films and Their Applications in Organic Light-Emitting Diodes. Nano Lett. 6, 1880-1886 (2006).
16. Zhang, M. et al. Strong, Transparent, Multifunctional, Carbon Nanotube Sheets. Science 309, 1215-1219 (2005).

17. Kaempgen, M., Duesberg, G. S. & Roth, S. Transparent Carbon Nanotube Coating. Appl. Surf. Sci. 252, 425-429 (2005).
18. Kavan, L. et al. Electrochemical Tuning of Electronic Structure of Single-Walled Carbon Nanotubes: In-Situ Raman and vis-NIR Studies. J. Phys. Chem. B 105, 10764-10771 (2001).
19. Zukalova, M., Tarabek, J., Kalbac, M., Kavan, L. & Dunsch, L. In Situ Optical Spectroelectrochemistry of Single-Walled Carbon Nanotube Thin Films. J Solid State Electrochem. 12, 1279-1284 (2008).
20. Wang, F., Itkis, M. E. & Haddon, R. C. Enhanced Electromodulation of Infrared Transmittance in Semitransparent Films of Large Diameter Semiconducting Single-Walled Carbon Nanotubes. Nano Lett. 10, 937-942 (2010).
21. Perebeinos, V. & Avouris, P. Exciton Ionization, Frank-Keldysh, and Stark Effects in Carbon Nanotubes. Nano Lett. 7, 609-613 (2007).
22. Misra, R., McCarthy, M. & Hebard, A. F. Electric Field Gating with Ionic Liquids Appl. Phys. Lett. 90, 052905 (2007).
23. Lee, J., Panzer, M. J., He, Y., Lodge, T. P. & Frisbie, C. D. Ion Gel Gated Polymer Thin-Film Transistors. J. Am. Chem. Soc 129, 4532-4533 (2007).
24. Cho, H. J. et al. High-Capacitance Ion Gel Gate Dielectrics with Faster Polarization Response Times for Organic Thin Film Transistors. Adv. Mater. 20, 686-690 (2008).
25. Yuan, H. T. et al. High-Density Carrier Accumulation in ZnO Field-Effect Transistors Gated by Electric Double Layers of Ionic Liquids. Adv. Funct. Mater. 19, 1046-1053 (2009).
26. Ye, J. T. et al. Liquid-Gated Interface Superconductivity on an Atomically Flat Film. Nat. Mat. 9, 125-128 (2010).
27. Ye, J. T. et al. Accessing the Transport Properties of Graphene and Its Multilayers at High Carrier Density. PNAS 108, 13002-13006 (2011).
28. Yuan, H. T. et al. Liquid-Gated Ambipolar Transport in Ultrathin Films of a Topological Insulator Bi2Te3. Nano Lett. 11, 2601–2605 (2011).
29. Itkis, M. E. et al. Spectroscopic Study of the Fermi Level Electronic Structure of Single Walled Carbon Nanotubes. Nano Lett. 2, 155-159 (2002).
30. Chen, J. et al. Solution Properties of Single-Walled Carbon Nanotubes. Science 282, 95-98 (1998).
31. Matsunaga, R., Matsuda, K. & Kanemitsu, Y. Observation of Charged Excitons in Hole-Doped Carbon Nanotubes Using Photoluminescence and Absorption Spectroscopy. Phy. Rev. Lett. 106, 037404 (2011).
32. McEuen, P. L. & Park, J.-Y. Electron Transport in Single-Walled Carbon Nanotubes. MRS Bull., 272-275 (2004).
33. Yaish, Y. et al. Electrical Nanoprobing of Semiconducting Carbon Nanotubes Using an Atomic Force Microscope. Phys Rev. Lett. 92, 046401 (2004).

34. Kang, D. et al. Adsorption-Induced Conversion of the Carbon Nanotube Field Effect Transistor from Ambipolar to Unipolar Behavior. Appl. Phys. Lett. 86, 093105 (2005).
35. Nosho, Y., Ohno, Y., Kishimoto, S. & Mizutani, T. Relation Between Conduction Property and Work Function of Contact Metal in Carbon Nanotube Field-Effect Transistors. Nanotechnology 17, 3412-3415 (2006).
36. Chai, Y. et al. Low-Resistance Electrical Contacts to Carbon Nanotubes with Graphite Interfacial Layer. IEEE Trans. Electron Dev. 59, 12-19 (2012).
37. Ueno, K. et al. Electric-Field-Induced Superconductivity in an Insulator. Nat. Mat. 7, 855-858 (2008).
38. Ueno, K. et al. Discovery of Superconductivity in KTaO3 by Electrostatic Carrier Doping. Nat. Nanotech. 6, 408-412 (2011).
39. Frood, D. G. H. A Dielectric Approach to Impurity Conduction. Proc. Phys. Soc. 75, 185-193 (1960).
40. Castner, T. G., Lee, N. K., Cieloszyk, G. S. & Salinger, G. L. Dielectric Anomaly and the Metal-Insulator Transition in n-Type Silicon. Phys Rev. Lett. 34, 1627-1630 (1975).
41. Capizzi, M., Thomas, G. A., DeRosa, F., Bhatt, R. N. & Rice, T. M. Observation of the Approach to a Polarization Catastrophe. Phys Rev. Lett. 44, 1019-1021 (1980).
42. Granqvist, C. G. Electrochromic Materials: Out of a Niche. Nat. Mat. 5, 89-90 (2006).
43. Baetens, R., Jelle, B. P. & Gustavsen, A. Properties, Requirements and Possibilities of Smart Windows for Dynamic Daylight and Solar Energy Control in Buildings: A State-of-the-Art Review. Solar Energy Materials & Solar Cells 94, 87-105 (2010).
44. Granqvist, C. G. Oxide Electrochromics: An Introduction to Devices and Materials. Solar Energy Materials & Solar Cells 99, 1-13 (2012).
45. Jaksic, N. I. & Salahifar, C. A Feasibility Study of Electrochromic Windows in Vehicles. Solar Energy Materials & Solar Cells 79, 409-423 (2003).

Chapter 4 Effect of Metal Deposition on the Conductivity of SWNT Networks

4.1 Introduction

4.1.1 Electronic properties of SWNT thin films

The interest in electronic applications of the SWNTs derives from the remarkable electronic properties associated with their unique quasi-1D structure. High mobility of the charge carriers and their ballistic transport, for example, have led naturally to consideration of SWNTs as replacement for Si in future generation devices.[1-5] However, despite the exceptional properties and many notable achievements in devices constructed on individual SWNTs, there are major challenges in scaling to any realistic type of system based on individual SWNTs. The lack of practical methods to yield good device-to-device reproducibility limits the application of individual SWNTs. A 2D system that involves large numbers of nanotubes assembled in a random network with thicknesses between sub-monolayer to sub-micron avoids these challenges.[6-10] It is believed that SWNTs in networks offer the most technologically realistic integration path, at least for the foreseeable future. 2D aligned SWNT arrays in which the SWNT–SWNT overlap junctions is absent are also of practical interest, but here we only consider thin films made of randomly assembled SWNTs.

Among all nanotube film development and research, transparent electrodes hold the most realistic promise for applications in the foreseeable future. Transparent electrical conductors are critical component of displays,

image recorders, solar cells, and solid state LEDs. This kind of electrode requires high conductivity, homogeneity, controllable thickness and optical transparency over the desired spectral range. Continuous SWNT films with a thickness between monolayer and 100nm are considered for large area transparent conducting coating applications including flexible polymer substrates because of the SWNT films extreme mechanical flexibility. In some applications, pristine SWNT films do not possess sufficient electrical conductivity, for example, in comparison to ITO. Thus, enhancement of electrical conductivity of the SWNT films while retaining their high transparency is in important direction for the development of the SWNT based optoelectronics.[10-14]

The SWNT network is a complex system, and it was found that the electrical properties of networks are quite different from that of individual SWNTs.[9] In films that include many SWNT–SWNT junctions, the electrical transport depends on a degree of percolation, density of SWNT–SWNT junctions, the lengths of the SWNTs and the distribution of diameters.

In the films consisting of a mixture of metallic and semiconducting nanotubes, the electrical properties such as conductivity and on/off ratio show a semiconductor-metal transition as the film thickness increases.[9] The conductivities of the extremely thin films show a strong dependence on the film thickness (*t*), which can be expressed by a power law of the form:

$$\sigma = (t - t_c)^{\alpha} \qquad (4.1)$$

where t and t_c are the film thickness and critical thickness (percolation threshold), respectively, and α is a critical exponent.

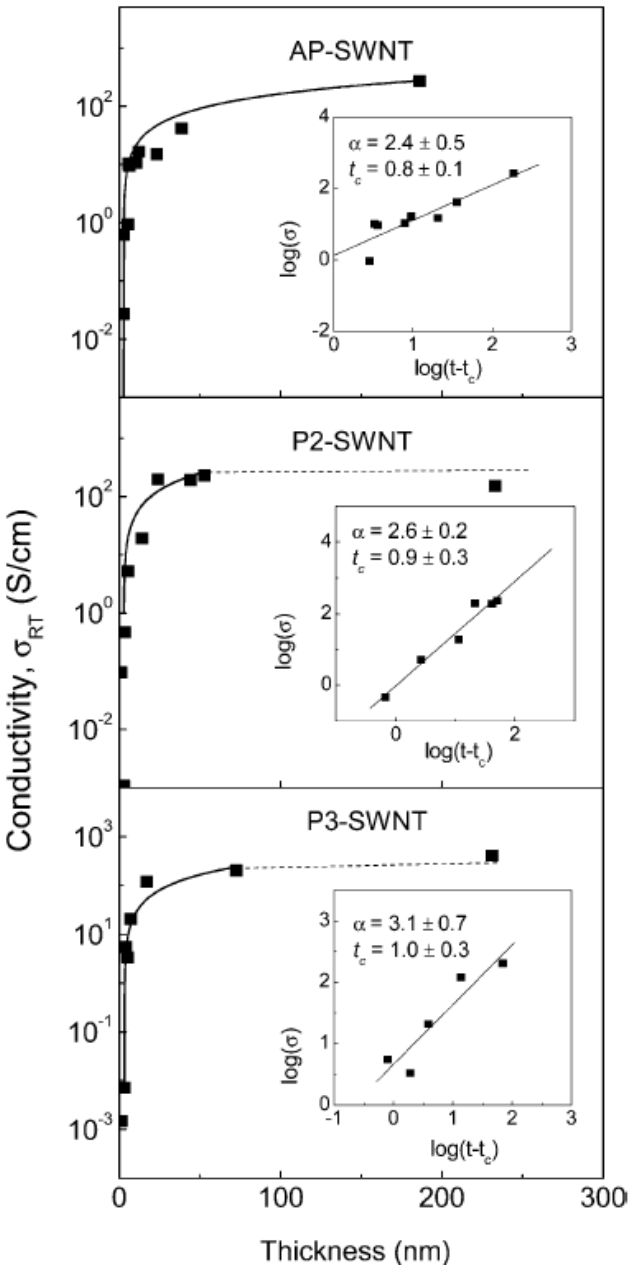

Figure 4.1 Conductivity of AP-SWNT, P2-SWNT, and P3-SWNT films as a function of film thickness.[9]

SWNT thin films thinner than the percolation threshold show semiconducting behavior and can be used as an active layer in thin film transistors and sensors.[15, 16] Films with thickness in the range of 5-100 nm show high optical transparency and electrical conductivity, and can be used as a replacement for ITO electrodes.[10, 15, 17-19] Micrometer-thick CNT films are nanoporous and can be used as electrodes for supercapacitors, fuel cells, and battery applications.[6, 20-26]

In addition to the film thickness (percolation), the conductivity of the films is also dependent on the bundling, surfactant, impurities, defects, length and the diameters of nanotubes. For example, covalent chemistries or harsh conditions of the SWNT processing, can lower the SWNT film electrical conductivity due to the shortening of the nanotubes and attachment of the chemical functionalities to the SWNT walls. Chemical functionalization decreases the conductivity of the films by 2 or 3 orders of magnitude and increases the percolation threshold by a factor of 5.[9]

My research is focused on SWNT film optoelectronics and transparent electrodes; I am extremely interested in SWNT film with thickness in the range of 5-100 nm.

4.1.2 Chemical doping of the SWNT thin films

Similar to semiconductor processing, doping is attractive and essential for performance improvement of transparent and conductive SWNT thin films.

Doping of the SWNTs increases the charge carrier concentration for high electrical conductivity.[27-29] In practice, SWNTs can be doped in various ways, including intercalation of electron donors or acceptors, substitutional doping, encapsulation in the interior spacing, molecular absorption, and covalent sidewall functionalization.[30] In general, the doping processing may lead to increasing carriers concentration, but decreasing mobility. Ionic doping can enhance the conductivity dramatically, while maintaining or improving transparency for Vis-IR light (Figure 4.2 (a)). The n-type doping is much harder to realize than the p-type doping. In the case of p-type ionic chemistry (p-type doping), the S_{11} and in some cases the S_{22} transitions of the semiconducting SWNTs lose spectral weight in the NIR range due to depletion of the valence bands, but this process also produces free carrier excitations (transitions S_{fc}, Figure 4.2 (b)) which absorb in the mid- and far-infrared spectral ranges (Figure 4.2 (a)). The p-type dopants for SWNTs include acids, such as HNO_3, and gases, such as O_2, NO_2, Br_2, and I_2. Charge transfer between dopants and SWNTs increases the number of charge carriers along the SWNTs and improves the conductivity. Such doping is extremely useful for enhancing the performance of a SWNT thin film transparent electrodes, because the resistance dramatically decreases after simple chemical doping treatment. Smalley et al. have observed that Br_2 and K doping increases the CNT thin film conductivity by a factor of 30.[27, 31]

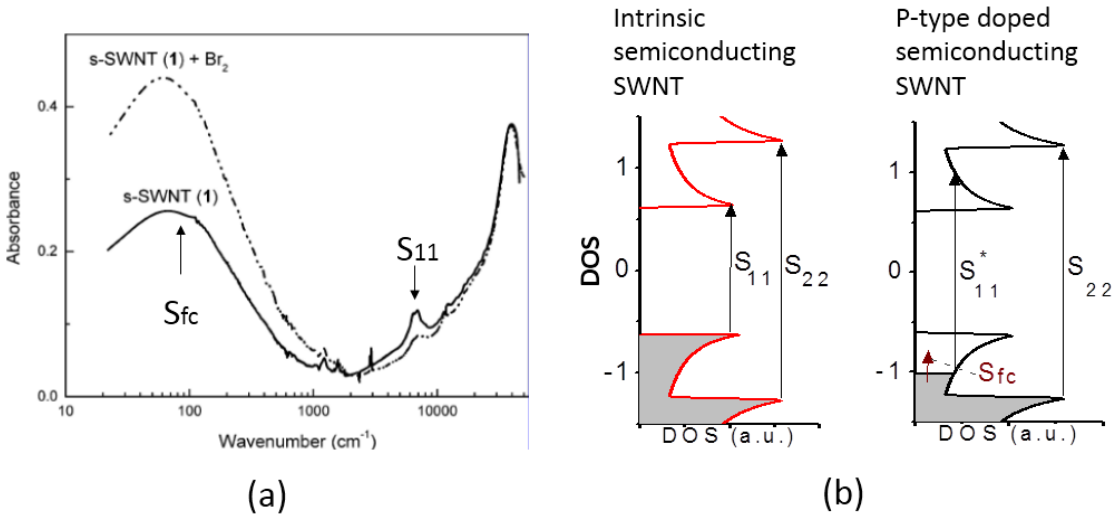

Figure 4.2 (a) IR-Vis-UV spectra of films of SWNT before and after exposure to bromine vapor.[32] (b) DOS of intrinsic semiconducting SWNTs and chemically doped semiconducting SWNTs: chemical doping leads to the suppression of interband transitions S_{11} and S_{22} and appearance of low energy free carrier absorption S_{fc}(right).

4.1.3. Nanotube junctions

Recently, techniques for separating semiconducting and metallic SWNTs were developed. SWNT materials in which 99% of the nanotubes are semiconducting (or metallic) can be separated in bulk by density-gradient ultracentrifugation,[33-36] which may lead to the extension of the SWNT applications. Due to the high intrinsic conductivities of the metallic SWNTs (M-SWNTs) the SWNT films with enriched content of M-SWNTs are attractive as conducting layers, especially for applications requiring high frequency (10 GHz) and high electrical field (>10 kV m^{-1}), or those that benefit from low optical absorption or mechanical robustness.[37, 38] SWNT thin films with enriched content

of SC-SWNTs can behave collectively as semiconducting networks, for use in active electronic devices.[39] High on/off ratios up to 10^5 were achieved for the networks with density close to the percolation threshold.[39]

However, once the thickness of the film is above percolation threshold, the electronic properties of the films fabricated from semiconducting or metallic SWNTs are almost the same, and are similar to the SWNT films fabricated from unseparated SWNT materials. Despite the high intrinsic conductivities of the metallic SWNTs, the room-temperature conductivity of all SWNT films prepared in our group is below 1000 S/cm, which is many orders lower than that of individual M-SWNTs. The SWNT films usually show non-metallic behavior in the temperature range 4-300 K corresponding to quasi-two-dimensional charge transport. One the other hand, annealed SWNT films composed of 99% semiconducting SWNTs possess significant conductance, extremely low on/off ratio (less than 100), and a weak temperature dependence of the conductivity as compared to individual SC-SWNTs.

All the phenomena described above indicate the presence of inter-tube tunneling barriers, which dominate the electronic properties of carbon nanotube networks. A simplified picture is that transport occurs along the tube to its end, and then crosses a tube-tube junction. A film below percolation limit has very low inter-tube junction concentration, its electronic properties are more close to individual nanotubes. CNT networks with density below 1.6 tubes/μm^2 (below monolayer) were used to maximize the on/off ratio of the thin film transistor (TFT)

device.[39] As the thickness and density increase, the concentration of these inter-tube junctions increases and the film thickness increases up to the point that the conductivity saturates (at *t* ~50 nm); at this point the film morphology is such that the conductivity is no longer a function of the film thickness. Therefore, in the film with thickness between 5 and 100nm, the junction resistance dominates the overall transport behavior of the SWNT films. Understanding the transport both along each individual CNT and the inter-tube transport will help in understanding the collective transport in such a complex system.

At room temperature, experimental studies of junctions formed from crossed SWNTs or small bundles have shown that semiconducting-semiconducting and metallic-metallic SWNT junctions show excellent tunneling characteristics with lower junction resistance than semiconducting-metallic SWNT junctions, where a Schottky barrier is formed with a height approximately equal to a half the band gap of the semiconducting SWNT(Figure 4.3).[40] Thermal and electrical properties are dominated by inter-tube junctions. Junctions in a film are very complex and all of the junctions are hetero-junctions, because the crossing tubes are likely of different chirality and bandgap.

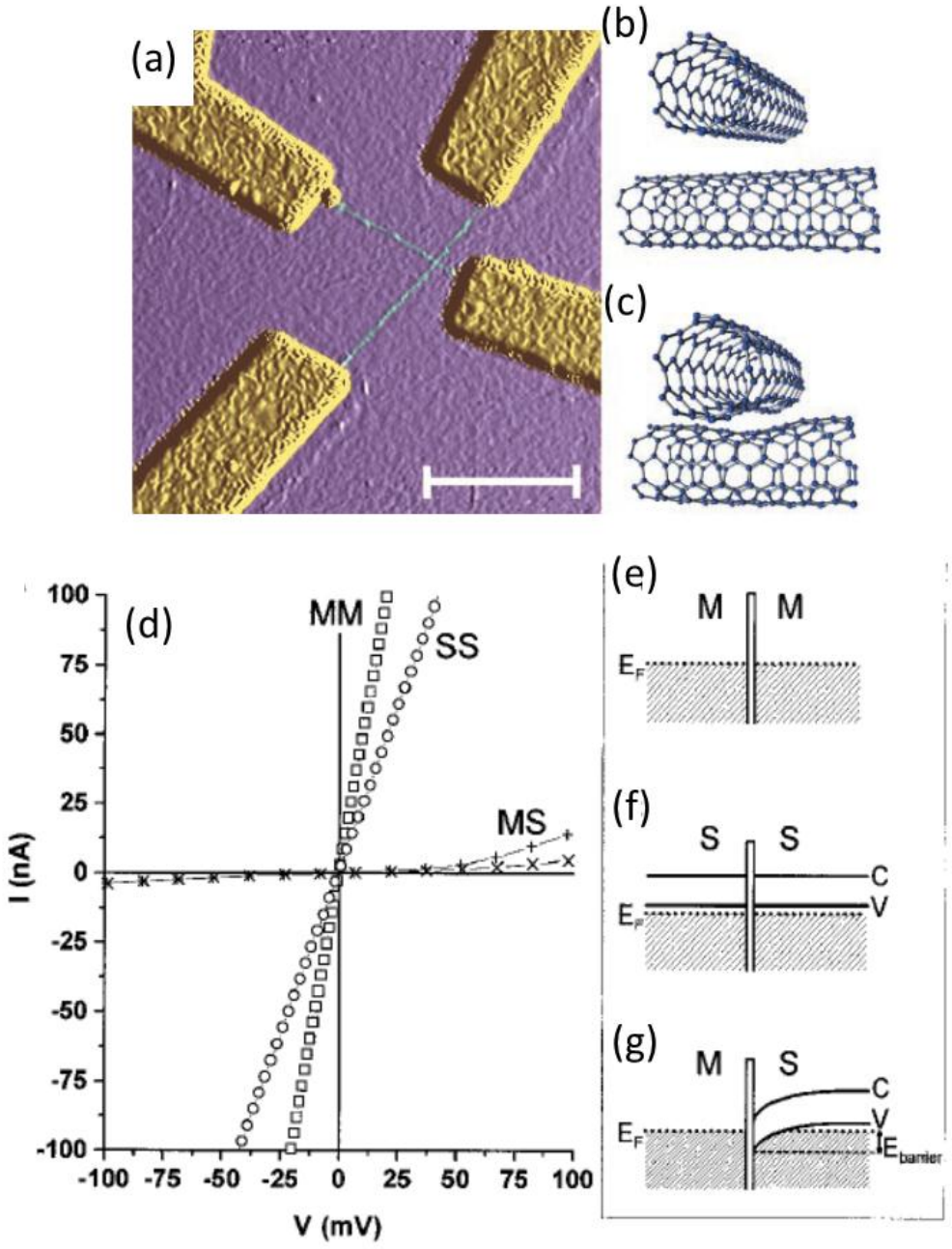

Figure 4.3: (a) Tapping mode AFM image of a crossed SWNT device. Two SWNTs (green) can be seen spanning the Cr/Au electrodes (yellow). (b and c) The structures of a junction between two metallic (5,5) SWNTs. (d) *I-V* characteristics of several SWNT junctions. (e) The band structure of M-M junction. (f) The band structure of S-S junction, (g) The band structure of M-S junction. [40]

Tube-tube junction functionalization or engineering is a fascinating, but least explored topic of the SWNT based electronics; no convincing and practical method was proposed until now to functionalize the junctions. During our research, we find a simple method to reduce the resistance of the junction. In this study, we focus on the effect of metal atoms deposition on the conductivity of SWNT networks. We found, that certain metal atoms, slowly evaporated on the preformed SWNT film, instantly reduce the resistance of the SWNT thin films. We suggest that the first row transition metal atoms are highly mobile and form bis-hexahapto complexes at the SWNT sidewalls, thereby bridging adjacent carbon nanotubes and reducing the inter-nanotube junction resistance.

4.2 Experimental

In this experiment we utilized purified SWNTs produced by the electric arc discharge process of average diameter 1.55±0.1nm and lengths in the range of 1 µm to 5 µm. Three materials with varying ratios of semiconducting to metal metallic (S/M) SWNTs were used: EA-SWNT (P2-SWNT), S/M~67:33, synthesized by our group; IsoNanotubes-M (M-SWNT), S/M~1:99 and IsoNanotubes-S (SC-SWNT), S/M ~99:1, both purchased from NanoIntegris Inc.[33]

The SWNT thin films were prepared by vacuum filtration of a SWNT dispersion in DMF using an alumina membrane disk (0.02µm or 0.2µm pore size, diameter 47mm and 34mm working diameter). The thickness of the SWNT films was controlled by the amount of SWNT material utilized for the vacuum filtration taking into account the working area of the filtration membrane and the SWNT film density of 1.2 g/cm^3; the thickness calibration was obtained by Dektak profilometer on thicker (>100 nm) SWNT films. Films used in this experiment were prepared from a dispersion of 0.010mg of SWNT material in 100 mL of solvent with a resulting thickness of t ~ 8nm; the film was thin enough to expose most of the SWNT bundles to the flux of metal atoms.

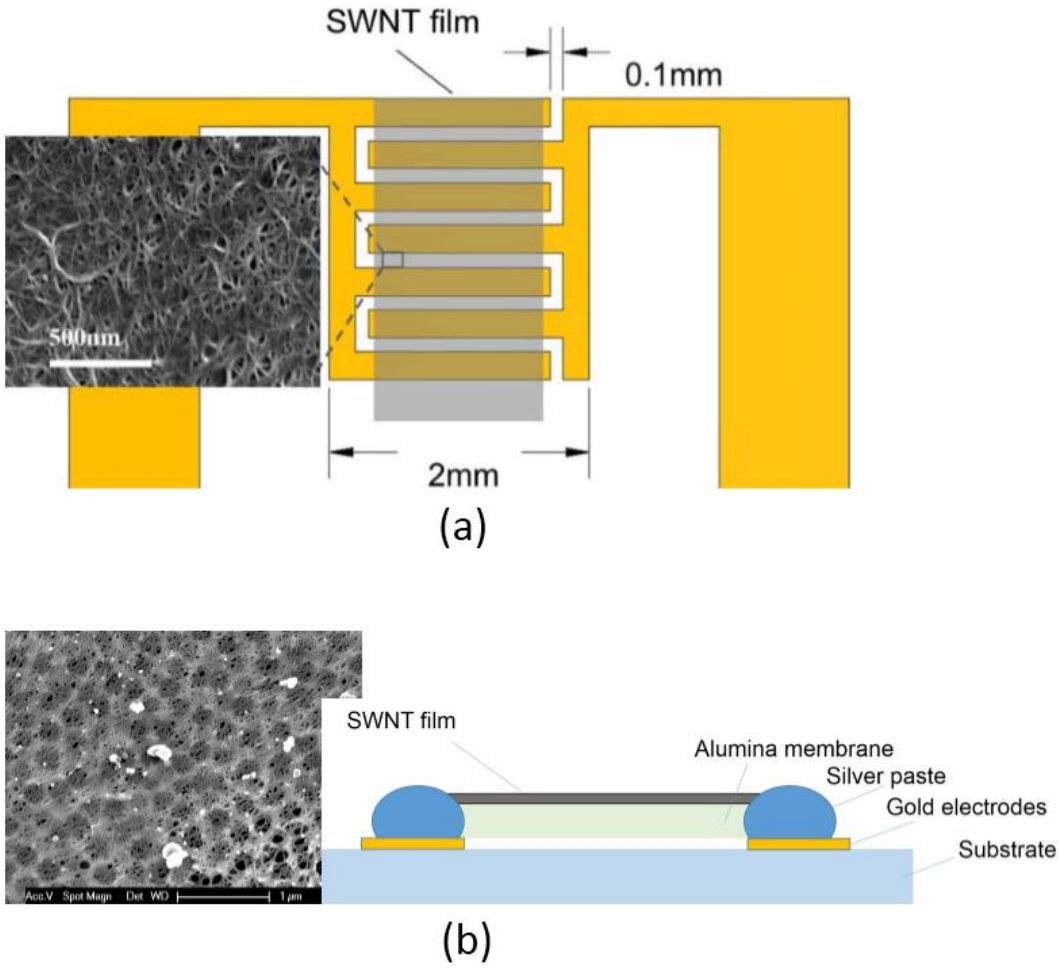

Figure 4.4: (a) Schematic of the SWNT thin film on the interdigitated electrodes together with a SEM image of the representative film. (b) Schematic of the SWNT thin film on the alumina membrane connected to the electrodes together with a SEM image of a representative film.

For the conductivity measurements, we used two device configurations to measure two-probe DC resistance. In the 1st configuration, the rectangular SWNT film fragment of the width ~1.5mm and length ~2mm was separated from the alumina membrane according to the procedure given in the previous chapters and placed on the top of the gold interdigitated electrodes with an electrode

separation of 100 μm as schematically shown in Figure 4.4 (a). In the 2nd configuration, in order to simplify the device fabrication, the SWNT film formed during vacuum filtration on the alumina membrane (Figure 4.4 (b)) was utilized; it was cut into a narrow ribbon of width 1 mm and length 3-4mm using a precision knife with a titanium alloy blade. Here we use silver paste to electrically connect the SWNT film to the electrodes instead of peeling it off and transferring to the substrate with pre-patterned electrodes. The data shown in this chapter are taken utilizing the first electrodes geometry if not specified.

Each substrate contained four independent sets of interdigitated electrodes: three sets were utilized to support identical SWNT channels (SWNT films on interdigitated electrodes or SWNT films on a membrane), and the remaining interdigitated pattern was left blank to be exposed to direct metal deposition in order to evaluate the contribution of the deposited metal film to the total conductance.

The in-situ resistance measurements were conducted in the Temescal BJD 1800 e-beam evaporation chamber (Technical Engineering Services, Inc., Santa Cruz, CA, USA) at a base pressure of 10^{-6} Torr. An electrical measurement stage was built into the e-beam evaporation chamber, which was connected to a data acquisition system outside the chamber with multi-pin electrical feedthrough. The growth of the metal film was monitored during the deposition by utilizing a quartz crystal micro-balance. The metals were deposited at a rate of 0.02-0.03 nm/s during which the electrical resistance of channel was continuously

monitored as a function of time utilizing a multichannel Keithley 2700 data acquisition system (Keithley Instruments, Inc., Cleveland, OH, USA). Usually, the substrates with the SWNT films were annealed at 350 ^{o}C for 2 h in a vacuum of 10^{-7} torr and immediately transferred into the chamber for the metal deposition; a second annealing was conducted inside the e-beam evaporator prior to the metal deposition by IR radiation lamps in the chamber.

4.3 Results and discussion

4.3.1 Typical conductance change of channels during metal deposition

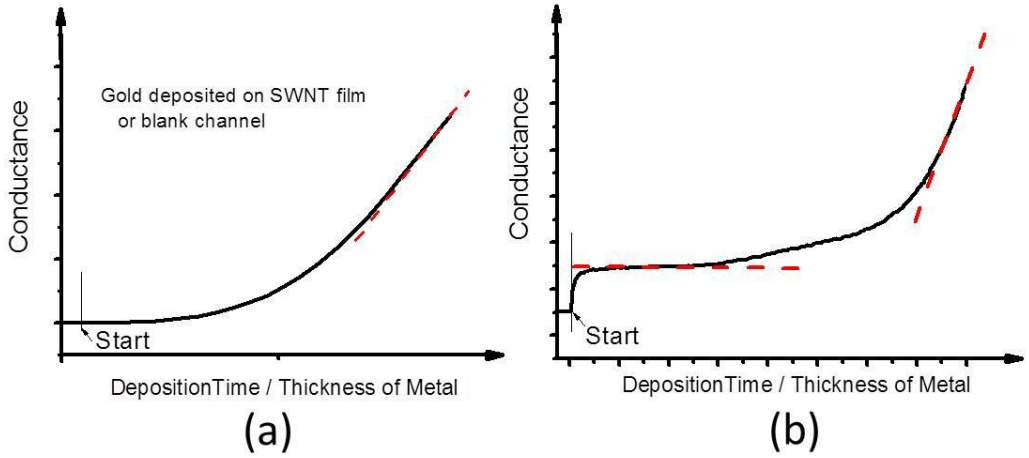

Figure 4.5: Schematic of conductance as a function of duration of metal deposition or thickness of metal deposited on to channel. (a) Deposition of gold atoms to SWNT film or blank channel. (b) Deposition of chromium (Cr) atoms to SWNT films.

It is understandable that the metal atoms deposited on the SWNT film would enhance the film conductance. Figure 4.5 shows the schematic of conductance as a function of duration of metal deposition or thickness of metal deposited on to the channel. During gold deposition onto blank channel or SWNT films, it may be seen in Figure 4.5 (a), that the onset of gold deposition does not induce a pronounced change in the value of the conductance. As more gold atoms are deposited, the conductance starts to increase rapidly. As the gold deposition progresses, the conductance increases linearly with metal thickness. The observed conductance change during gold deposition can be explained by percolation theory. Before the thickness of metal atom reaches the percolation

threshold, the deposited metal clusters do not form interconnecting conducting channels. When the thickness of the metal is in the vicinity of percolation threshold, the conductivity change shows rapid and nonlinear features. After the formation of a continuous metal film, the conductance increases linearly with metal film thickness, and the conductivity is relatively invariant to further increase of the film thickness corresponding to the bulk gold film behavior.

During transition metal deposition, the SWNT channel shows a different behavior. The conductance of the SWNT film increased significantly almost immediately after the commencement of the Cr deposition as shown in Figure 4.5 (b). Beyond initial stage, as the deposition continues, the conductivity shows the same behavior as in case of gold deposition. The initial significant change of the resistance corresponds to a very small amount of Cr atoms, much less than it would be required for the formation of a continuous metal film. This indicates that there is a special interaction between the metals and the graphitic surfaces of the carbon nanotubes.

We studied the interaction between metals and the graphitic surfaces of SWNTs by slowly evaporating small amounts of metal atoms onto SWNT thin films (thickness t ~ 8nm) while measuring in situ the resistance of the SWNT thin films. In order to exclude the contribution of parallel conductance of a continuous metal film, we halted the deposition before the formation of a continuous metal film.

4.3.2 Conductance change of SC-SWNT films during metal deposition

Figure 4.6 shows the conducivity of SC-SWNT films as a function of the duration of metal deposition of Li, Cr and Au.

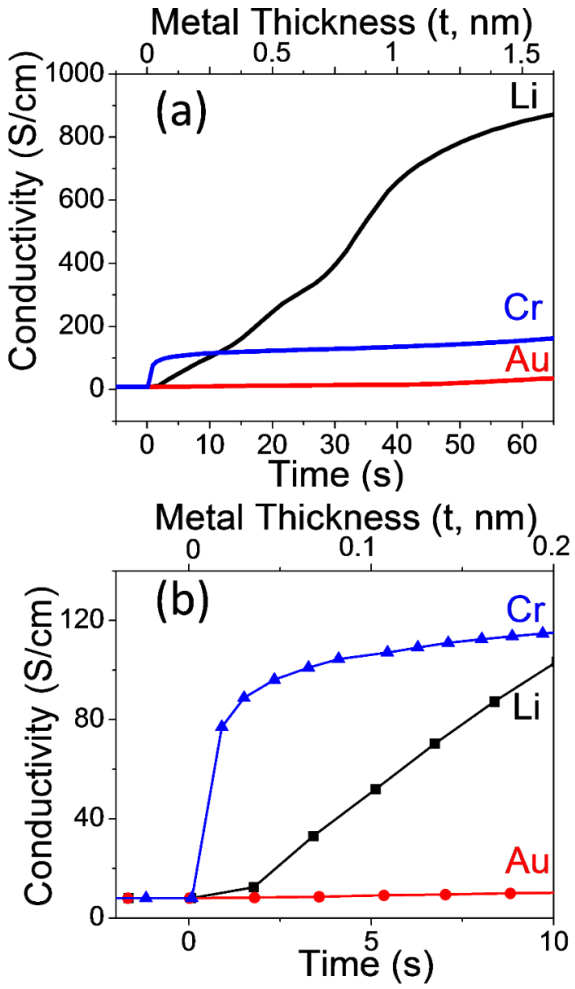

Figure 4.6: Conductivity of SC-SWNT films (t = 8nm), as a function of the duration of metal deposition of Li, Cr, and Au.

From the results, we can distinguish three modes of interaction between metals and the graphitic surfaces of carbon nanomaterials: (a) weak

physisorption (Au), in which there is minimal interaction between the metal and the graphitic surface; (b) ionic chemisorption (Li), in which there is charge transfer to the graphitic structure and preservation of the conjugation and band structure; (c) covalent chemisorption (Cr) with formation of bis-hexahapto-metal bonds, such as those in (η^6-SWNT)Cr((η^6-SWNT), interconnecting adjacent graphitic surfaces and significantly reducing the inter-tube junction resistance in the SWNT networks. It should be noted that this latter mode of interaction is entirely distinct from covalent chemisorption with strong rehybriization of the graphitic surface which brings about a drastic change in the band structure. [41] For example, the reaction of graphitic surfaces with aryl radicals brings about the complete rehybridization of the carbon atoms from sp^2 to sp^3, and leads to the removal of these carbon atoms from the band structure of the remaining graphitic structure. [42, 43]

The conductivity change of the SWNT film resulted from gold deposition is very weak, despite the fact that the bulk electrical conductivity of gold is about six times greater than that of Cr and Li. The resistance change of the SWNT film resulting from Li deposition is strong with the conductance increasing by a factor of over 100 at a Li film thickness, $t \approx 1.2$ nm. In contrast, a strong and instant conductivity enhancement of the SWNT film during Cr deposition can be observed as shown in Figure 4.6 (b). The amount of Cr needed to achieve such an increase was extremely small: the deposition of less than 0.05 nm of Cr resulted in an increase of the conductivity of the SC-SWNT film by more than one

order of magnitude, whereas 0.05 nm of Li resulted in a relatively small change in the SC-SWNT film conductivity. The stoichiometric composition of the SWNT-metal system (MC_x) may be obtained from the relationship:

$$x = \frac{t_C \times d_C \times AW_M}{t_M \times d_M \times AW_C} \quad (4.2)$$

where t is the thickness (nm), d is the density, AW is the atomic weight, M refers to the metal, C refers to SWNT carbon atoms. The stoichiometry (MC_x) at the point where the films attained their maximum conductance were determined to be: t_M = 1.2 nm for Li, giving a value of x ~ 8 (LiC_8), whereas for Cr the upper limit was reached at t_M <0.05nm, which gives x > 180 (1 Cr atom per 180 carbon atoms).

We also monitoedr the blank channel in parallel with the test structures, and during the metal deposition we found that the direct Li deposition on the blank channel does not lead to a measurable conductance (R > 100 Mohm). When the blank channel was exposed to the deposition of Cr or Au, the measured resistance maintained values of R > 10 Mohm with metal thickness, t <1.5nm, which is 100 times higher than the starting resistance of the SC-SWNT film. In the case of Au deposition, it is likely that the small conductivity increase observed in the SC-SWNT film could be explained by the parallel conductance of the continuous Au film. More complex mechanisms must be invoked in the case of Cr and Li deposition.

We also studied the response of the conductivities of the SC-SWNT films to the deposition of other first row transition metals (Ti, V, Cr, Mn and Fe)

immediately adjacent to Cr in the periodic table (Figure 4.7 (a)). The results show similar behavior to that of Cr. Effects of metal atom deposition on the conductivity of SWNT films are summarized in Figure 4.7 (b).

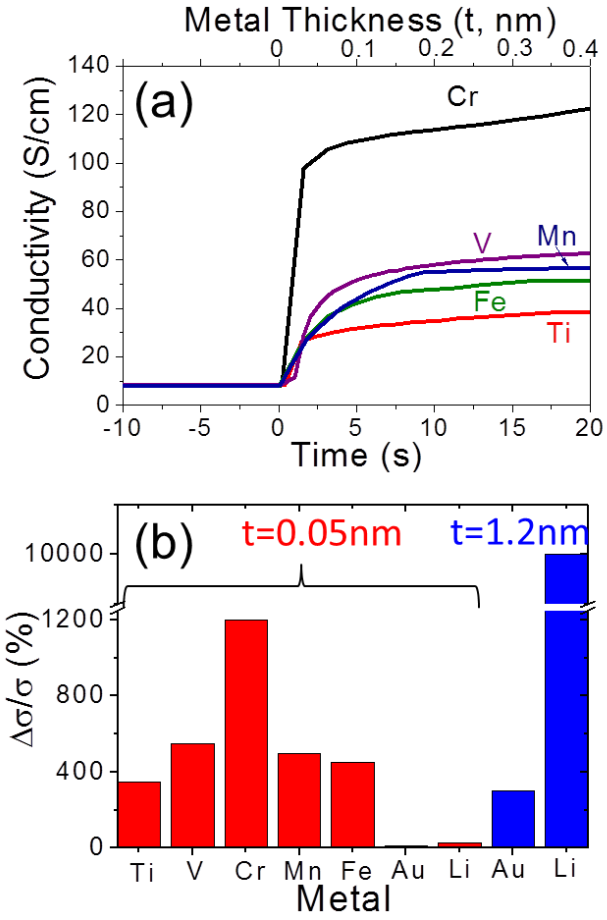

Figure 4.7: (a) Conductivity of SWNT films as a function of the duration of metal deposition of Ti, V, Cr, Mn, and Fe. (b) Effect of metal atom deposition on the conductivity of SWNT films.

4.3.3 Model

We developed a model of the SWNT metal bond formation schematically shown in Figure 4.8 and Figure 4.10. As I describe early in this chapter, the SWNT films consist of a network of individual semiconducting SWNTs and SWNT bundles, and the overall film resistance is composed of the resistance of the individual semiconducting SWNTs and the highly resistive intertube nanotube junctions. Thus, the resistance drop of the SC-SWNT films can be induced either by variations in the resistance of the individual SC-SWNTs or by changes of the resistance of the inter-nanotube junctions.

The response of the conductivity of graphitic materials such as fullerenes, CNTs, and graphene to metal deposition is usually explained by a change in the carrier concentration as a result of charge transfer processes (doping). [27, 44, 45] In the case of Li deposition, the observed maximal conductivity is observed at a stoichiometry LiC_8 similar to the known case of KC_8 in the graphite intercalation compounds. Thus we conclude that the conductivity increase observed in the SC-SWNT film during Li deposition is explained by the charge transfer doping of the SC-SWNT film (Figure 4.8).

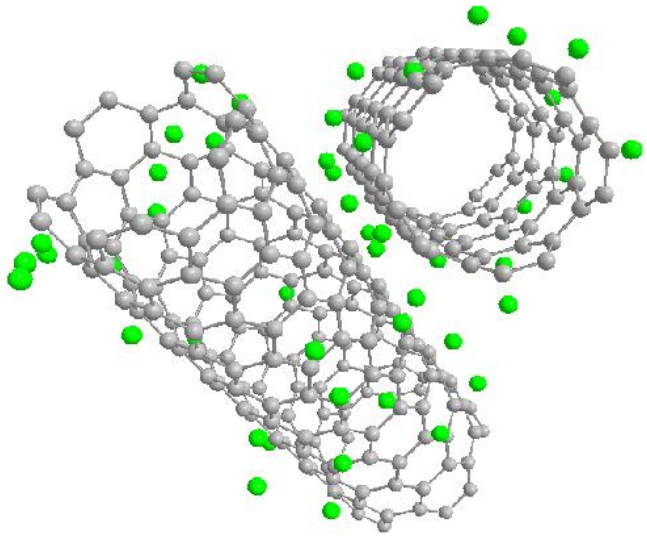

Figure 4.8: Electron transfer processes (doping): Li atoms (green) donate electrons to the conduction bands of the SWNTs.

In the case of Cr deposition, the conductivity increase is unlikely to be due to the charge transfer process, because the maximum conductivity is achieved at a metal to carbon ratio that is too small to be explained by the doping. Instead, the increase in the SWNT network conductance by Cr may arise from the reduction of the intertube junction resistance. The first row transition metals are known to be mobile on conjugated carbon surfaces and offer a range of organometallic chemistries.[46-56] It is known that the atoms of the first row transition metals migrate readily between benzenoid hexahapto complexation sites at room temperature, and the van der Waals gap of 3.15 Å within SWNT bundles [57] is a good fit for a first row transition metal atom; for example, the separation between benzene rings in (η^6-benzene)$_2$Cr is known to be 3.226 Å (Figure 4.9).[52, 58] It is likely that the highly mobile chromium atoms are able to

diffuse along the graphitic surfaces until they encounter a SWNT-SWNT junction or intra-bundle contact with a geometry that allows a formation of a bis-hexahapto-metal bond (Figure 4.10). Thus we propose, that the (η^6-SWNT)$_2$Cr complexes are effective in reducing the conductivity of SWNT films.

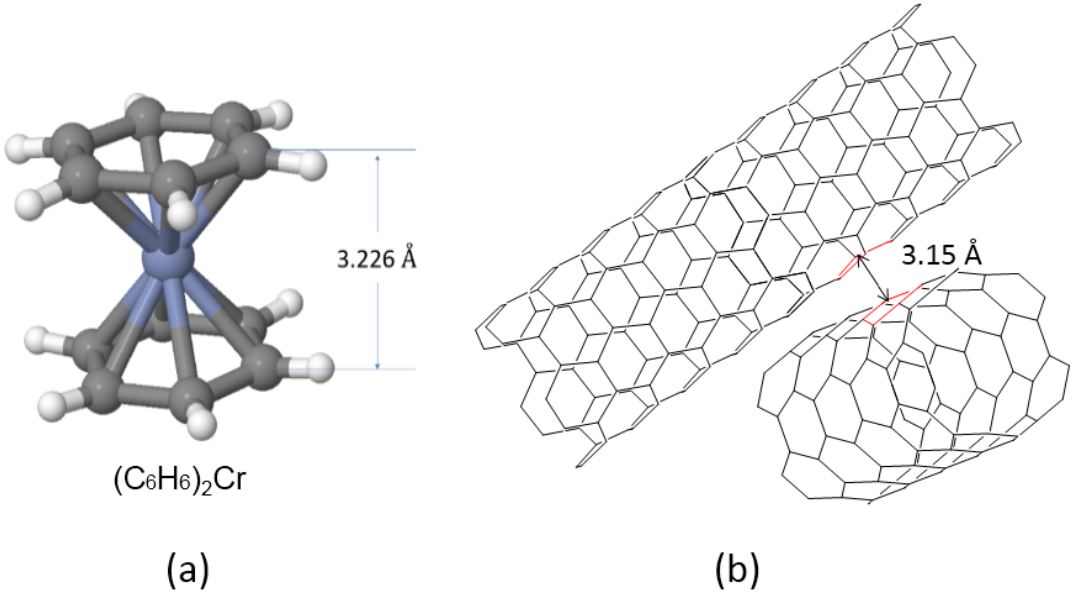

Figure 4.9: (a) Schematic of (η^6-benzene)$_2$Cr where the separation between benzene rings in (η^6-benzene)$_2$Cr is known to be 3.226 Å. (b) SWNT-SWNT junction with van der Waals gap of 3.15 Å.

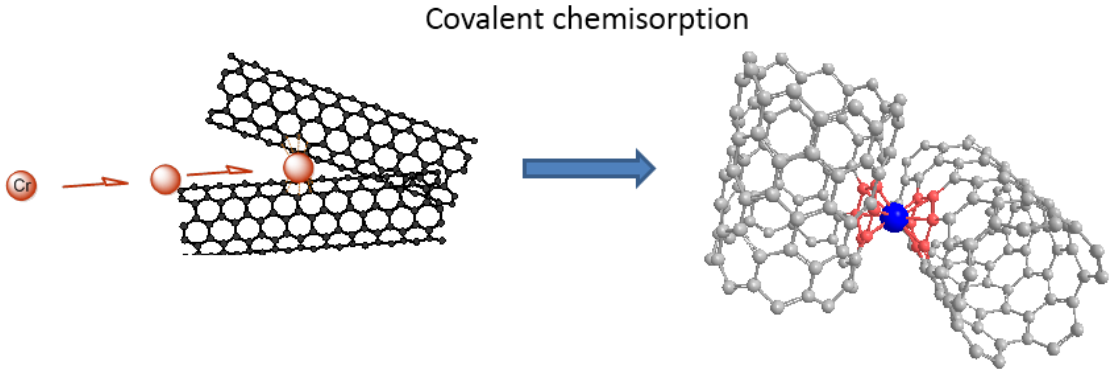

Figure 4.10: Cr atoms form bis-hexahapto complexes at the SWNT sidewalls thereby bridging adjacent carbon nanotubes and reducing the inter-nanotube junction resistance.

Other transition metals (M = Ti, V, Cr, Mn and Fe) also spontaneously form $(\eta^6\text{-}C_6H_6)_2M$ complexes by low temperature metal vapor synthesis (MVS), [50], and thus we conclude that they are appropriate precursors for inter-carbon nanotube junction formation because they exhibit the same sharp increase in conductivity that was found in the case of chromium.

4.3.4 Conductance change of P2-SWNT films during metal deposition

The response of the conductivities of the P2-SWNT films (33:67 mixture of metal and semiconducting SWNTs) to the deposition of the first row transition metals (M = Ti, V, Cr, Mn and Fe) is presented in Figure 4.11. It may be seen that the films exhibit the same sharp increase in conductivity that was shown in the case of SC-SWNT thin film. The effect of metal atom deposition on the conductivity of the SWNT thin films decreases in the order: Cr > V>Fe>Mn, Ti.

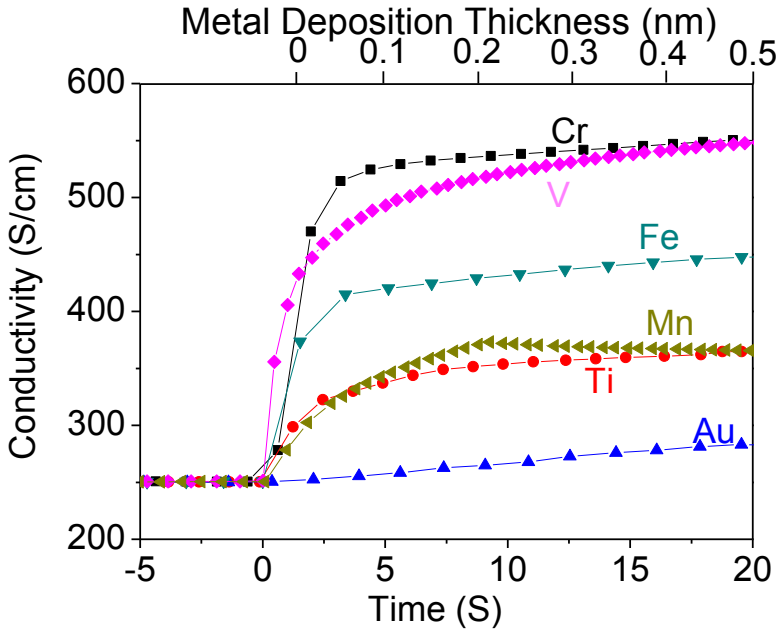

Figure 4.11: Conductivity of P2-SWNT films as a function of the duration of metal deposition.

4.3.5 Conductance change of M-SWNT films during metal deposition

The response of the conductivities of the metallic SWNT films to the deposition of first row transition metals and Li is given in Figure 4.12. The data are collected utilizing SWNT films supported by the alumina membrane without being transferred to the interdigitated electrodes. It may be seen that the data exhibit the same sharp increase in conductivity during Cr deposition as for semiconducting SWNT films which can also be explained by the formation of the bis-hexahapto complexes at the intertube junctions. Interestingly, the deposition of Li resulted in an increase of the conductivity of the M-SWNT. It is possible that Li deposition not only changes the carrier density in the van Hove singularities of semiconducting SWNTs, but also modifies the carriers density in the first van Hove singularity of the metallic SWNTs. Depletion of the first singularity in metallic SWNTs results in the loss of the associated M_{11} absorption intensity, which was observed in the electrical doping of P2-SWNT films in Chapter 3 shown in Figure 2.13(c).

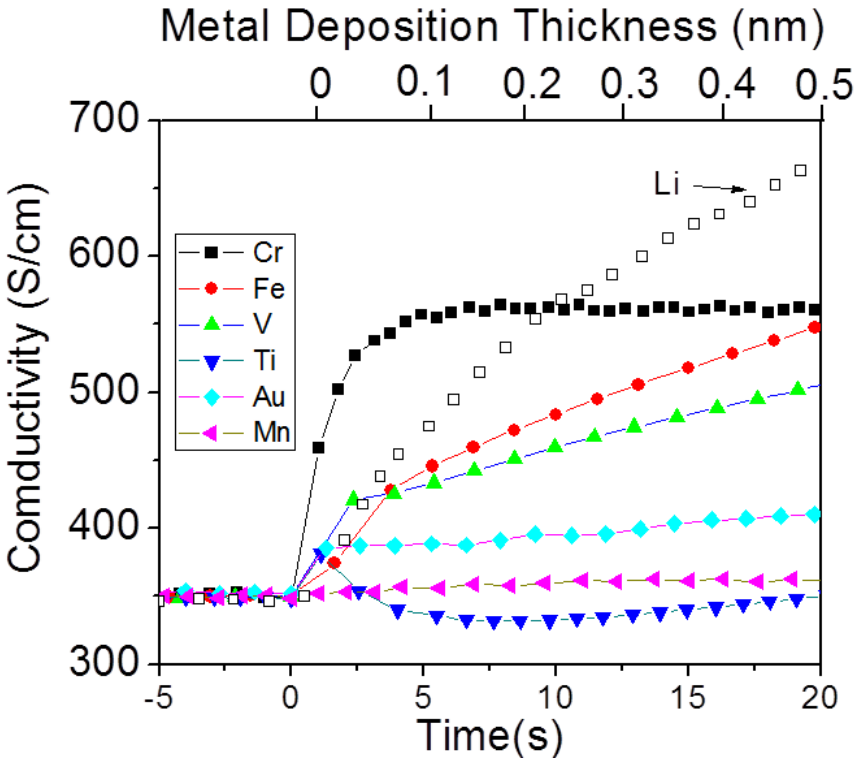

Figure 4.12: Conductivity of M-SWNT films as a function of the duration of metal deposition.

4.3.6 Orbital interaction diagram

As can be seen in the data obtained for all types of SWNT films (P2, Metallic and Semiconducting), the effect of Cr atom deposition on the conductivity of the SWNT thin films is much stronger than for other transitions metals. The orbital interaction diagram for $(\eta^6\text{-}C_6H_6)_2Cr$ is presented in Figure 4.13. It assumes that the relevant SWNT orbitals transform in the same manner

as the benzene π -orbitals.[41, 59] Clearly, Cr is associated with the stable 18 valence electron count discussed above, but V and Ti will have missing electrons from the HOMO in the diagram, whereas Mn and Fe will possess extra electrons residing in the LUMO. Thus, we conclude that the optimum electronic structure of the bridging complex for inter-carbon nanotube junctions obeys the familiar 18-electron rule of organometallic chemistry.[59]

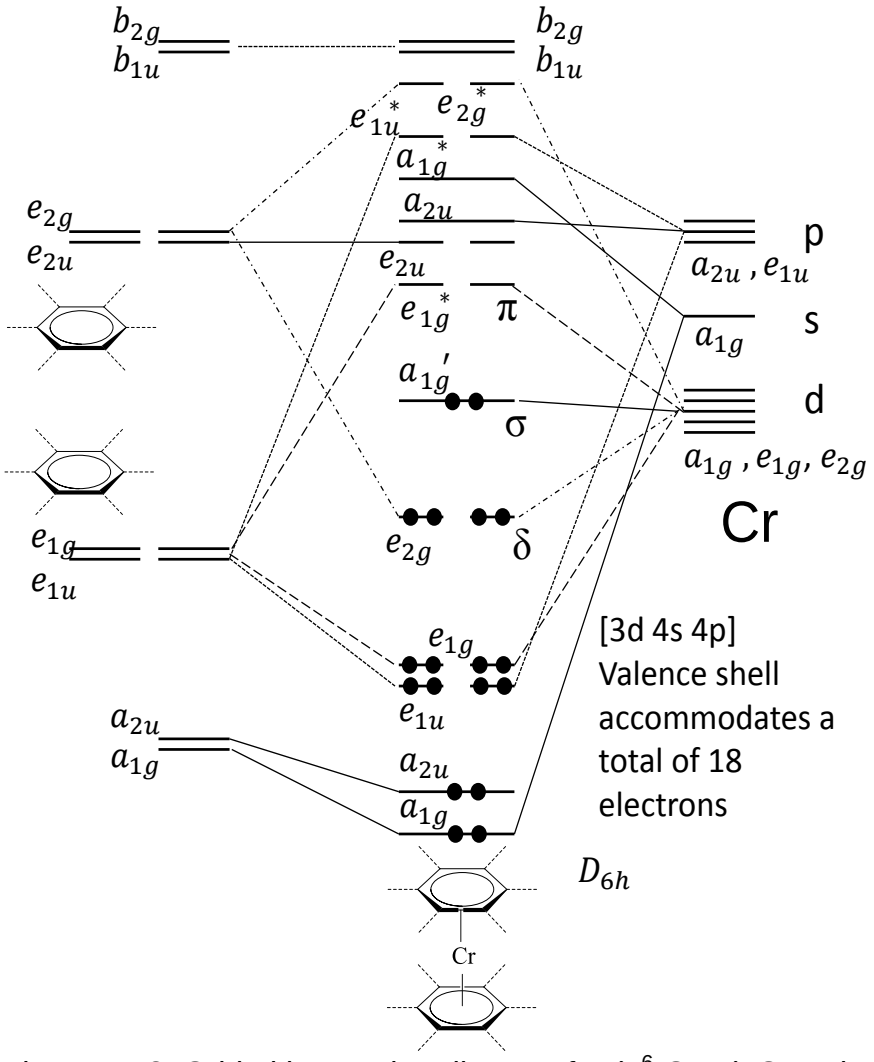

Figure 4.13: Orbital interaction diagram for (η^6-$C_6H_6)_2$Cr. Adapted from Ref. 59.

4.3.7 Three mechanisms of enhancement conductivity in SWNT films

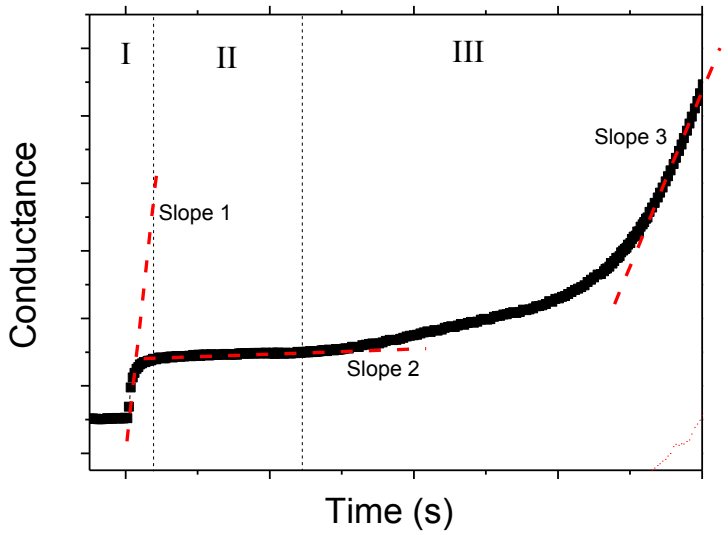

Figure 4.14: Schematic of conductance as a function of duration of metal deposition or thickness of metal deposited on to SWNT thin film.

In summary, I discussed three mechanisms that lead to an increase of conductivity in SWNT thin films during metal deposition: (a) formation of a non-interacting metal film conducting channel formed on the top of the SWNT film and resulting in monotonic conductivity increase; (b) ionic chemisorption of alkali metals strongly increasing conductivity due to charge transfer to SWNTs;(c) chemisorption of the first row transition metals leading to the abrupt change in conductivity due to formation of (η^6-SWNT)M(η^6-SWNT) interconnects.

During the deposition of an arbitrary metal, three mechanisms of interaction between metals and the graphitic surfaces of carbon nanotube may contribute simultaneously. In order to evaluate the effect of each mechanism, I divide the curve of conductance as a function of duration of metal deposition into

three regions shown in Figure 4.14. In the first region, there is an abrupt increase in conductivity. Since small amount of metal atoms would result in a very limited change in film conductivity due to charge transfer and continuous metal film cannot be formed in this region, the covalent chemisorption with formation of the organometallic hexahapto-metal bonds dominates the change of conductivity, whose effect can be indicated by slope 1. In the second region, the linear increase of the conductance is mainly due to the chemical doping, and the strength of the charger transfer can be evaluated by slope 2. In the part III, the change of conductivity is due to the formation of the continuous metal film. After the formation of the continuous metal film, the slope 3 is proportional to the conductivity of the bulk metal and is relatively invariant to further increases of the metal deposition thickness. By comparing the slope1, slope 2 and slope 3, we can evaluate the effect of each mechanism. For example, in case of Cr deposition, the slope1 >>slope2, indicating that the conductivity change during Cr deposition is due to the covalent chemisorption with formation of an organometallic hexahapto-metal bond. During the deposition of Li, there is no part III, indicating no Li metal film can be formed because of the oxidation of Li under the conditions of the experiment.

4.4 Summary

In conclusion, we studied the conductivity of SWNT films as a function of the exposure to the controlled e-beam evaporation of a range of metals, and we were able to identify three distinct mechanisms for the observed conductivity enhancement: (1) physisorption (Au), which leads to the formation of a parallel conducting film, (2) ionic chemisorption (Li), leading to the charge transfer doping of the SWNT film, and (3) covalent chemisorption (Ti, V, Cr, Mn, and Fe), in which there is constructive rehybridization that preserves the graphitic band structure and leads to the formation of conductive carbon nanotube interconnects via bis-hexahapto bond formation. For this latter mode of interaction, we delineated the effect of the occupancy of the transition metal valence shell on the efficiency of the SC-SWNT interconnects and found that Cr (6 valence electrons) deposition results in the highest conductivities in agreement with stability arguments from organometallic chemistry based on the 18-electron valence shell principle. The present results provide a new approach to the application of covalent bond formation to the modification of the transport properties of graphitic structures, which unlike previous doping techniques, leads to an enhancement in the conductivity by increasing the dimensionality of the electronic structure. This research would help to guide optimization of transparent conducting SWNT films and development of thin film based electronics.

References:

1. Tans, S. J., Verschueren, R. M. & Dekker, C. Room Temperature Transistor Based on a Single Carbon Nanotube. Nature 393, 49-52 (1998).
2. Martel, R., Schmidt, T., Shea, H. R., Hertel, T. & Avouris, P. Single- and Multi-Wall Carbon Nanotube Field-Effect Transistors. Appl. Phys. Lett 73, 2447-9 (1998).
3. Dai, H. Carbon Nanotubes: Synthesis, Integration, and Properties. Acc. Chem. Res. 35, 1035-1044 (2002).
4. Avouris, P., Appenzeller, J., Martel, R. & Wind, S. J. Carbon Nanotube Electronics. Proc. IEEE. 91, 1772-1784 (2003).
5. Avouris, P., Chen, Z. & Perebeinos, V. Carbon-Based Electronics. Nat. Nanotechnol. 2, 605-615 (2007).
6. Das, R. N., Liu, B., Reynolds, J. R. & Rinzler, A. G. Engineered Macroporosity in Single-Wall Carbon Nanotube Films. Nano Letters 9, 677-683 (2009).
7. Kamaras, K. et al. Wide-Range Optical Spectra of Carbon Nanotubes: a Comparative Study. Physica Status Solidi B: Solid State Physics 245, 2229-2232 (2008).
8. Borondics, F. et al. Charge Dynamics in Transparent Single-Walled Carbon Nanotube Films from Optical Transmission Measurements. Phys Rev. B 74, 045431 (2006).
9. Bekyarova, E. et al. Electronic Properties of Single-Walled Carbon Nanotube Networks. J. Am. Chem. Soc. 127, 5990-5995 (2005).
10. Wu, Z. et al. Transparent, Conductive Carbon Nanotube Films. Science 305, 1273-1276 (2004).
11. Kaempgen, M., Duesberg, G. S. & Roth, S. Transparent Carbon Nanotube Coating. Appl. Surf. Sci. 252, 425-429 (2005).
12. Hu, L., Hecht, D. S. & Gruner, G. Percolation in Transparent and Conducting Carbon Nanotube Networks. Nano Lett. 4, 2513-2517 (2004).
13. Zhang, D. et al. Transparent, Conductive, and Flexible Carbon Nanotube Films and Their Applications in Organic Light-Emitting Diodes. Nano Lett. 6, 1880-1886 (2006).
14. Green, A. A. & Hersam, M. C. Colored Semitransparent Conductive Coatings Consisting of Monodisperse Metallic Single-Walled Carbon Nanotubes. Nano Lett. 8, 1417-1422 (2008).
15. Kaempgen, M., Chan, C. K., Ma, J., Cui, Y. & Gruner, G. Printable Thin Film Supercapacitors Using Single-Walled Carbon Nanotubes. Nano Lett. 9, 1872-1876 (2009).
16. Artukovic, E., Kaempgen, M., Hetch, D. S., Roth, S. & Gruner, G. Transparent and Flexible Carbon Nanotube Transistors. Nano Lett. 5, 757-760 (2005).

17. Cao, Q. et al. Highly Bendable, Transparent Thin-Film Transistors that use Carbon-Nanotube-Based Conductors and Semiconductors with Elastomeric Dielectrics. Advanced Materials 18, 304-+ (2006).
18. Itkis, M. E., Borondics, F., Yu, A. & Haddon, R. C. Bolometric Infrared Photoresponse of Suspended Single-Walled Carbon Nanotube Films. Science 312, 413-416 (2006).
19. Itkis, M. E., Yu, A. & Haddon, R. C. Single-Walled Carbon Nanotube Thin Film Emitter-Detector Integrated Optoelectronic Device. Nano Lett. 8, 2224-2228 (2008).
20. Ramesh, P., Itkis, M. E., Tang, J. M. & Haddon, R. C. SWNT-MWNT hybrid architecture for proton exchange membrane fuel cell cathodes. J. Phys. Chem. C 112, 9089-9094 (2008).
21. Tang, J. M. et al. High Performance Hydrogen Fuel Cells with Ultralow Pt Loading Carbon Nanotube Thin Film Catalysts. J. Phys. Chem. C 111, 17901-17904 (2007).
22. Tang, J. et al. Carbon Nanotube Free Standing Membrane of Pt/SWNTs as Catalysts Layer in Hydrogen Fuel Cells. Aus. J. Chem. 60, 528-532 (2007).
23. Jha, N., Palanisamy, R., Itkis, M. E. & Haddon, R. C. Construction of a Carbon-Nanotube-Based Fuel Cell Which Exceeds 2015 DOE Targets. ACS Nano submitted (2011).
24. Xie, X. et al. Graphene-Sponges as High-Performance Low-Cost Anodes for Microbial Fuel Cells. Energy & Environ. Sci. 5, 6862-6866 (2012).
25. Xie, X. et al. Nano-Structured Textiles as High-Performance Aqueous Cathodes for Microbial Fuel Cells. Energy & Environ. Sci. 4, 1293-1297 (2011).
26. Xie, X. et al. Three-Dimensional Carbon Nanotube-Textile Anode for High-Performance Microbial Fuel Cells. Nano Lett. 11, 291-296 (2011).
27. Lee, R. S., Kim, H. J., Fischer, J. E., Thess, A. & Smalley, R. E. Conductivity Enhancement in Single-Walled Carbon Nanotube Bundles Doped with K and Br. Nature 388, 255-257 (1997).
28. Jhi, S.-H., Louie, S. G. & Cohen, M. L. Electronic properties of Oxidized Carbon nanotubes. Phys. Rev. Lett 85, 1710-1713 (2000).
29. Banerjee, S., Hemraj-Benny, T. & Wong, S. S. Covalent Surface Chemistry of Single-Walled Carbon Nanotubes. Adv. Mater. 17, 17-29 (2005).
30. Hu, L. B., Hecht, D. S. & Gruner, G. Carbon Nanotube Thin Films: Fabrication, Properties, and Applications. Chem. Rev. 110, 5790-5844 (2010).
31. Fischer, J. E. et al. Metallic Resistivity in Crystalline Ropes of Single-Wall Carbon Nanotubes. Phys. Rev. B 55, R4921-R4924 (1997).
32. Hu, H. et al. Sidewall Functionalization of Single-Walled Carbon Nanotubes by Addition of Dichlorocarbene. J. Am. Chem. Soc. 125, 14893-14900 (2003).

33. Arnold, M. S., Green, A. A., Hulvat, J. F., Stupp, S. I. & Hersam, M. C. Sorting carbon nanotubes by electronic structure using density differentiation. Nature Nanotechnology 1, 60-65 (2006).
34. Frank, O., Kavan, L., Green, A. A., Hersam, M. C. & Dunsch, L. In-Situ Vis/NIR Spectroelectrochemistry of Single-Walled Carbon Nanotubes Enriched with (6,5) Tubes. Phys. Stat. Sol. 245, 2239-2242 (2008).
35. Green, A. A., Duch, M. C. & Hersam, M. C. Isolation of Single-Walled Carbon Nanotube Enantiomers by Density Differentiation. Nano Res 2, 69-77 (2009).
36. Hossain, M. Z., Walsh, M. & Hersam, M. C. Scanning Tunneling Microscopy, Spectroscopy, and Nanolithography of Epitaxial graphene Chemically Modified with Aryl Moieties. J. Am. Chem. Soc. 132, 15399-15403 (2010).
37. Gruner, G. Carbon Nanotube Films for Transparent and Plastic Electronics. J. Mater. Chem. 16, 3533-3539 (2006).
38. Xu, H., Anlage, S. M., Hu, L. B. & Gruner, G. Microwave Shielding of Transparent and Conducting Single-Walled Carbon Nanotube Films. Appl. Phys. Lett. 90, 183119 (2007).
39. Hecht, D., Hu, L. & Gruner, G. Conductivity Scaling with Bundle Length and Diameter in Single Walled Carbon Nanotube Network. Appl. Phys. Lett. 89, 133112 (2006).
40. Fuhrer, M. S. et al. Crossed Nanotube Junctions. Science 288, 494-497 (2000).
41. Bekyarova, E. et al. Effect of Covalent Chemistry on the Electronic Structure and Properties of Carbon Nanotubes and Graphene. Acc. Chem. Res. accepted (2012).
42. Niyogi, S. et al. Covalent Chemistry for Graphene Electronics. J. Phys. Chem. Lett. 2, 2487-2498 (2011).
43. Bekyarova, E., Sarkar, S., Niyogi, S., Itkis, M. E. & Haddon, R. C. Advances in the Chemical Modification of Epitaxial Graphene. J. Phys. D: Appl. Phys. 45, 154009 (2012).
44. Kochanski, G. P., Fiory, A. T., Hebard, A. F. & Haddon, R. C. Electrical Resistivity and Stoichiometry of KxC60 Films. Science 255, 184 (1992).
45. Haddon, R. C., Kochanski, G. P., Hebard, A. F., Fiory, A. T. & Morris, R. C. Electrical Resistivity and Stoichiometry of CaxC60 and SrxC60 Films. Science 258, 1636 (1992).
46. Filatov, A. S. & Petrukhina, M. A. Probing the Binding Sites and Coordination Limits of Buckybowls in a Solvent-free Environment: Experimental and Theoretical Assessment. Coord. Chem. Rev. 254, 2234-2246 (2010).
47. Hubig, S. M., Lindeman, S. V. & Kochi, J. K. Charge-Transfer Bonding in Metal-Arene Coordination. Coord. Chem. Rev. 200-202, 831-873 (2000).

48. Bush, B. F., Lynch, V. M. & Lagowski, J. J. Transition-Metal Organometallic Compounds. 8. Arene Exchange Reactions of Bis(naphthalene) chromium. Organometallics 6, 1267-1275 (1987).
49. Bush, B. F. & Lagowski, J. J. Chemistry of Bis(h^6-naphhtalene)chromium Ligand Exchange Reactions: Synthesis and Characterization of Poly[(m-h^6, h^6-naphthalene)chromium] Organometallics 7, 1945-1948 (1988).
50. Pampaloni, G. Aromatic Hydrocarbons as Ligands. Recent Advances in the Synthesis, the Reactivity and the Applications of bis(h^6-arene) Complexes. Coord. Chem. Rev. 254, 402-419 (2010).
51. Kundig, E. P., Perret, C., Spichiger, S. & Bernardinelli, G. Naphthalene Complexes .5. Arene Exchange-Reactions in Naphthalenechromium Complexes. J. Organomet. Chem. 286, 183-200 (1985).
52. Jimenez-Halla, J. O. C., Robles, J. & Sola, M. Coordination of Bis(tricarbonylchromium) Complexes to Small Polycyclic Aromatic Hydrocarbons: Structure, Relative Stabilities, and Bonding. Chem Phys Lett 465, 181-189 (2008).
53. Jimenez-Halla, J. O. C., Robles, J. & Sola, M. Intramolecular Haptotropic Rearrangements of the Tricarbonylchromium Complex in Small Polycyclic Aromatic Hydrocarbons. Organometallics 27, 5230-5240 (2008).
54. Kundig, E. P. Synthesis of Transition Metal h6-Arene Complexes. Topics Organomet. Chem. 7, 3-20 (2004).
55. Pape, A. R., Kaliappan, K. P. & Kundig, E. P. Transition-Metal-Mediated Dearomatization Reactions. Chem. Rev. 100, 2917-2940 (2000).
56. Kundig, E. P. & Timms, P. L. Metal Atom Preparation and Ligand Displacement Reactions of BisnaphthaleneChromium and Related Compounds. J. Chem. Soc. Chem. Commun., 912-913 (1977).
57. Thess, A. et al. Crystalline Ropes of Metallic Carbon Nanotubes. Science 273, 483-487 (1996).
58. Haaland, A. The Molecular Structure of Gaseous Dibenzene Chromium, $(C_6H_6)_2Cr$. Acta Chem. Scand. 19, 4146 (1965).
59. Elschenbroich, C. Organometallics (Wiley-VCH, Weinheim, 2006).

Chapter 5 Electro-Oxidized Epitaxial Graphene and its Optoelectronics Application

5.1 Introduction

Graphene has extraordinary electronic properties that offer charge carrier concentrations up to 10^{13} cm^{-2} and room temperature mobility of $\sim$ 10 000 $cm^{-2}V^{-1}s^{-1}$; [1-3] It is considered as the next generation electronic material that may serve as the successor to silicon in integrated circuits and microelectronic devices.

In graphite, the adjacent graphene layers are bound by weak van der Waals forces. The first graphene sample of micrometer lateral size was obtained from the mechanical exfoliation of graphite using adhesive tapes.[1, 4] However, the exfoliation process cannot make controlled, large-scale graphene. The first method of creating large sheets of graphene was developed in 2004 by researchers in Georgia Tech.[2] Epitaxial graphene (EG) is made by heating silicon carbide wafers in a vacuum so that the silicon was vaporized, leaving behind the carbon layer. The price of epitaxial graphene on SiC is dominated by the substrate price, which is probably too expensive for commercial applications at present time.

Another approach which can employs established industrial processes is chemical vapor deposition (CVD) graphene growth, in which graphene is grown by decomposing methane or hydrocarbon gases on a hot reactive metal surface.[5, 6] Ruthenium, Iridium and Nickel have been used as metal substrates, but later copper was found to give higher quality graphene. Once synthesized,

CVD graphene is transferable to diverse substrates, making this technique adaptable for numerous electronic applications.[7, 8]

At the present moment large-scale solution-based processes are used to produce bulk quantities of small-area graphene flakes for development of structural composites, chemical filters, or battery components.

Another important method is the oxidation of graphite and exfoliation of the resulting graphite oxide with the help of sonication, centrifugation or intercalation by chemicals to form graphene oxide suspension.[9] Chemical reduction or physical reduction (laser), [10] are used to prepare reduced graphene oxide sheets or chemically functionalized graphene.[11-16]. Several alternative methods of directly exfoliating graphite in solution have been developed by using ultrasound or highly specialized solvents such as ionic liquids.

In comparison to other types of graphene, epitaxial graphene stands at the forefront of materials that may be used for large integrated electronics in the semiconductor industry. Epitaxial graphene devices and circuits can be fabricated by processes similar to those employed for silicon-based device manufacture. In addition to promising industrial application, epitaxial graphene on silicon carbide plays an important role in fundamental research and development in academia. For example, the first measurements on graphene monolayers were made on epitaxial graphene;[2] the graphene-electronic band structure was first visualized on EG;[17] and weak anti-localization was observed in this material.[18]

5.1.1 Band gap engineering of graphene

Intrinsic graphene is a 2D semi-metal or zero-gap semiconductor with a tiny overlap between valence and conduction bands. Thus, before graphene can be engineered into transistor or other electronic devices, an energy gap must be introduced into its band structure. Graphene can be rendered semiconducting via energy gaps introduced in a variety of ways, including electrical biasing, nano-patterning, coupling to substrates and chemical modification.

In bi-layer graphene two layers are either rotated relative to each other or superimposed in a graphitic Bernal stacked configurations (the stacking fashion of graphite),[19, 20] and the stacking geometry greatly influences the properties of bilayer graphene. Bi-layer graphene has been shown to have interesting electrical properties; such as on-off conductivity switching by use of a gate electrode.[19-25] Bi-layer graphene is now a promising candidate for optoelectronic and nanoelectronic applications.

Graphene nanoribbons of only a few nanometers in width and atomically smooth edges have been intensively studied both theoretically and experimentally.[26-33] It has been found that the lateral confinement of charge carriers creates an energy gap near the charge neutrality point and the band-gap scales inversely with the ribbon width.[29]

An energy gap can be also introduced by coupling to substrates. For example, an energy gap of ~0.26 eV at the K point in epitaxial graphene has

been reported. It is believed that the origin of this gap is the breaking of sub-lattice symmetry owing to the graphene–substrate interaction.[34]

An elegant approach to band gap opening utilizes the idea of chemically changing the hybridization of carbon atoms from sp^2 into sp^3, thus removing the conducting these p-orbitals from conjugation and from the band structure.[35-38]. A reversible chemical modification was demonstrated by binding hydrogen to graphene and reducing the graphene conductivity by a factor of one-million. [39] The Haddon research group suggested the application of covalent chemistry to modify the electronic and magnetic properties of graphene.[40] The application of nitrophenyl (NP) functionalization to epitaxial graphene (Figure 5.1 (a)) has succeeded in opening a band gap of ~0.4 eV (Figure 5.1 (b))[41, 42] and inducing room temperature ferromagnetism (Figure 5.1 (c)).[43] Nevertheless, the effective tuning of the graphene band gap by chemical routes remains a great challenge.

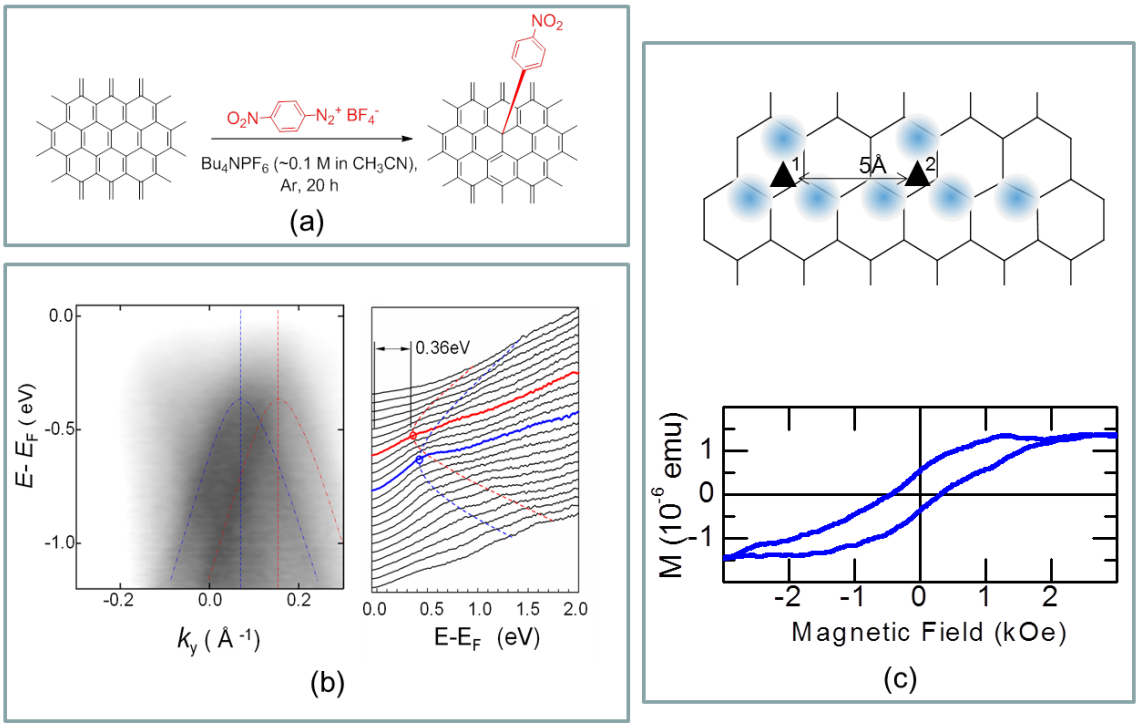

Figure 5.1: (a) Structure of the nitrophenyl (NP) addition products of graphene. (b) Angle-resolved photoelectron emission spectroscopy of NP-functionalized epitaxial graphene showing two diffuse bands highlighted by the dashed lines, corresponding to Dirac cones with a band edge 0.36 eV below the Fermi level, estimated from constant energy cuts.[42] (c) The magnetism of EG due to NP functionalization.[43]

5.1.2 Optoelectronic applications of graphene

2D graphene is now emerging rapidly as one of the leading candidates to replace silicon in high density electronics,[1, 44, 45] but its potential in optoelectronic applications is yet to be explored.

Graphene can form highly transparent conducting films with an absorption of 2.3% per layer in the visible range.[46] With such transparency and high electrical conductivity, graphene is expected to become a replacement for

expensive and brittle indium tin oxide and other ceramic transparent electrode materials as a flexible transparent electrode for applications in organic light-emitting diodes (OLED), photovoltaic cells and touchscreen displays.

Recently, the optical and photo-electronic properties of graphene have attracted significant interest because of the new physics and the potential for photonic applications.[47, 48] Despite the extremely short life time of the photocarriers, the photoconductivity in graphene was detected by using a laser beam focused at the regions adjacent to the metal electrodes where the internal electric field induced by the band bending is able to separate the photogenerated electron-hole pairs before they recombine.[49-52] As a result, an ultrafast graphene photodetection has been demonstrated with an operating bandwidth exceeding 40 GHz, high-speed information transfer of 10 Gbit/s, and a responsivity of 6.1 mA/W at a wavelength of 1.55 um.[47, 48] In a different development, photoconductivity was observed in thin films of graphene produced by reduction of graphene oxide,[14, 53] and was enhanced by attachment of GdSe quantum dots thus giving rise to an extrinsic photoconductivity with responsivity up to 4 mA/W at 532 nm wavelength laser irradiation.[54, 55]

In this chapter, I will discuss the effect of the controlled electrochemical oxidation of epitaxial graphene (EG) in nitric acid on the electronic and optoelectronic properties. We observed electrical conductivity behavior which was ascribed to the scattering of the charge carriers in a two-dimensional

electron gas. In addition, we observed enhanced photoresponsivity of the EG in UV spectral range.

5.2 Experimental

For this work we employed multi-layer EG (6-8 layers) films grown on the C-face of SiC substrates (Cree Inc., 4H SiC) with dimensions 3.5 x 4.5 mm.[2, 44] Two identical isolated macroscopic dog bone shaped EG channels, comprising test and reference channels(Figure 5.2 (a)), with length 1.2 mm and width 0.35 mm were patterned side-by-side on the same wafer with a precision knife with a titanium alloy blade. The electrical contacts to the channels were formed by e-beam evaporation of 10 nm Ti and 100 nm Au layers wired to the outside circuit via indium pads.

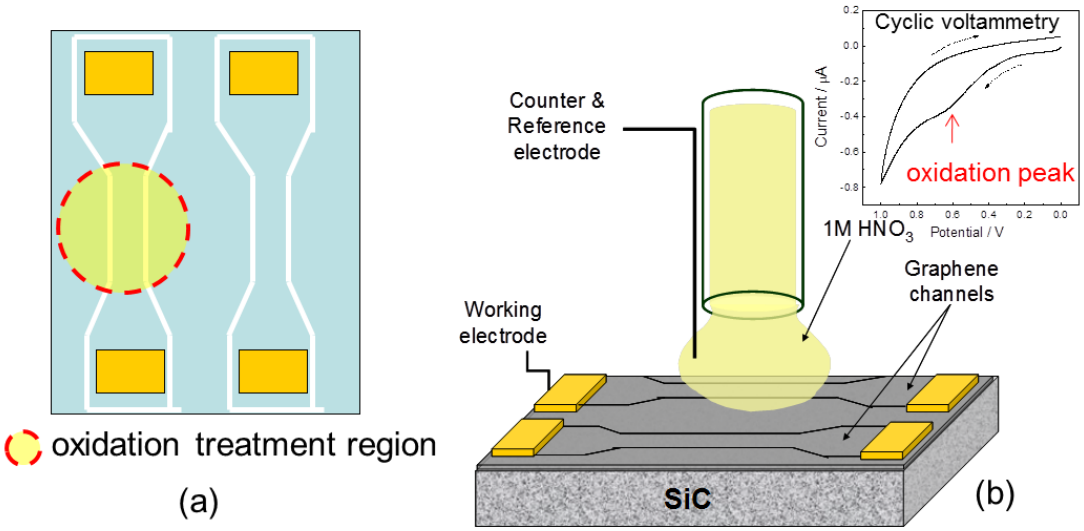

Figure 5.2: (a) Schematic of SiC substrate with two isolated EG channels, oxidation is conducted on one channel, leaving another channel in its pristine state. (b) Schematic illustration of electrochemical oxidation of epitaxial graphene, and cyclic voltammogram of epitaxial graphene electrode in 1 M HNO_3 (inset).

Electrochemical oxidation utilizing 1M nitric acid electrolyte was applied to the test channel (Figure 5.2 (b)): a 1 mm diameter Teflon capillary tube mounted on an *XYZ* translational stage was used to position a drop of the electrolyte (1 M HNO3) on top of the test channel. The electrolyte covers most of electro-oxidation channel without spreading to the gold contacts and reference channel. The Pt wire mounted at the capillary tube and inserted into the electrolyte drop served as a counter/reference electrode, while the surface of the graphene channel was used as the working electrode in the cyclic voltammetry (CV) experiments (Figure 5.2 (b), inset). The typical starting resistance of the pristine EG channel was ~5 kΩ. The resistance of the test channel increases during the electrochemical oxidation; we stopped the controlled electrochemical oxidation when the resistance of the test channel increased by a factor of about 2.

Atomic force microscope (AFM) imaging of the graphene channels was carried out using Dimension 5000 Veeco instrument. Raman spectra were collected with a Nicolet Almega XR Raman microscope using 532 nm laser excitation.

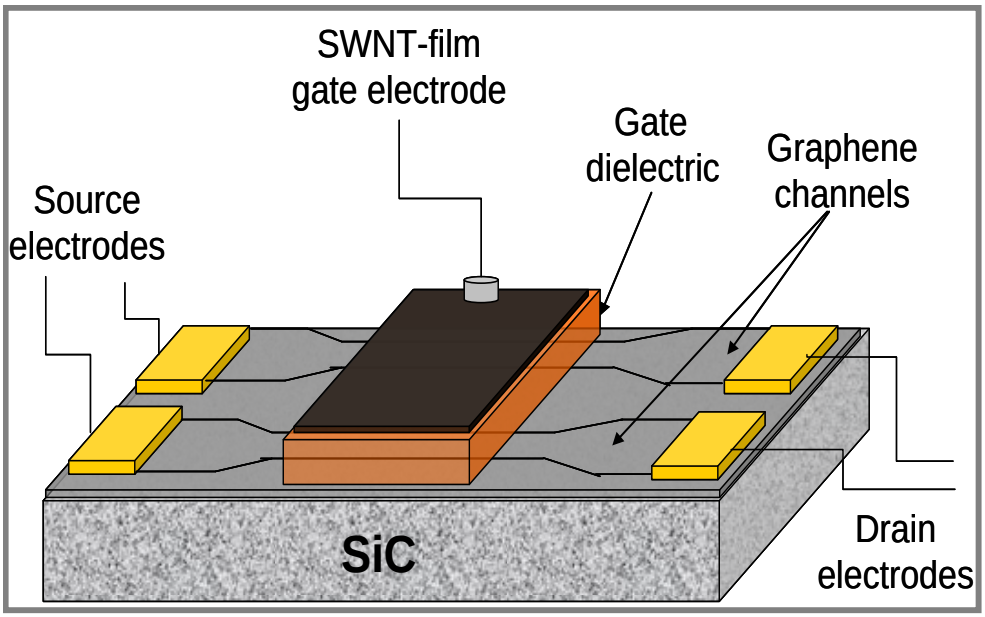

Figure 5.3: Schematic of the EG based FET

In order to further characterize the graphene channels, field effect transistors were prepared on the basis of two parallel EG channels as shown in Figure 5.3. For the large area macroscopic FETs (mm size) utilized in the current study, there is a much higher probability of a device failure due to pinholes in the gate dielectric in comparison with micrometer size devices. We have tested several gate dielectric materials at a variety of thicknesses, and the 1 um thick parylene film by CVD vacuum deposition was chosen to coat the graphene channels as a gate dielectric. The parylene was sublimed at 120 °C at the end of the furnace, cleaved by passing through the pyrolysis zone, which was kept at 650 °C, and polymerized on the epitaxial graphene sample placed at the room temperature region of the reactor tube.[56, 57] To further increase the yield of

functional FETs, we utilized a conducting SWNT thin film as the top gate electrode; the 40 nm thick semitransparent P2-SWNT film was prepared by vacuum filtration and placed on top of the dielectric layer as top gate electrode. The SWNT film functions as an integrated two-dimensional conducting network with in-plane alignment. Compared with the metal top gate fabricated by vapor deposition, the nanotube film suppresses the formation of the pinholes due to the high aspect ratio of the carbon nanotubes. The prepared graphene FET functions well against breakdown for gate voltages up to 110 V under ambient conditions.

5.3 Result and discussion

5.3.1 Effect of electro-oxidation on surface of EG

Figure 5.4 shows AFM image of pristine EG surface and EG at different stages of the electro-oxidation. An AFM image of the pristine sample in Figure 5.4 (a) shows the atomically smooth EG surface overlaid with a pattern of ridges, which is typical for EG grown on SiC substrates.[58, 59] The occurrence of ridges (pleats, folds) of larger dimensions (height, $h \approx 10$ nm) in EG is related to the compressive stress that accompanies the cooling of the wafer after the growth of EG at high temperatures as a result of the difference in the thermal coefficient of expansion of sample and substrate. As the electro-oxidation starts, sp^3 functionalities containing carbon-oxygen bonds are introduced into the graphene surface as point defects that are responsible for the increase in the surface roughness (Figure 5.4 (b)). As the electro-oxidation continues, we observed the initiation of line defects (Figure 5.4 (c)), which propagate along the ridges. In the meantime, electrolyte may access and intercalate into the underlying EG layers through the line defects (Figure 5.4 (d)), and this may provide an additional reaction channel for EG that is not present in other flat carbons such as graphite and exfoliated graphene. During further oxidation, we observed a partial delamination of the graphene layers along these line defects (Figure 5.4 (e)), indicating the interlayer electrolyte intercalation. In some extreme cases, complete delamination can be seen with exposure of the SiC substrate (Figure 5.4 (f)). In present electo-oxidation experiment, the observed line defects along

the ridges are ascribe to the enhanced reactivity originated from local curvature. Local curvatures have been used to explain the enhanced reactivity of the fullerenes[60] and carbon nanotubes[61].

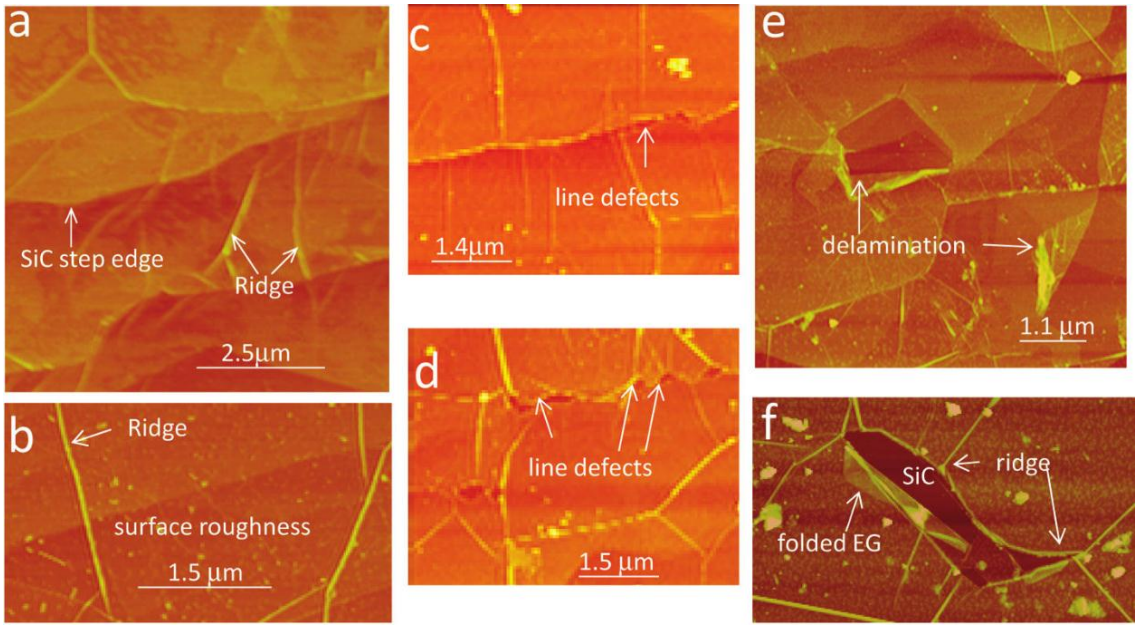

Figure 5.4: AFM images of C face of EG sample at different stages of the electro-oxidation. (a) Pristine EG. (b-e) Transformation of EG surface during the oxidation steps.

Figure 5.5 shows Raman spectra of EG as a function of the electro-oxidation time. The pristine multilayer EG sample shows the prominent G and 2D-band features at frequencies 1581 and 2689 cm^{-1}, respectively (Figure 5.5 (a)). With increasing oxidation time, the intensities of G and 2D bands decrease, and the D band at 1340 cm^{-1}, which originates from the sp^3 carbon centers present as defects in the conjugated sp^2 network, is developed. The resulting

increase of the ratio of intensities of D to G bands (I_D/I_G) with electro-oxidation time (Figure 5.5 (b)) correlates with increasing concentration of the point and line defects and the increasing roughness of the oxidized EG surface observed in AFM images in Figure 5.4. The decreasing intensity of 2D bands with increasing electro-oxidation time (Figure 5.5 (b)) qualitatively indicates the thinning of EG layers and correlates with the increase of the channel resistance.

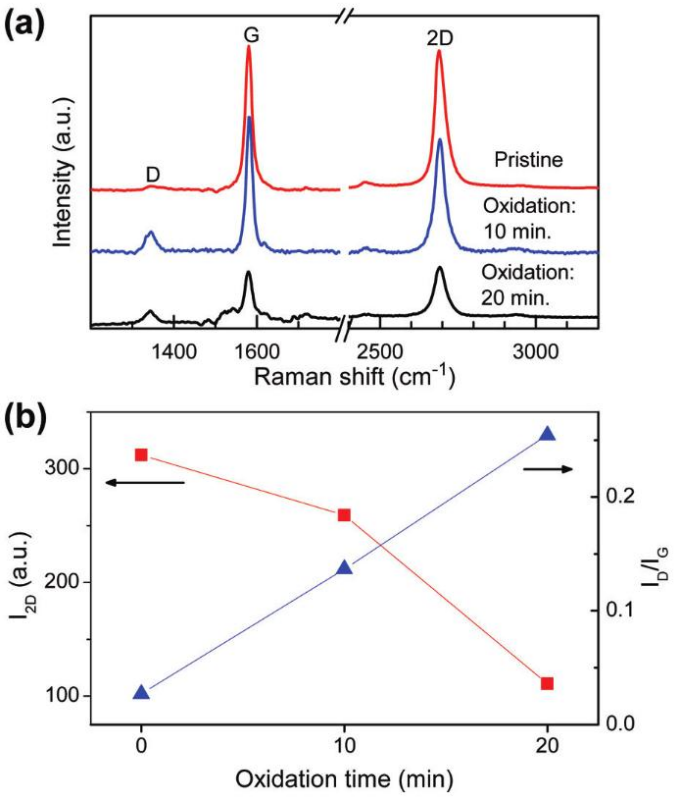

Figure 5.5: (a) Raman spectra of EG-D pristine sample, after 10 min and 20 min electro-oxidation; (b) intensity of 2D-band (red) and D-band to G-band intensities ratio (blue) as a function of electro-oxidation time.

5.3.2 Effect of electro-oxidation on electrical properties of EG

Figure 5.6 presents the temperature dependence of the resistance of the two EG channels before and after controlled electro-oxidation of EG sample. In the initial pristine state, both channels demonstrate weak temperature dependence of the resistance, showing~10% resistance change with temperature decreasing from 360 to 4.2 K. After controlled electro-oxidation (we stopped the electro-oxidation when the resistance of test channel at room temperature increased by a factor of about 2), the temperature dependence of the resistance changed from metallic to nonmetallic over the whole temperature range with a total increase of resistance of ~80% from 360 to 4.2 K (Figure 5.6 (a)). Since there is no electro-oxidation conducted in the reference channel, the temperature dependence remains essentially unchanged (Figure 5.6 (b)).

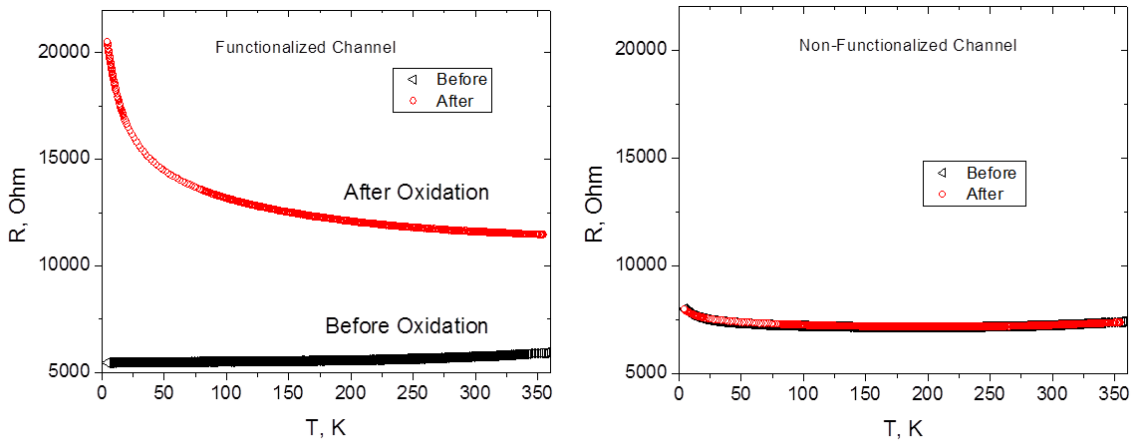

Figure 5.6: Temperature dependences of resistance of graphene channels before and after oxidation. The resistance data were taken before FET fabrication without gating the channels. (a) Test channel. (b) Reference channel.

In order to test if the nonmetallic behavior observed in the electro-oxidized channel is associated with the opening of the energy gap, we present the temperature dependence of resistance data $R(T)$ in the form of an Arrhenius plot shown in Figure 5.7 (a). Intrinsic semiconductor with a well-defined energy gap would show a linear relationship in the Arrhenius plot, and the slope would indicate the size of the energy gap. In contrast, the Arrhenius plot of experimental data shows a variable slope with a temperature dependent activation energy, which changes from 1.9 meV at room temperature to 0.03 meV at helium temperatures, which is much less than the thermal energy [$k_B T$~ 26 meV at 300 K)]. Moreover, resistance of pristine channel shows similar values for the activation energies in Arrhenius plot in the corresponding temperature ranges. Thus, effect of controlled electro-oxidation could not be explained with Arrhenius plot analysis.

The nature of the observed nonmetallic dependence becomes clear when the resistance is plotted as a function of the logarithm of the temperature as shown in Figure 5.7(b). In both pristine and electro-oxidized EG channels, the function $R = R_0 + A \times \ln(T/T_0)$ satisfactorily fits the experimental data over the temperature range from 50 to 5 K. This type of logarithmic temperature dependence was observed in a number of two-dimensional electron gas systems at low temperatures, such as thin metal (AuPd) films, [62], silicon inversion layers,[63] ultrathin Pt films, [64] and indium oxide films.[65] Theoretically, this logarithmic temperature dependence was ascribed to weak localization[66-68] or electron-

electron interactions[69, 70] in two dimensional electron gas systems with some degree of disorder. Thus, the quasi-linear *R* versus ln *T* dependence in both pristine and electro-oxidized EG channels presented in Figure 5.7 (b) indicates that the nonmetallic character of the electrical conductivity originates from scattering in a 2D electronic system with some degree of disorder in EG surface. Chemical functionalization introduces additional scattering centers increasing the degree of disorder, but an energy gap at the Fermi level could not be introduced.

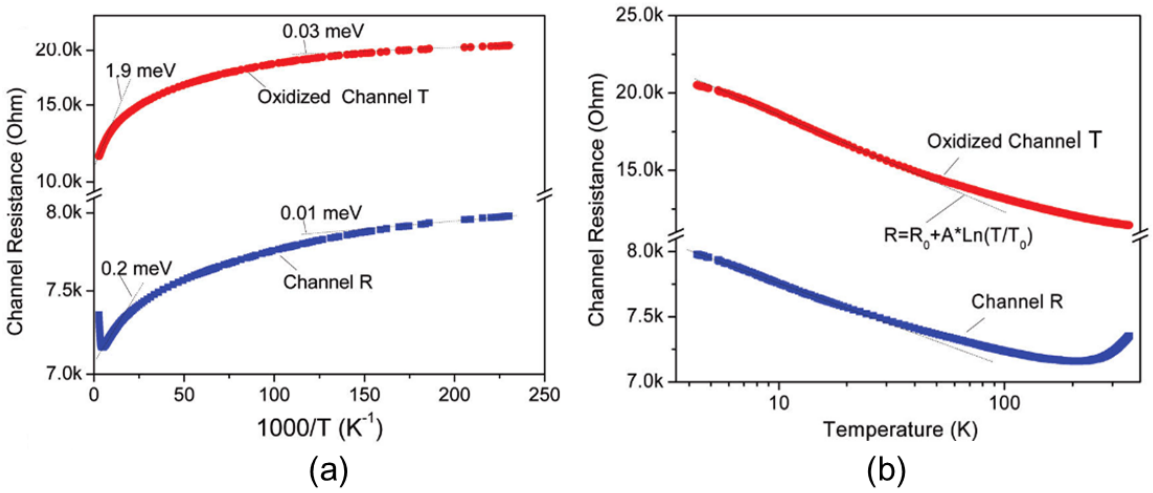

Figure 5.7: Temperature dependences of resistances of pristine and electro-oxidized graphene channels presented as (a) Arrhenius and (b) semi-logarithmic plot.

5.3.3 Effect of electro-oxidation on FET performance of EG

In order to further characterize both pristine and oxidized graphene channels, FET were fabricated on the basis of chemically treated EG substrate as shown in Figure 5.3. The FET transfer characteristics of both channels as a

function of gate voltage V_g in the temperature range from 300 to 4.4 K are shown in Figure 5.8 (a) and (b).

The pristine reference channel (Figure 5.8 (a)) shows p-type behavior, the origin of which may related to the EG growth conditions, defects and impurities in the underlying SiC wafer, and environmental doping.[71] The oxidized channel T shows a significantly increased degree of p-doping due to the electro-oxidation with the neutrality point shifted to positive polarity beyond the maximum gate voltage that could be applied (110 V). Since the graphene has no band gap, the conductivity could not be efficiently controlled by the gate voltage. Both pristine and oxidized channels show very limited FET performance. The most drastic difference between devices was observed in the on-off ratio of the FET devices: 1.9 (90% increase of the current) for the oxidized channel and 1.03 (3% increase of the current) for the pristine channel at *T* ~4.4 K, showing the enhancement of the FET performance of the EG channel after electro-oxidation with nitric acid.

From the slope of source-drain current versus gate voltage $\frac{dI_{sd}}{dV_g}$ in the negative *V*g range, carrier drift mobility can be calculated by using:

$$\mu = \frac{L \cdot t_{par}}{\varepsilon_{par} \cdot \varepsilon_0 \cdot V_{sd} \cdot W} \cdot \frac{dI_{sd}}{dV_g} \qquad (5.1)$$

where L and W are the length and width of the EG FET channel, respectively; t_{par} is the thickness of gate dielectric (parylene); ε_{par} is dielectric constant of parylene; ε_0 is the vacuum dielectric constant; and V_{sd} is the source-drain voltage. The mobility data for both FET channels as a function of temperature are presented in

Figure 5.8 (c). It may be seen that the drift mobilities in both channels are very low. The maximum values of the mobility for the pristine channels is 70 $cm^2/V \cdot s$, which is at the low end of the published data for EG[71, 72] and much lower than the best results.[2, 44, 72] Interestingly, the mobility in the oxidized channel is significantly higher than in the pristine channel. For the oxidized channel, the mobility increases as the temperature is lowered and reaches a maximum value of 370 $cm^2 \cdot V^{-1} \cdot s^{-1}$, followed by a drop below 25 K, which is typical of a transition from phonon to impurity scattering. The observed low values of mobility are probably due to the macroscopic size of our devices, which are not directly comparable to the lithographically defined, microscopic FETs that are typically confined to the highest quality areas of EG.

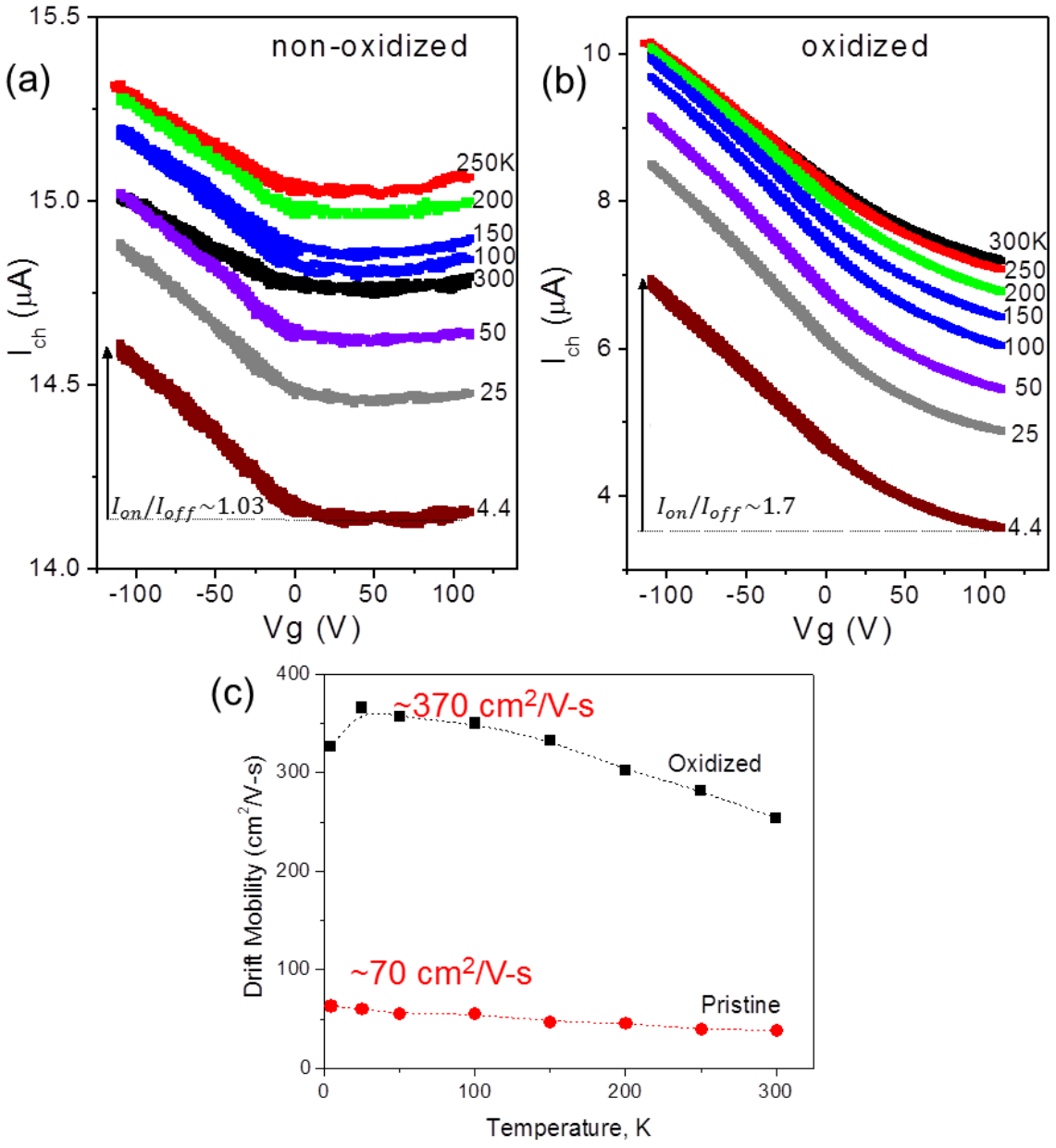

Figure 5.8: (a) Dependence of the channel current on gate voltage for pristine EG channel as a function of temperature. (b) Dependence of the channel current on gate voltage for electro-oxidized EG channel as a function of temperature. (c) FET mobility as a function of temperature for pristine and electro-oxidized EG channels.

5.3.4 Model of effect of electro-oxidation of EG

In order to explain the observed effects, we developed a model presented schematically in Figure 5.9. We assume that the uppermost layers are the most defective as a result of the bottom up growth of EG, [73-75] while the internal layers are of highest quality with lower concentration of defects and higher mobility. The observed increase of resistance together with the AFM image of EG channel during electro-oxidation is consistent with a picture in which the top 3-4 layers of the initial 6-8 layers are excluded from the electrical transport by a combination of point and line defects, delamination, and oxidative removal, while the underlying layers that are responsible for the charge transport remain relatively defect free. The gate voltage couples most strongly to the layers adjacent to the gate dielectric and is screened from the deeper layers, so the decrease in the total number of active layers will improve the utilization of the lower layers in the FLG stack. Thus, by excluding these defective outside layers from the electrical transport, the electro-oxidation process activates high-quality lower EG layers, thereby improving not only the on-off ratio, but also the effective drift mobility and enhancing all aspects of the FET performance.

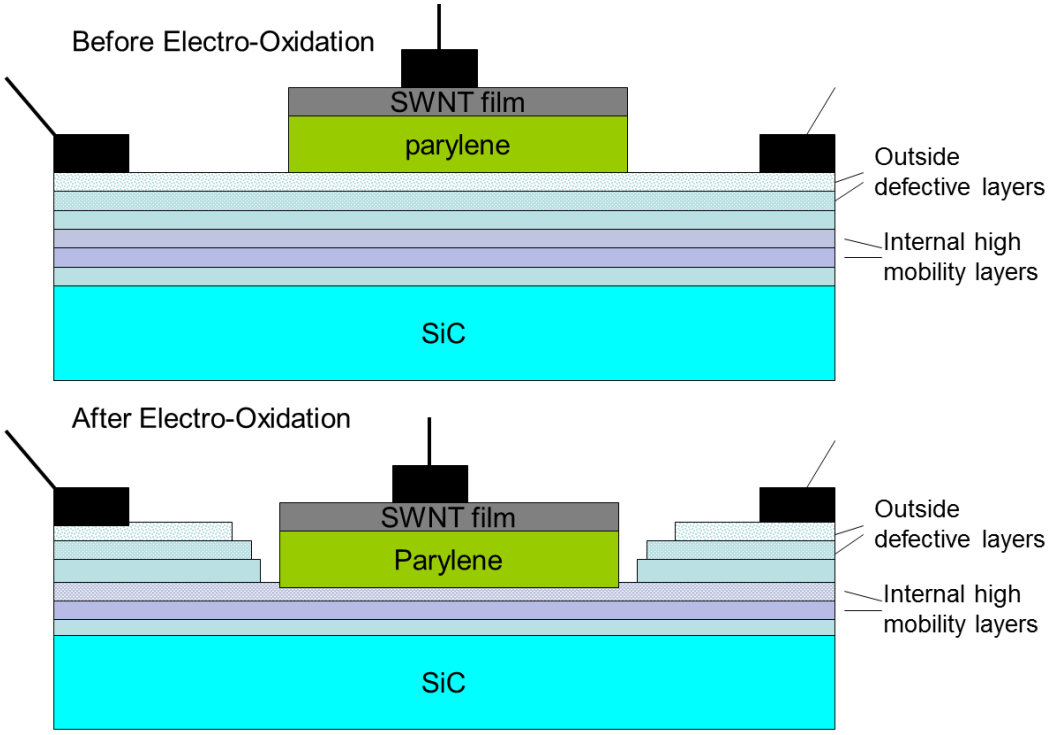

Figure 5.9: Schematic of effect of electro-oxidation on electronics properties of EG

5.3.5 Enhanced photosensitivity in electro-oxidized EG

The electro-oxidation dose did not lead to the energy gap opening, however, we observed enhanced photosensitivity.

We noticed, that under the fluorescent room light the resistance of the electro-oxidized channel decreases by ~6% while no changes was observed in the resistance of the reference (pristine) channel (Figure 5.10 (a)). Thus the direct comparison of the test and reference channels shows that the photoconductivity of the EG is significantly enhanced after electrochemical oxidation. The spectral dependence of the observed photoconductivity is

presented in Figure 5.10 (b); it shows an onset of the photoconductivity corresponding to a photon energy ~1.7 eV, and the photoresponse increases by four orders of magnitude in the UV spectral range.

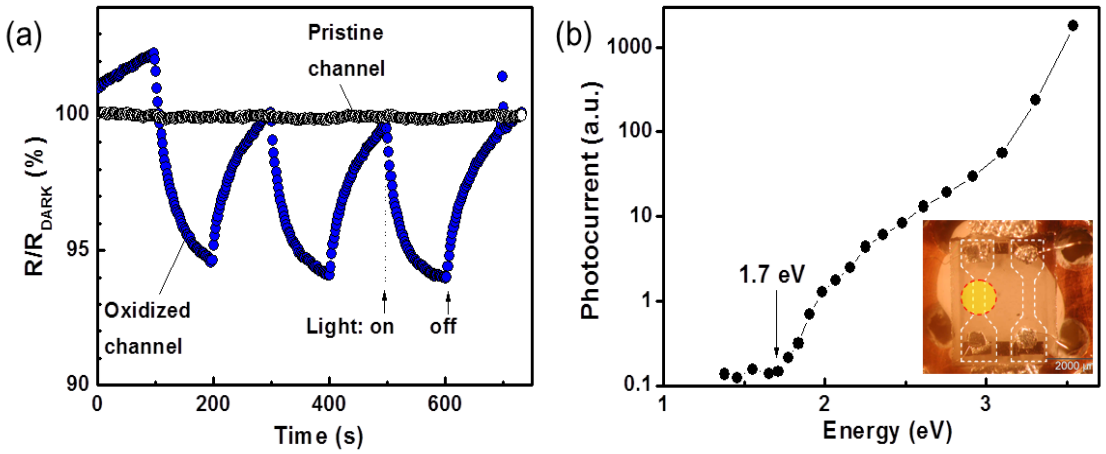

Figure 5.10: (a) Effect of fluorescent room light illumination on the resistance of electro-oxidized (blue circles) and pristine (black open circles) EG channels. (b) Spectral dependence of photoresponse of electro-oxidized channel. Inset shows schematics of the electro-oxidation EG substrate.

Figure 5.11 (a) shows the photoresponse of the electro-oxidized EG (EO-EG) channel to square-wave pulses of blue LED light (central wavelength ~470nm): the relative change of resistance under the incident power of 0.2 μW is at the level of 1% with a signal to noise ratio of ~100. At incident power 0.2 μW and the channel bias 450 mV, we obtained a current responsivity ~ 2.5 A/W and voltage responsivity ~ 20,000 V/W (measured against a calibrated Si photodiode), which is 3-4 orders of magnitude higher than previously reported

values in graphene,[47, 48, 51] and the current responsivity increases by more than 2 orders of magnitude in the UV range where it exceeds 200 A/W(Figure 5.11(b)). With increasing incident power P, we observed a sublinear increase of photocurrent I_{Ph} which can be expressed in the form: $I_{Ph} \propto P^{\gamma}$ where γ~0.4 (inset in Figure 5.11(b)), for power levels above 1 μW. The characteristic response time of the observed photoconductivity is in the tens of seconds; it persists for extended periods of time after the irradiation is turned off; thus it can be classified as transient photoconductivity.[76]

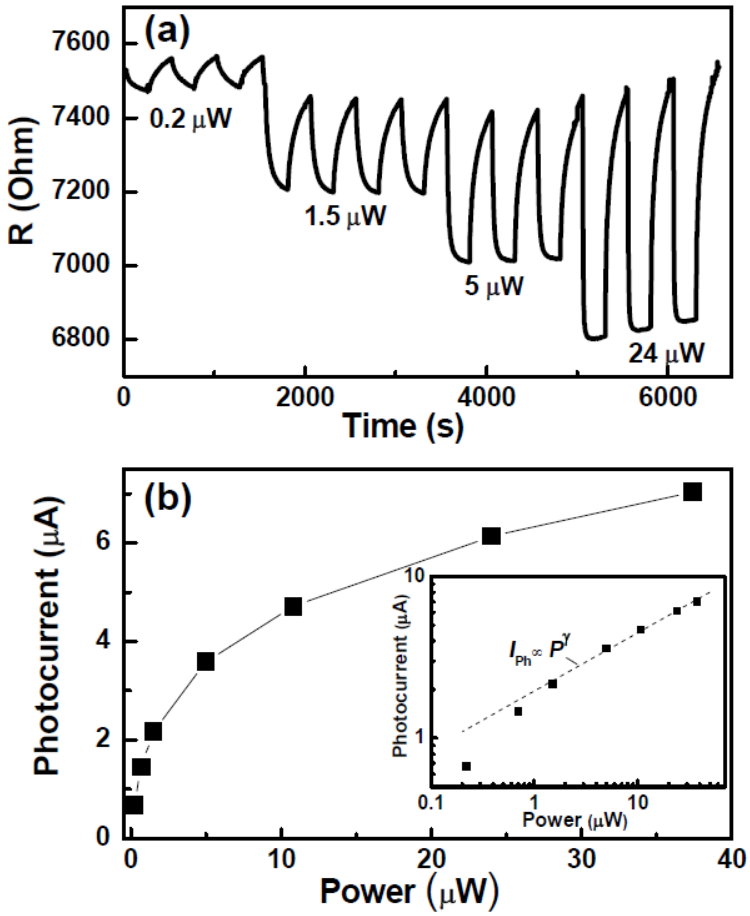

Figure 5.11: (a) Modulation of the resistance of the electro-oxidized EG channel under square-wave pulses of blue LED illumination of different power. (b) Dependence of electro-oxidized EG channels photocurrent on the power of incident radiation. Inset shows the dependence in logarithmic scales.

The onset of the photoconductivity and the enhanced photoresponse are usually associated with semiconducting materials with a well-defined energy gap, but in case of electro-oxidized EG the energy gap is not present. Instead, we attributed the behavior to the formation of localized defect states at the EG interface to the electro-oxidized material from which photogenerated carriers are released and enter the EG channel thus giving rise to the observed

photoconductivity. The interface defect states act not only as a source of additional photocarriers, they also change the recombination dynamics by preferentially capturing one carrier type before the electron-hole pairs recombine, localizing this carrier type in the traps and later re-injecting them into the channel, thereby prolonging the carrier life time from the (intrinsic) picosecond time scale to some tens of seconds (Figure 5.10(a) and 5.11(a)) thus significantly enhancing the photoconductivity. This mechanism has similarity with the classical description of the effect of traps in conventional semiconductors.[76, 77]

The power law, $I_{Ph} \propto P^{\gamma}$ satisfactorily fits the sublinear dependence of the photocurrent on the light intensity. This feature arises when the traps levels are distributed over a wide energy range: with increasing radiation intensity, quasi-Fermi level shifts convert a number of traps into recombination centers.[76, 77] This leads to a decrease in the life time of the photoexcitations resulting in a sublinear dependence of photocurrent on light intensity and faster photoresponse at higher power level as can be seen in Figure 5.11 (b) (P=24 μW). Similar transient photoconductivity phenomena have been observed in varieties of semiconductor systems, such as amorphous and microcrystalline silicon,[78, 79] In-Ga-Zn-O,[80] and ZnO thin films and nanowires.[81]

The enhanced photoconductivity was initially studied before the fabrication of FET. After the fabrication of FET, we did not observe any decrease in the photoresponse with parylene coating, suggesting that the photoresponse does

not originate from the oxygen photodesorption process previously observed in the case of exfoliated graphene FETs.[82]

Figure 5.12 (a) compares the transfer characteristics of the electro-oxidized EG FET in the dark and under blue LED illumination with 20 μW of incident power. In the absence of illumination the EG channel shows strong p-type behavior as described in chapter 5, while under illumination the "on" state current increases and the "off" state current decreases resulting in an increase in the on-off ratio and a better defined neutrality point which lies in the vicinity of +100 V. In the dark, the carrier drift mobility is μ = 390 cm^2/V-s. Under illumination the slope of the transfer characteristic increases, corresponding to a factor of 3 increase in the drift mobility of the holes to μ = 1100 cm^2/V-s, in the gate voltage V_g range from 0 to 50 V.

Reciprocal effect can be observed as shown in Fig.5.12 (b)-(d): the amplitude of the photoresponse of the electro-oxidized EG FET channel depends on the FET gate voltage. The photoresponse is enhanced by a factor of ~2 under negative gate voltage at V_g=-100 V in comparison with V_g=0 (Figure 5.12 (b),(c)), while the photoresponse is decreased by a factor of ~2 under a positive gate voltage at V_g=100 V (Figure 5.12(d)). Thus changing the gate polarity leads to a total modulation of the photoresponse by a factor of 4. This behavior is consistent with the model presented above: the gate potential shifts the position of the Fermi level with respect to the energy levels of the traps which converts a

number of the traps into recombination centers thus changing the lifetime of photo-carriers: positive gate voltages shorten the photocarriers life time leading to a decreased amplitude of the photoresponse; negative gate voltages prolong the photocarriers life time leading to an increased photoresponse.

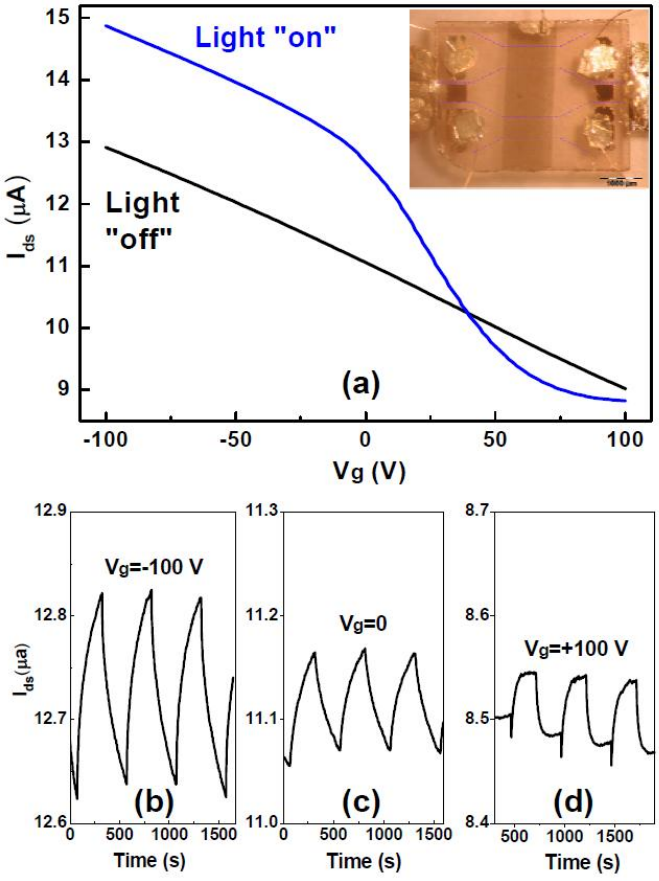

Figure 5.12: (a) Modification of transfer characteristics of electro-oxidized EG channel FET under blue LED illumination at incident power of 20 μW. (Inset) Microscope image of SiC substrate with two FETs based on pristine and electro-oxidized EG channels with SWNT thin film gate electrode. Dog bone shape of the channels is indicated by dashed line. (b-d) Photoresponse of electro-oxidized EG channel at gate voltages (b) -100V, (c) 0 V and (d) +100V at incident irradiation power 0.2 μW.

5.4 Summary

Controlled chemical treatment has been utilized to modify the electronic and optical properties of graphene. [41-43] In this chapter, I discuss a controlled electro-oxidation experiment conducted on multilayer EG channels, and show the presence of an additional reaction channel through the ridges in EG that is not present in flat carbons such as graphite and exfoliated graphene. The electro-oxidized channel shows a logarithmic increase of resistance with decreasing temperature, which can be ascribed to the scattering of the charge carriers in a two-dimensional electron gas, rather than to the presence of an energy gap at the Fermi level. The observed improved field-effect transistor performance in the electro-oxidized channel is ascribed to the gating of high-quality internal EG layers after electro-oxidative removal of the more defective outside layers.

Photoconductivity in EG may provide important information about energy band structure and this topic has not received much attention. We show that the utilization of electrochemical oxidation increases the photoresponsivity of EG to the level 2.5 A/W under blue light (wavelength 460 nm) and > 200 A/W in the UV range, which exceeds the previously reported responsivity values [49-55] by several orders of magnitude, but the response time is very slow. If further optimization of the chemistry can be made to shorten the photoresponse time while conserving the high sensitivity, the functionalized EG may be applied for UV detection for aerospace, automotive, and UV lithography together with biological and environmental research which requires blindness in the visible spectral range.

References:

1. Novoselov, K. S. et al. Electric Field Effect in Atomically Thin Carbon Films. Science 306, 666-669 (2004).
2. Berger, C. et al. Ultrathin Epitaxial Graphite: 2D Electron Gas Properties and a Route Toward Graphene-Based Nanoelectronics. J. Phys. Chem. B 108, 19912-19916 (2004).
3. Zhang, Y., Tan, Y. W., Stormer, H. L. & Kim, P. Experimental Observation of the Quantum Hall effect and Berry's Phase in Graphene. Nature 438, 201-204 (2005).
4. Novoselov, K. S. et al. Two-Dimensional Atomic Crystals. Proc. Nat. Acad. Sci. USA 102, 10451-10453 (2005).
5. Pletikosic, I. et al. Dirac Cones and Minigaps for Graphene on Ir(111). Phys. Rev. Lett. 102, 056808 - 4 (2009).
6. Li, X. S. et al. Large-Area Synthesis of High-Quality and Uniform Graphene Films on Copper Foils. Science 324, 1312-1314 (2009).
7. Bae, S. et al. Roll-to-Roll Production of 30-inch Graphene Films for Transparent Electrodes. Nat. Nanotech. 5, 574-578 (2010).
8. Kim, K. S. et al. Large-Scale Pattern Growth of Graphene Films for Stretchable Transparent Electrodes. Nature 457, 706-710 (2009).
9. Hernandez, Y. et al. High-Yield Production of Graphene by Liquid-Phase Exfoliation of Graphite. Nat. Nanotech. 3, 563-568 (2008).
10. Sokolov, D. A., Shepperd, K. R. & Orlando, T. M. Formation of Graphene Features from Direct Laser-Induced Reduction of Graphite Oxide. J. Phys. Chem. Lett. 1, 2633–2636 (2010).
11. Dubin, S. et al. A One-Step, Solvothermal Reduction Method for Producing Reduced Graphene Oxide Dispersions in Organic Solvents. ACS Nano 4, 3845-3852 (2010).
12. Li, X. L. et al. Simultaneous Nitrogen Doping and Reduction of Graphene Oxide. J. Am. Chem. Soc. 131, 15939-15944 (2009).
13. Compton, O. C. & Nguyen, S. T. Graphene Oxide, Highly Reduced Graphene Oxide, and Graphene: Versatile Buildings Blocks for Carbon-Based Materials. Small 6, 711-723 (2010).
14. Ghosh, S., Sarker, B. K., Chunder, A., Zhai, L. & Khondaker, S. I. Position Dependent Photodetector from Large Area Reduced Graphene Oxide Thin Films. Appl. Phys. Lett. 96, 163109 (2010).
15. Erickson, K. et al. Determination of the Local Chemical Structure of Graphene Oxide and Reduced Graphene Oxide. Adv. Mater. 22, 4467-4472 (2010).
16. Shin, H. J. et al. Efficient Reduction of Graphite Oxide by Sodium Borohydrilde and Its Effect on Electrical Conductance. Adv. Funct. Mater. 19, 1987-1992 (2009).

17. Ohta, T. et al. Interlayer Interaction and Electronic Screening in Multilayer Graphene Investigated with Angle-Resolved Photoemission Spectroscopy. Phys. Rev. Lett. 98, 206802 (2007).
18. Morozov, S. V. et al. Strong Suppression of Weak Localization in Graphene. Phys. Rev. Lett. 97, 016801 (2006).
19. Katsnelson, M. I., Novoselov, K. S. & Geim, A. K. Chiral Tunnelling and the Klein Paradox in Graphene. Nature Phys. 2, 620-625 (2006).
20. Ohta, T., Bostwick, A., Seyller, T., Horn, K. & Rotenberg, E. Controlling the Electronic Structure of Bilayer Graphene. Science 313, 951-954 (2006).
21. Brar, V. W. et al. Scanning Tunneling Spectroscopy of Inhomogeneous Electronic Structure in Monolayer and Bilayer Graphene on SiC. Appl. Phys. Lett. 91, 122102 (2007).
22. Oostinga, J. B., Heersche, H. B., Liu, X., Morpurgo, A. F. & Vandersypen, L. M. K. Gate Induced Insulting State in Bilayer Graphene Devices. Nat. Mater. 7, 151 (2007).
23. Boukhvalov, D. W. & Katsnelson, M. I. Tuning the Gap in Bilayer Graphene using Chemical Functionalization: Density Functional Calculations. Phys. Rev. B 78, 085413 (2008).
24. Zhang, Y. et al. Direct Observation of a Widely Tunable Bandgap in Bilayer Graphene. Nature 459, 820-823 (2009).
25. Bao, W. et al. Evidence for a Spontaneous Gapped State in Ultraclean Bilayer Graphene. PNAS 109, 10802-10805 (2012).
26. Li, X. L., Wang, X. R., Zhang, L., Lee, S. W. & Dai, H. J. Chemically Derived, Ultrasmooth Graphene Nanoribbon Semiconductors. Science 319, 1229-1232 (2008).
27. Obradovic, B. et al. Analysis of Graphene Nanoribbons as a Channel Material for Field-effect Transistors. Appl. Phys. Lett. 88, - (2006).
28. Chen, Z. H., Lin, Y. M., Rooks, M. J. & Avouris, P. Graphene Nano-Ribbon Electronics. Physica E 40, 228-232 (2007).
29. Han, M. Y., Ozyilmaz, B., Zhang, Y. B. & Kim, P. Energy Band-Gap Engineering of Graphene Nanoribbons. Phys. Rev. Lett. 98, 206805-4 (2007).
30. Jiang, D. E., Sumpter, B. G. & Dai, S. Unique Chemical Reactivity of a Graphene Nanoribbon's Zigzag Edge. J. Chem. Phys. 126, 134701 (2007).
31. Son, Y.-W., Cohen, M. L. & Louie, S. G. Half-Metallic Graphene Nanoribbons. Nature (London) 444, 347-349 (2008).
32. Nguyen, V. H., Do, V. N., Bournel, A., Nguyen, V. L. & Dollfus, P. Controllable Spindependent Transport in armchair Graphene Nanoribbon Structures. Preprint arXiv: 0905. 1868v 1 (2009).
33. Dresselhaus, M. S., Saito, R., Hofmann, M., Dresselhaus, G. & Jorio, A. Raman Spectroscopy of Graphene and Carbon Nanotubes. Adv. Phys. 60, 413-550 (2011).

34. Zhou, S. Y. et al. Substrate-Induced Bandgap Opening in Epitaxial Graphene. Nat. Mater. 6, 770-775 (2007).
35. Sofo, J. O., Chaudhari, A. S. & Barber, G. D. Graphane: A Two-Dimensional Hydrocarbon. Phys Rev. B 75, 153401 (2007).
36. Boukhvalov, D. W., Katsnelson, M. I. & Lichtenstein, A. I. Hydrogen on Graphene: Electronic Structures, Total Energy, Structural Distortions and Magnetism from First-Principles Calculations. Phys Rev. B 77, 035427 (2008).
37. Kamat, P. V. Graphene - A Physical Chemistry Perspective. J. Phys. Chem. Lett. 1, 587-588 (2010).
38. Kamat, P. V. Graphene-Based Nanoarchitectures. Anchoring Semiconductor and Metal Nanoparticles on a Two-Dimensional Carbon Support. J. Phys. Chem. Lett. 1, 520-527 (2010).
39. Elias, D. C. et al. Control of Graphene's Properties by Reversible Hydrogenation: Evidence for Graphane. Science 323, 610-613 (2009).
40. Bekyarova, E., Itkis, M. E., Ramesh, P. & Haddon, R. C. Chemical Approach to the Realization of Electronic Devices in Epitaxial Graphene. Phys. Stat. Sol. RRL 3, 184-186 (2009).
41. Bekyarova, E. et al. Chemical Modification of Epitaxial Graphene: Spontaneous Grafting of Aryl Groups. J. Am. Chem. Soc. 131, 1336-1337 (2009).
42. Niyogi, S. et al. Spectroscopy of Covalently Functionalized Graphene. Nano. Lett. 10, 4061–4066 (2010).
43. Hong, J. et al. Effect of Nitrophenyl Functionalization on the Magnetic Properties of Epitaxial Graphene. Small 7, 1175-1180 (2011).
44. Berger, C. et al. Electronic Confinement and Coherence in Patterned Epitaxial Graphene. Science 312, 1191-1196 (2006).
45. de Heer, W. A. et al. Epitaxial Graphene. Solid State Commun. 143, 92-100 (2007).
46. Nair, R. R. et al. Fine Structure Constant Defines Visual Transparency of Graphene. Science 320, 1308 (2008).
47. Xia, F., Mueller, T., Lin, Y., Valdes-Garcia, A. & Avouris, P. Ultrafast Graphene Photodetector. Nature Nanotech. 4, 839-843 (2009).
48. Mueller, T., Xia, F. & Avouris, P. Graphene Photodetectors for High-Speed Optical Communications. Nature Photon. 4, 297-301 (2010).
49. Lee, E. J. H., Balasubramanian, K., Weitz, R. T., Burghard, M. & Kern, K. Contact and Edge Effects in Graphene Devices. Nature Nanotech. 3, 486-490 (2008).
50. Xia, F. et al. Photocurrent Imaging and Efficient Photon Detection in a Graphene Transistor. Nano Lett. 9, 1039-1044 (2009).
51. Park, J., Ahn, Y. H. & Ruiz-Vargas, C. Imaging of Photocurrent Generation and Collection in Single-Layer Graphene. Nano Lett. 9, 1742-1746 (2009).

52. Mueller, T., Xia, F., Freitag, M., Tsang, J. & Avouris, P. Role of Contacts in Graphene Transistors: A Scanning Photocurrent Study. Phys. Rev. B 79, 245430 (2009).
53. Lv, X. et al. Photoconductivity of Bulk-Film-Based Graphene Sheets. Small 5, 1682-1687 (2009).
54. Lin, Y. et al. Dramatically Enhanced Photoresponse of Reduced Graphene Oxide with Linker-Free Anchored CdSe Nanoparticles. ACS Nano 4, 3033-3038 (2010).
55. Geng, X. et al. Aqueous-Processable Noncovalent Chemically Converted Graphene-Quantum Dot Composites for Flexible and Transparent Optoelectronic Films. Adv. Mater. 22, 638-642 (2010).
56. Podzorov, V., Pudalov, V. M. & Gershenson, M. E. Field-Effect Transistors on Rubrene Single Crystals with Parylene Gate Insulator. Appl. Phys. Lett. 82, 1739-1741 (2003).
57. Butko, V. Y., Chi, X., Lang, D. V. & Ramirez, A. P. Field-Effect Transistor on Pentacene Single Crystal. Appl. Phys. Lett. 83, 4773-4775 (2003).
58. Sun, G. F., Jia, J. F., Xue, Q. K. & Li, L. Atomic-Scale Imaging and Manipulation of Ridges on Epitaxial Graphene on 6H-SiC(0001). Nanotechnology 20, 355701-1-355701-4 (2009).
59. de Heer, W. A. et al. Epitaxial Graphene Electronic Structure and Transport. J. Phys. D: Appl. Phys. 43, 374007 (2010).
60. Haddon, R. C. Chemistry of the Fullerenes: The Manifestation of Strain in a Class of Continuous Aromatic Molecules. Science 261, 1545-1550 (1993).
61. Niyogi, S. et al. Chemistry of Single-Walled Carbon Nanotubes. Acc. Chem. Res. 35, 1105-1113 (2002).
62. Dolan, C. J. & Osheroff, D. D. Nonmetallic Conduction in Thin Metal Films at Low Temperatures. Phys. Rev. Lett. 43, 721-724 (1979).
63. Bishop, D. J., Tsui, D. C. & Dynes, R. C. Nonmetallic Conduction in Electron Inversion Layers at Low Temperatures. Phys. Rev. Lett. 44, 1153-1156 (1980).
64. Markiewicz, R. S. & Harris, L. A. Two- Dimensional Resistivity of Ultrathin Metal Films. Phys. Rev. Lett. 46, 1149-1153 (1981).
65. Ovadyahu, Z. & Imry, Y. Magnetoresistance Effects in an Effectively Two-Dimensional Systems. Weak Anderson Localization. Phys. Rev. B 24, 7439-7442 (1981).
66. Thouless, D. J. Maximum Metallic Resistance in Thin Wires. Phys. Rev. Lett. 39, 1167-1170 (1977).
67. Anderson, P. W., Abrahams, E. & Ramakrishnan, T. V. Possible Explanation of Nonlinear Conductivity in Thin-Film Metal Wires. Phys. Rev. Lett. 43, 718-720 (1979).
68. Abrahams, E., Anderson, P. W., Licciardello, D. C. & Ramakrishnan, T. V. Scaling Theory of Localization: Absence of Quantum Diffusion in Two Dimensions. Phys. Rev. Lett. 42, 673-676 (1979).

69. Altshuler, B. L., Aronov, A. G. & Lee, P. A. Interaction Effects in Disordered Fermi Systems in Two Dimensions. Phys. Rev. Lett. 44, 1288-1291 (1980).
70. Fukuyama, H. Effects of Interactions on Non-Metallic Behaviors in Two-Dimensional Disordered Systems. J. Phys. Soc. Jpn. 48, 2169-2170 (1980).
71. Tedesco, J. L. et al. Hall Effect Mobility of Epitaxial Graphene Grown on Silicon Carbide. Applied Physics Letters 95, 122102 (2009).
72. Robinson, J. A. et al. Correlating Raman Spectral Signatures with Carrier Mobility in Epitaxial Graphene: A Guide to Achieving High Mobility on the Wafer Scale. Nano Lett. 9, 2873-2876 (2009).
73. Poon, S. W., Chen, W., Tok, E. S. & Wee, A. T. S. Probing Epitaxial Growth of Graphene on Silicon Carbide by Metal Decoration. Applied Physics Letters 92, 104102 (2008).
74. Emtsev, K. V. et al. Towards Wafer-Size Graphene Layers by Atmospheric Pressure Graphitization of Silicon Carbide. Nature Materials 8, 203-207 (2009).
75. Robinson, J. et al. Nucleation of Epitaxial Graphene on SiC(0001). ACS Nano 4, 153-158 (2010).
76. Joshi, N. V. Photoconductivity: Art, Science, and Technology (ed. Thompson, B. J.) (Marcel Dekker, Inc. , NY, NY, 1990).
77. Bube, R. H. Photoconductivity of Solids (John Wiley & Sons, Inc., NY, London, 1960).
78. Beyer, W. & Hoheisel, B. Photoconductivity and Dark Conductivity of Hydrogenated Amorphous Silicon. Solid State Commun. 47, 573-576 (1983).
79. Bruggermann, R. Photoconductivity Studies of n-Type Hydrogenated Amorphous Silicon and Microcrystalline Silicon. J. Mater. Sciense: Mater. in Electronics 14, 629-633 (2003).
80. Lee, D. H., Kawamura, K., Nomura, K., Kamiya, T. & Hosono, H. Large Photoresponse in Amorphous In-Ga-Zn-O and Origin of Reversible and Slow Decay. Electrochem. Solid-State Lett. 13, H324-H327 (2010).
81. Zheng, H. G. et al. Photoconductive Ultraviolet Detectors Based on ZnO Films. Appl. Surf. Sci. 253, 2264-2267 (2006).
82. Shi, Y., Fang, W., Zhang, K., Zhang, W. & Li, L.-J. Photoelectrical Response in Single-Layer Graphene Transistors. Small 5, 2005-2011 (2009).